Research in aeroelasticity EFP-2005

Bak, C.

Publication date:
2006

Document Version
Publisher's PDF, also known as Version of record

RISØ

Risø-R-1559(EN)

Research in Aeroelasticity EFP-2005

Edited by Christian Bak

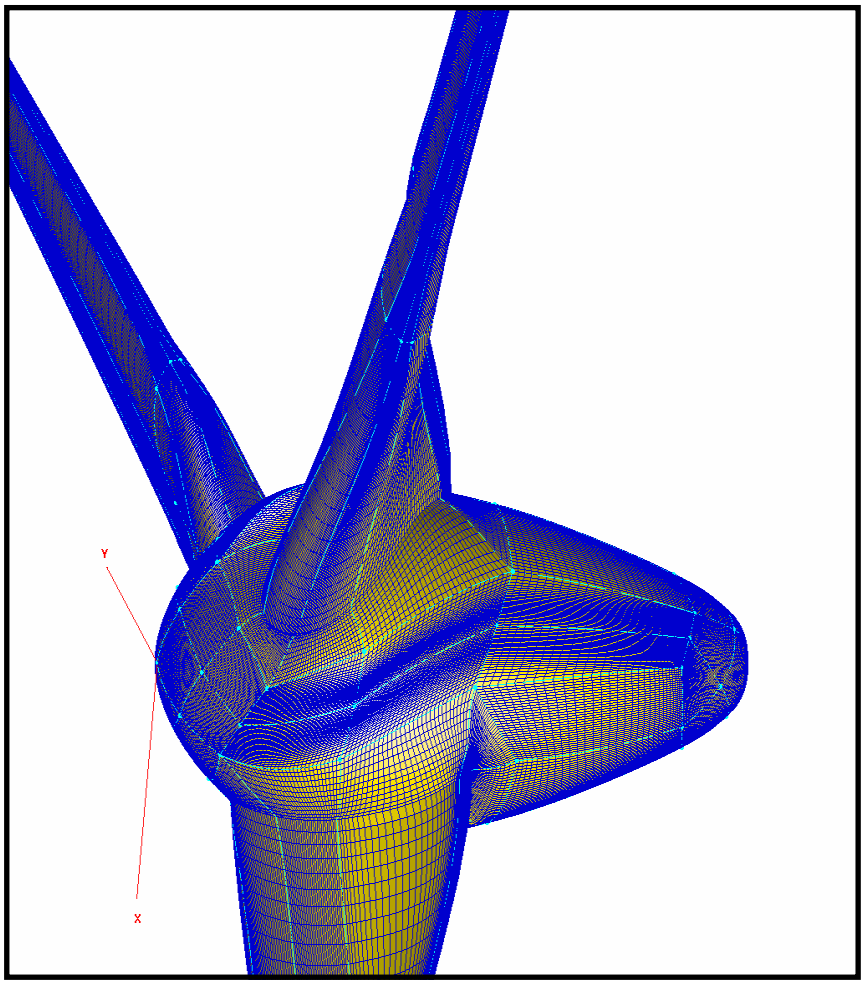

Risø National Laboratory
Roskilde
Denmark
May 2006

Risø-R Report

Author: Edited by Christian Bak
Title: Research in Aeroelasticity EFP-2005
Department: Wind Energy Department

Risø-R-1559(EN)
May 2006

Abstract:

In the Energy Research Project "Program for Research in Applied Aeroelasticity" (EFP2005), Risø National Laboratory (Risø) and the Technical University of Denmark (DTU) have applied and further developed the tools in the aeroelastic design complex. The main results from the project are:

- Adding a winglet to a wind turbine blade for minimizing the induced drag of the blade led to the biggest increase in power of 1.4%.
- Transient wind loads during pitch motion are determined using CFD. Compared to the NREL/NASA Ames test, reasonably good agreement is seen.
- A general method was developed for the determination of 3D angle of attack for rotating blades from either measurements or numerical computations using CFD.
- A model of the far wake behind wind turbines was developed for stability studies of the tip vortices in the far wake.
- Investigating the blade root region showed that the power efficiency, CP, locally can be increased significantly beyond the Betz limit, but that the global CP for the rotor cannot exceed the Betz limit. When including tip losses and a minimum blade drag coefficient, a maximum rotor CP in the range of 0.51-0.52 was obtained.
- A new airfoil family was designed and a 3D airfoil design tool was developed. Compared to the Risø-B1 family, the new airfoil family showed similar or improved aerodynamic and structural characteristics.
- Four different airfoils were analyzed to reveal the differences between 2D and 3D CFD. The major conclusions are the dependency of computational results to transition modelling, and the ability of 3D DES calculations to realistically simulate the turbulent wake of an airfoil in stall.
- The capability of a theory for simulation of Gaussian turbulence driven gust events was demonstrated by emulating a violent shear gust event from a complex site. An asymptotic model for the PDF of the largest excursion from the mean level, during an arbitrary recurrence period, has been derived for a stochastic wind speed process driven by atmospheric turbulence.
- The simulation of an offshore monopile foundation with HAWC2 showed a reduction of the first tower frequency with app. 5%. The influence of hydrodynamics showed only minor influence on the tower frequency and damping. An increase in external water velocity leads to a noticeable increase in damping.
- A new anisotropic beam element has been implemented. This provides the basis for giving more confidence in flutter estimation and the ability to analyze the reduction of fatigue loads by aeroelastic tailoring of future blades.

ISSN 0106-2840
ISBN 87-550-3521-3

Contract no.:
ENS 33031-0077

Group's own reg. no.:
1110047-01

Sponsorship:
Energistyrelsen
Amaliegade 44
1256 København K

Cover :
The cover shows a mesh used in the 3D CFD analysis of the inboard rotor aerodynamics including an aerodynamically shaped spinner

Pages: 107
Figures: 87
Tables: 10
References: 87

Risø National Laboratory
Information Service Department
P.O.Box 49
DK-4000 Roskilde
Denmark
Telephone +45 46774004
bibl@risoe.dk
Fax +45 46774013
www.risoe.dk

Contents

1 Summary 7

1.1 Main results from the project 7
1.2 References 10

2 Advanced rotor aerodynamics – including tip and root aerodynamics 11

2.1 Winglets 11
2.2 Transient loads during pitch motion 13
2.3 Determination of angle of attack for rotating blades 14
2.4 Modelling of the far wake behind a wind turbine 16
2.5 References 17

3 Inboard rotor/blade aerodynamics and its influence on blade design 19

3.1 Background and motivation for the work 19
3.2 Two analytical solutions for the description of the influence from the pressure term caused by wake rotation 21
3.3 Overview of the numerical modeling used in the analysis 24
3.4 The influence of wake pressure from wake rotation 27
3.5 A simple method to include the influence of wake pressure from wake rotation in the BEM code 29
3.6 What is the maximum power coefficient for a rotor and what is the corresponding loading ? 30
3.7 Influence of spinner – AD simulations 35
3.8 Results from analysis of a specific rotor design 36
3.9 Summary 38
3.10 References 39

4 New Airfoil Family Considering Structural Stiffness and Compatibility 41

4.1 Nomenclature 41
4.2 Introduction 42
4.3 The airfoil design tool 42
4.4 Design strategy 44
4.5 The new airfoil family 46
4.6 Conclusions 53
4.7 References 53

5 Profile Catalogue for Airfoil Sections Based on 3D Computations 55

5.1 Description of the Navier-Stokes Solver 55
5.2 RISØ-B1-18 Airfoil 56
5.3 NACA 63-430 Airfoil 58
5.4 S809 Airfoil 60
5.5 DU 93-W-210 Airfoil 63
5.6 Analysis and Summary of the Results 65
5.7 Conclusion 67
5.8 References 68

6 Aeroelastic response in extreme wind cases 69

6.1 The importance of a stochastic formulation of extreme gusts 69
6.2 The statistical distribution of turbulence driven one point velocity extremes 78
6.3 Conclusions 85
6.4 References 86

7 Influence of soil and water on tower dynamics 89

7.1 Introduction 89
7.2 Symbols 90
7.3 Model 90
7.4 Investigation of soil support 92
7.5 Investigation of influence of water level on tower frequency and damping at standstill 94
7.6 Influence of water level of dynamic tower response during operation 95
7.7 Results and discussion 96
7.8 References 97

8 Torsional properties of large wind turbine blades 99

8.1 Description of Master Projects 99
8.2 Application of an anisotropic beam model 102
8.3 Conclusion 104
8.4 References 105

9 Conclusion 107

10 Complete list of publications from the project 111

10.1 Journal papers 111
10.2 Conference papers 111
10.3 Reports 112
10.4 Lectures 112

Preface

The Energy Research Project ”Program for Research in Applied Aeroelasticity, EFP-2005” was carried out in cooperation between Risø National Laboratory and the Technical University of Denmark (DTU) from 1 April 2005 to 31 March 2006. From the onset of the project, six milestones were defined which represents the main part of the research activity. Apart from the work focused on the milestones, also analyses of current problems and further development of the existing models were carried out.

Several researchers at the DTU and Risø have been involved in the project work and have contributed to the research presented in this report. To enable reference to the different parts of the report, the names of the authors is indicated for each chapter. It should, however, be emphasized that the report is not a detailed report of the complete activity within the project. Thus, not all of the contributors to the project appear as authors to the different chapters. For a detailed description of the results from the project, please see Chapter 0 in which a complete list of publications in the project can be found.

At the DTU, the following researchers from the Fluid Mechanics Section of the Department of Mechanical Engineering have been involved in the project:

Kurt S. Hansen
Martin O.L. Hansen
Robert Mikkelsen
Wen Zhong Shen
Jens Nørkær Sørensen
Stig Øye

At Risø, primarily the researchers from the Aeroelastic Design Group have contributed to the project:

Peter B. Andersen
Christian Bak
Franck Bertagnolio
Kim Branner
Thomas Buhl
Mac Gaunaa
Anders M. Hansen
Morten H. Hansen
Jeppe Johansen
Gunner C. Larsen
Torben J. Larsen
Helge A. Madsen
Helen Markau
Flemming Rasmussen
Niels N. Sørensen
Kenneth Thomsen

1 Summary

This report contains the results from the Energy Research Project ”Program for Research in Applied Aeroelasticity, EFP-2005” covering the period from 1. April 2005 to 31. March 2006. The project partners are Risø National Laboratory and The Technical University of Denmark (DTU). The overall objectives of the project are to ensure the development of an aeroelastic design complex, which can create the basis for the next generation of wind turbines and make new design concepts possible. The project forms a strategic cooperation between Risø and the DTU and the wind turbine industry with emphasis on obtaining a suitable balance between long-term strategic research, applied research and technological development. To obtain synergy between the different subjects and to ensure an optimal, dynamic cooperation with the industry, while maintaining the continuity of the research, the project is organized as a research program within applied aeroelasticity with a combination of research activities with specific short-term targets within one year and general continuous long-term research activities. This research project has been the eighth in a row of one-year projects, which has ensured a continuous development since 1997, where the activity in this row of projects is described in [1], [2], [3], [4], [5], [6] and [7].

Risø and DTU develop an aeroelastic design complex which creates the basis for the next generation of wind turbines

1.1 Main results from the project

The main emphasis of the activity in the project was put on the milestones which were defined in the project proposal. Furthermore, there has been activity on the further development of tools and models in “the aeroelastic design complex” which consists of 3D Navier-Stokes models, aeroacoustic models, airfoil- and blade design, aeroelastic codes and loads, aeroelastic stability, control and new concepts. Also, there have been investigations of subjects of fundamental character, which often constitute long-term research. A summary of the main results from the project is given in the following.

Advanced rotor aerodynamics – tip and root aerodynamics

Winglets can increase the power slightly

The aerodynamic codes used at both Risø and the DTU have reached a level of advancement, so that specific details of the flow around a wind turbine rotor can be analyzed in detail. Furthermore, the wind turbine industry has shown an increased interest in investigating specific design changes which could improve the overall rotor performance. Therefore, several specific issues have been investigated during the present project. These include:

Sudden pitch changes simulated with CFD show reasonably good agreement with experiments

- the aerodynamic investigation of adding a winglet to the wind turbine blade for minimizing the induced drag of the blade, where different winglet configurations were analysed, and for a winglet pointed toward the wind the biggest increase in power was 1.4% with a corresponding increase in thrust of 1.6%. Effects of sweep and cant angles were not accounted for in this analysis.
- modelling of transient wind loads during pitch motion, where the time constants varying along the blade span are determined using the EllipSys3D Navier-Stokes solver and an actuator disc method. Transients in the computations are compared to the NREL/NASA Ames test and reasonably good agreement is seen.

A general method for determination of angles of attack for rotors is developed

- determination of 3D angle of attack for rotating blades, which is a general method for determining angle of attack from either measurements or numerical computations using CFD.

A model for the far wake is developed for stability studies

- modelling of the far wake behind wind turbines, which forms the basis for a supplementary work on stability of the tip vortices in the far wake behind a wind turbine.

The blade root region is investigated aerodynamically, showing that the efficiency can be increased locally but not globally

- the investigation of an aerodynamically more efficient root region, where it was found that the power efficiency, CP, locally can be increased significantly beyond the Betz limit, but that the global CP for the rotor cannot exceed the Betz limit. Furthermore, a simple correction of the Glauert BEM model to account for the effect from the pressure term from wake rotation has been developed and tested. Finally, when including tip losses and the minimum blade drag coefficient, a maximum rotor CP in the range of 0.51-0.52 was obtained, which is in good agreement with 3D CFD computations which showed a CP around 0.51.

Airfoil design

A new airfoil family with high maximum lift considering structural stiffness and compatibility using a 3D design tool is designed

A new airfoil family for MW-size wind turbines with variable speed and pitch control was designed. Five airfoils were designed with thickness-to-chord ratios between 15% and 30% to cover most of the span of a wind turbine blade. The airfoils were designed to have high maximum lift coefficient to allow a slender flexible blade while maintaining high aerodynamic efficiency. Given those characteristics, the airfoils were designed with maximum stiffness and compatibility between the airfoils. Finally, the airfoils were designed to be roughness insensitive. Compared to an earlier airfoil design, i.e. the Risø-B1 family, the aerodynamic characteristics are improved because the characteristics with forced transition at the leading edge are similar, but with free transition the lift-drag ratio was increased significantly for lift values between 1.0 and 1.6. When comparing the structural characteristics with the Risø-B1 family, it has been found that the new airfoil family is around 5% more stiff around the chord line corresponding to the flap direction for a wind turbine blade, and the compatibility between the airfoils was further improved. The design was carried out using a Risø in-house multi disciplinary optimization tool which was extended to 3D so that the complete blade shape, including the compatibility between the airfoil sections, and the rotor flow were taken into account.

2D airfoil catalogue based on 3D DES computations

The influence of 3D effects on 2D airfoil characteristics are investigated using CFD

This investigation is a continuation of the Wind Turbine Airfoil Catalogue (EFP-2000/2001) the objective of which was, firstly, to provide a database of aerodynamic characteristics for a wide range of airfoil profiles aimed at wind turbine applications, and secondly to test the two-dimensional Navier-Stokes solver EllipSys2D by comparing its results with experimental data. In the present work, the original two-dimensional results are compared with three-dimensional calculations as it was surmised that the two-dimensional assumption in some cases could be responsible for discrepancies between the numerical flow solution and the actual fluid flow, and thereby the incorrect prediction of airfoil characteristics. In addition, other features of the flow solver, such as transition and turbulence modelling, and their influence onto the numerical results are investigated. Several mechanisms explaining the discrepancies between the different numerical simulations, and some of the experimental results, have been identified based on four different airfoils. However, these conclusions cannot in general be applied to all types of airfoils. The two major conclusions of this work are the dependency of computational results to transition modelling, and the ability of 3D DES calculations to realistically simulate the turbulent wake of an airfoil in stall.

Aeroelastic response from MW turbines in extreme wind situations

Extreme loads are investigated by using a gust generator and by developing statistical extreme value model

The purpose of the present work is to initiate a process in which today's state-of-the-art extreme load specifications eventually are replaced by physically more realistic stochastic extreme load cases. To achieve this goal, the following is required:

- A "gust generator" that facilitate generation of consistent simulated turbulence fields, consisting of fully 3D multiple correlated stochastic processes, containing one or more extreme events, with the second order structure functions correctly represented;
- A statistical model that, for a given set of turbulence characteristics and an arbitrarily selected return period, can predict realistic (most likely) gust amplitudes as input for the "gust generator" on a rational basis.

The requested "gust generator" is available from a previous energy research project. The present contribution thus deals partly with the illustration of the capacity of this "gust generator" and partly with the development of a statistical model for an especially simple gust event. Accordingly, the work falls in two parts. The first part uses the developed "gust generator" to demonstrate the importance of considering stochastic gust events as an alternative to today's stylized deterministic coherent gust specifications. This study furthermore stresses the importance of a site-specific determination of gust amplitudes. In line with that, the second part deals with the development of a consistent statistical extreme value model for the simplest possible gust type – a one point wind speed increase.

Integrated hydroelastic and aeroelastic computations on offshore turbine

The effect of an offshore monopole foundation on a wind turbine tower is investigated using HAWC2

The newly developed code HAWC2 was used to investigate some stability effects regarding the boundary conditions of a monopile foundation that is lacking in other codes. Nonlinear soil spring forces were applied as well as hydrodynamic forces based on Morison's equation. The boundary conditions of the soil and the flexibility of the pile mainly reduce the first tower frequency with app. 5%. A parameter variation showed that when the pile length exceeds a certain minimum length, any further elongation does not contribute to increased stiffness. It is verified that even though the soil support has a very nonlinear characteristic, it is fully justifiable to simplify the model by modelling the monopile down to an equivalent depth where it is fully fixed. The influence of hydrodynamics showed only minor influence on the tower frequency and damping. The hydrodynamics only affect the mode shapes where the 2nd tower bending mode is present by decreasing the natural frequency. The effective damping on the 1st tower vibration is not affected by the hydrodynamics, but slightly on the higher frequencies. An increase in external water velocity, which occurs due to current or waves, leads to a noticeable increase in damping.

Torsional properties for large wind turbine blades

Torsional properties are analyzed by implementing a new anisotropic beam element and carry out measure-ments on a blade section

The work performed under the milestone related to torsional properties for large wind turbine blades is on-going and will be continued in the continuation of the EFP-2005-project. During the project, a new anisotropic beam element based on the program VABS, which is a program for providing sectional-properties of arbitrary blade sections from geometry and material properties, has been implemented. The verification of the beam element formulation awaits the finalization of the 2 master projects which were initiated during this milestone. When these master projects are finalized, it is expected that the present work provides an improved model for doing blade response analysis,

which has been verified by comparison between experiments (static and dynamic) and a FEM shell model. This provides the basis for giving more confidence in flutter estimation and also the ability to analyze the reduction of fatigue loads by aeroelastic tailoring of future blades.

1.2 References

[1] Madsen, H.A. (Red.) ”Forskning i Aeroelasticitet. Rapport for EFP-97” (in Danish), Risø-R-1066(DA), Forskningscenter Risø, Roskilde, August 1998

[2] Madsen, H.A. (Red.) ”Forskning i Aeroelasticitet – EFP-98” (in Danish), Risø-R-1129(DA), Forskningscenter Risø, Roskilde, August 1999

[3] Madsen, H.A. (Red.) ”Forskning i Aeroelasticitet – EFP-99” (in Danish), Risø-R-1196(DA), Forskningscenter Risø, Roskilde, November 2000

[4] Madsen, H.A. (Red.) ”Forskning i Aeroelasticitet – EFP-2000” (in Danish), Risø-R-1272(DA), Forskningscenter Risø, Roskilde, Juli 2001

[5] Madsen, H.A. (Red.) ”Forskning i Aeroelasticitet EFP-2001” (in Danish), Risø-R-1349(DA), Forskningscenter Risø, Roskilde, December 2002

[6] Bak, C. (Red.) ”Forskning i Aeroelasticitet EFP-2002” (in Danish), Risø-R-1434(DA), Forskningscenter Risø, Roskilde, Februar 2004

[7] Bak, C. (Red.) ”Forskning i Aeroelasticitet EFP-2004” (in Danish), Risø-R-1509(DA), Forskningscenter Risø, Roskilde, Maj 2005

2 Advanced rotor aerodynamics – including tip and root aerodynamics

Jeppe Johansen, Niels N. Sørensen, Helge Aa. Madsen, Wen Zhong Shen and Valery Okulov

The aerodynamic codes used at both Risø and DTU have reached a level of advancement so that specific details of the flow around a wind turbine rotor can be analyzed in detail. Furthermore, the wind turbine industry has shown an increased interest in investigating specific design changes, in order to improve the overall rotor performance. Therefore, several specific issues have been investigated during the present project. These include the aerodynamic investigation of adding a winglet to the wind turbine blade for minimizing the induced drag of the blade, modelling of transient wind loads during pitch motion, determination of 3D angle of attack for rotating blades, modelling of the far wake behind wind turbines and finally, the investigation of an aerodynamically more efficient root region. The first four research areas will be described briefly in the following chapter, while the latter will be described in more depth in a separate chapter. All work has been published and is shown in the reference list at the end of the present chapter.

2.1 Winglets

In short, the purpose of adding a winglet to a rotor blade design is to decrease the induced drag on the blade by changing the downwash distribution. The art is then to design a winglet, which carries an aerodynamic load such that the vortex sheet shed from the winglet diminishes the influence of the tip vortex, decreasing the downwash and reduces the induced drag. Or in other words; to design a winglet such that the extra form drag of the winglet is smaller than the decrease in induced drag such that the total drag is decreased.

The effect of winglets has been investigated using CFD

To investigate the aerodynamic effect of adding a winglet to a wind turbine blade five different winglets were designed and added on an existing pitch regulated turbine and the aerodynamic forces were computed using the 3D CFD code EllipSys3D. The work has been published in refs. [1] and [2], and for more in depth information the reader is referred to these. To maximize the effect of the winglet the tip was assumed rectangular and the rotor radius was kept constant. Four winglets pointed upwind and one winglet pointed downwind, see Figure 2-1. The height of the winglet was set to 1.5% of the rotor radius. For comparison a rectangular type tip with the same solidity as the blades with winglets projected on the rotor plane was computed.

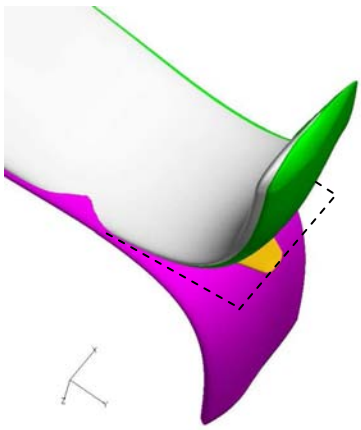

Figure 2-1: Example of the upwind pointing winglets (green and white) and downwind pointing winglet (purple) compared to the original blade (orange) and the rectangular tip (dashed line).

Results are presented as increase/decrease in mechanical power and thrust compared to the original blade in Figure 2-2. *winglet1* to *winglet4* refers to upwind pointing winglets. *winglet1* is made with a symmetric airfoil with a geometric angle of attack of 0º. *winglet2*, *winglet3* and *winglet4* have a cambered airfoil with a geometric angle of attack of 2º, 5º and -3º, respectively. Finally, *winglet5* is pointing downwind with a geometric angle of attack of 2º. The results of the rectangular tip are included for comparison.

The present winglets increase mechanical power of up to 1.7 %

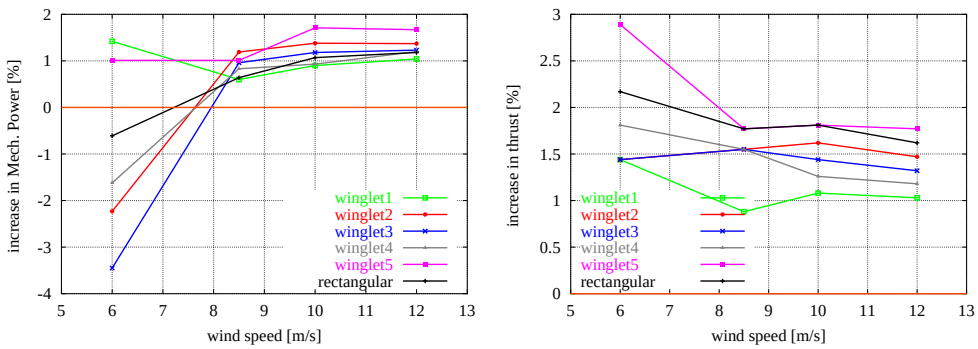

Figure 2-2: Increase/decrease in mechanical power (left) and thrust (right) compared to the original blade.

Based on the present investigation it is seen that *winglet2* has the best overall power performance of the upwind pointing winglets, but the increase in power of around 1.4% for wind speeds larger than 6 m/s is relatively low and must be compared to the increase in thrust of around 1.6%. But pointing the winglet downstream seems to increase the power production even further. (1.7% increase in mechanical power and 1.8% in thrust.) The effect of sweep and cant angles is not accounted for in the present investigation. This might improve the performance of the winglets even more, as well as other arbitrary configurations.

2.2 Transient loads during pitch motion

Time constants for transient loads are determined using both 3D CFD and Actuator Disc methods.

In connection with the design of wind turbines and their control algorithms, the transient loads, especially generated by time varying blade loads, are very important. In the Blade Element Momentum (BEM) method the time constants necessary to describe these problems are not an inherent part of the model. Transient aerodynamic loads are typically handled at two levels, unsteady airfoil aerodynamics, and the so called dynamic inflow models. The first part covers the unsteady non-separated effects from shed vorticity and the dynamic stall models. Phenomena which both deals with relatively fast motion with a time scale in the order of the chord divided by the velocity seen by the airfoil. The second part of the dynamic loads, the dynamic inflow, or dynamic induction, is phenomena related to variations in the inflow velocity, blade vibrations and tip pitch changes. The time scales important for this are of size rotor radius divided by the free stream velocity. In the present study the main focus is on the second part of these models namely the dynamic inflow models. The main area of concern is the influence on the damping properties in connection with dynamic instabilities and vibrations.

Two different approaches are used to determine the time constants, namely the EllipSys3D Navier-Stokes solver, and an actuator disc method. The time constants estimated by the actuator disc method are afterwards used in a standard BEM method and a BEM method coupled with a Near Wake (NW) method, where the unsteady trailed vorticity is included. In both BEM models the shed vorticity is modeled with the Beddoes-Leishman dynamic stall model. The resulting transients are compared to measured values, for a step pitch change taken from the unique data set of the NREL/NASA Ames experiment.

In the current work, one series of step pitch changes taken from The NREL/NASA Ames wind tunnel test is investigated using both a full 3D CFD code, and two versions of the BEM model, with the main focus of looking at the time constants for the settling of the loads. The work has been published in Ref. [3] and for further information the reader is referred to this.

Figure 2-3 (left) shows the computed shaft torque from the NREL/NASA Ames test using the EllipSys3D CFD code compared to the measured values. The overall agreement is reasonably good. For the 10 degrees tip pitch (t = [0:20] s), where a negative shaft torque is observed, the CFD code predicts a slightly larger negative torque at the equilibrium state, while the overall transient behavior except for the lack of oscillation agrees reasonably well with the measured curve. For the minus 6 degrees tip pitch (t = [20:40] s), where the turbine is heavily loaded, the shaft torque predicted by the CFD code is slightly lower, and the decay is slower than observed in the experiment. The difference in the decay rate may be connected to the extremely high axial induction in this situation, and the associated blockage effects. Concerning the high frequency oscillations seen in the measurements, these may be partly connected to torsion vibrations in the shaft, caused by the abrupt change in the shaft torque. As the model runs do not allow any structural deformations, these effects are not present in the computed results. Computed flapwise blade root moment using the engineering models and the experimental values are compared in the right side of Figure 2-3, showing excellent agreement, again the high frequency response seen in the experiments may be connected to structural vibrations of the turbine.

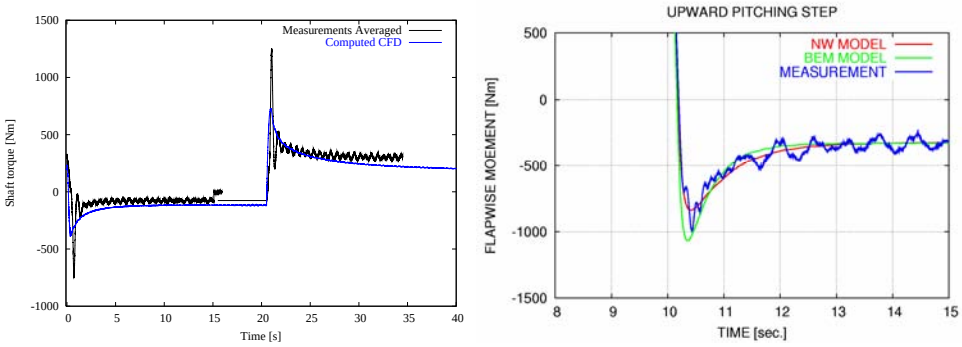

Figure 2-3: Left the figure shows comparison of the measured and computed shaft torque during step pitch changes, using the EllipSys3D code. At t=0 [s] the rotor is pitched from minus 6 to 10 degrees deloading the rotor, this is followed by a pitch step from minus 6 to 10 degrees initiated at approximately t=20 [s]. The right side of the figure shows comparison of the flapwise blade moment for the NW and the BEM model with the measurements, for a step from minus 6 to 10 degrees, deloading the rotor.

The wake velocity is used for normalization of the time constants

The time constants can subsequently be estimated from an exponential curve fit. In order for the BEM and NW models to reflect the influence of the thrust coefficient on the transient behavior normalization of the time constant using the velocity in the wake instead of the free stream velocity is used. Thereby, a more universal time constant for the slowest part of the dynamic inflow process is obtained.

The work also includes the investigation of the spanwise variation of time constants. By looking at the time histories of the local normal force at different radial positions results indicated that there was a limited radial variation for normal operation. See Ref [3].

2.3 Determination of angle of attack for rotating blades

A method for determining the 3D AOA has been developed

For a 2D airfoil the angle of attack (AOA) is defined as the geometrical angle between the flow direction and the chord. The concept of angle of attack is widely used in aero-elastic engineering models (i.e. FLEX and HAWC) as an input to tabulated airfoil data that normally are established through a combination of numerical calculations and wind tunnel tests and a correction for the effect of Coriolis and centrifugal forces in a rotating boundary layer. For a rotating blade the flow passing by a blade section is bended due to the rotation of the rotor, and the local flow field is influenced by the bound circulation on the blade. As a further complication, 3D effects from tip and root vortices render a precise definition of the AOA difficult. Today, a lot of experimental and numerical (CFD) data exist from which aerodynamic loads may be extracted. However, this leaves us with the problem of determining lift and drag polar as function of the local AOA.

A method for determining this AOA in standard operations and also in general flow conditions has been developed in Ref. [4]. The method needs to choose a convenient control point at each radial cross section and uses a point vortex to represent the bound circulation around an airfoil section. Since point vortex is singular at the centre of the vortex, the control point should not be too close to the airfoil. In order to overcome the difficulty, a new method is developed in this study. In the new method, a distributed circulation around the airfoil has been used instead of the point vortex. This local circulation is determined from the local pressure distribution. The procedure is:

1. The boundary layer edge velocity is determined using Bernoulli equation.
2. The local circulation is found by using the edge velocity and the definition of circulation.
3. The induced velocities created from the bound vorticity are determined from the circulation using the Biot-Savart law.
4. An AOA is determined from the velocities subtracted the induced velocities.

The method has been validated on operational conditions from the Tellus 95kW wind turbine from Risø and compared to previously developed models: The previous developed method from Ref. [4] and the Averaging Technique (AT) from Ref. [5]. Results are presented in Figure 2-4 and Figure 2-5 and good agreement between the models is obtained.

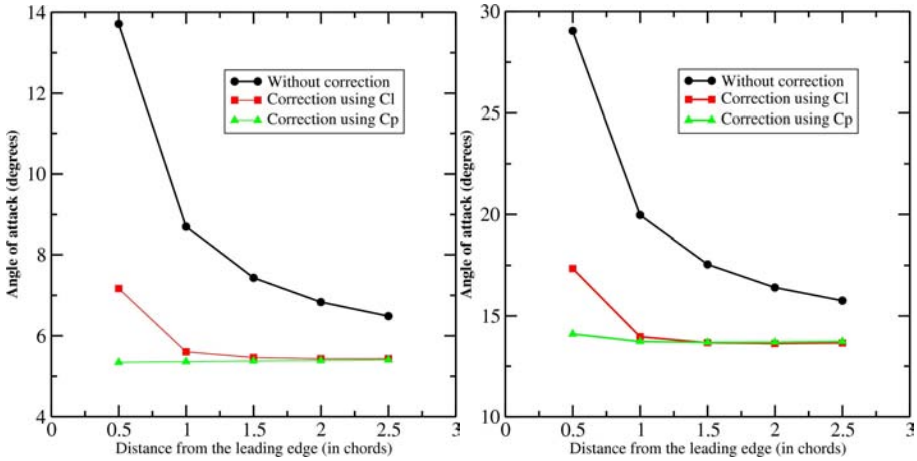

Figure 2-4: AOA as function of distance between the control point and the airfoil leading edge at wind speeds of 7 m/s (left) and 12 m/s (right).

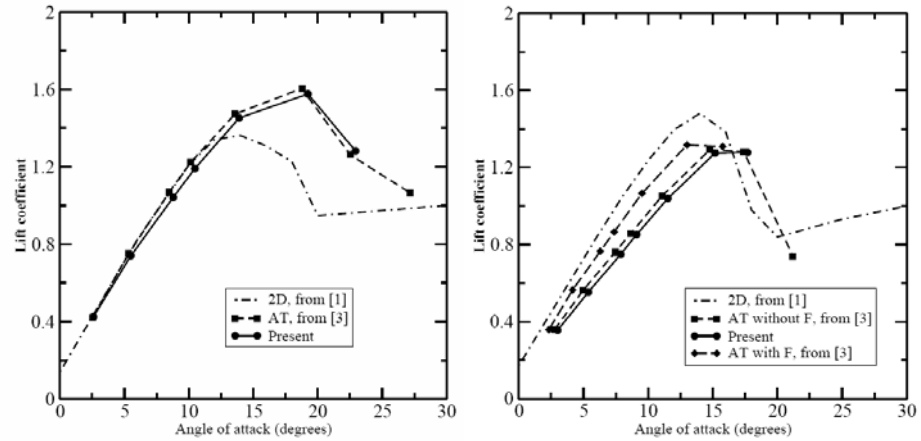

Figure 2-5: Lift coefficient at r/R=65.7% (left) and r/R=94.7% (right) compared to 2D and the AT method.

A general method for determining angle of attack has been developed, which can be used to extract 3D AOA from either measurements or numerical computational using CFD in all flow conditions. Moreover, it can be used to study airfoil characteristics in the region near the tip.

2.4 Modelling of the far wake behind a wind turbine

When wind turbines are clustered in a wind farm, the power production will be reduced due to the reduced free-stream velocity. However, an even more important impact on the economics of a wind farm is the increased turbulence intensity from the wakes of the surrounding wind turbines that increases the fatigue loadings. Even though many wake studies have been performed over the last two decades, a lot of basic questions still need to be clarified in order to elucidate the structure and dynamic behavior of wind turbine wakes. In the present work, various vortex models for far wakes are analyzed, resulting in the development of a new analytical wake model [6]. In the model the vortex system is replaced by N helical tip vortices of strength (circulation) Γ embedded in an inner vortex structure representing the vortices emanating from the inner part of the blades and the hub, Figure 2-6. A simplified model, in which the inner structure of the wake is represented by a single central vortex line of strength $-N\Gamma$, was firstly formulated by Joukowski (1912).

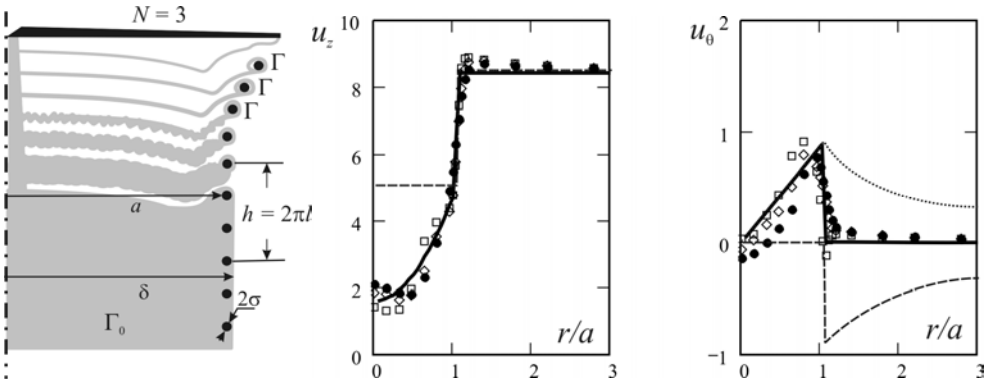

Figure 2-6: Example of a sketch (left) illustrating the new far wake model for propeller. (Middle and right): Comparison of experimental data [7] (symbols) with results from the new model. Middle: Axial velocity; Right: Tangential velocity. Thick lines: Velocity profiles computed by the model; Thin lines: Contribution from hub vorticity; Dashed lines: Contribution from tip vortices.

The developed model forms the basis for a supplementary work on stability of the tip vortices in the far wake behind a wind turbine (Figure 2-7). As examples of inner vortex fields, we consider three generic vorticity distributions (Rankine, Gaussian and Scully vortices) at radial extents ranging from the core radius of a tip vortex to several rotor radii. The analytical solution of the problem allows us to provide an efficient analysis of some of the experimentally observed stable vortex arrays in far wake behind multi-blade wind turbines.

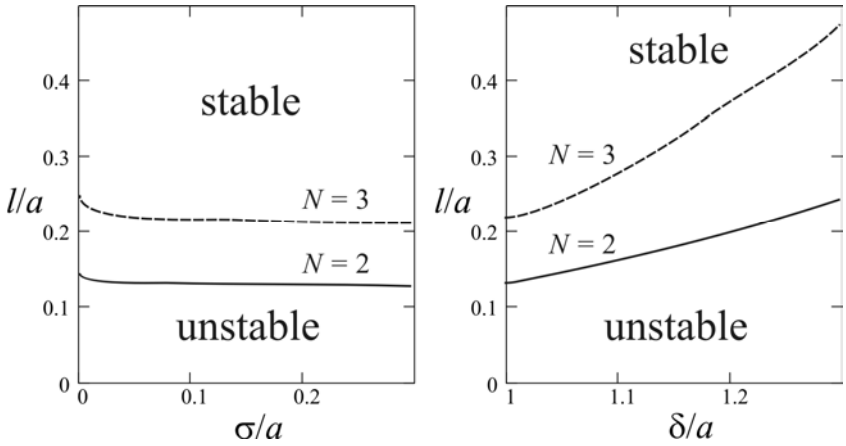

Figure 2-7: Neutral curves for far-wake model of Figure 2-6(left) with different numbers of tip vortices (N = 2, 3) as function of various wake parameters ($2\pi l$ – helical pitch of tip vortices; a *– radius of tip vortex system; σ - radius of tip vortex core; and δ - radius of hub vortex core.*

2.5 References

[1] J. Johansen and N.N. Sørensen, "Aerodynamic investigation of Winglets on Wind Turbine Blades using CFD", Risø-R-1543(EN), Risø National Laboratory, Roskilde, February, 2006.

[2] J. Johansen and N.N. Sørensen, "CFD modeling of winglets", IEA Annex XI/XX Joint meeting, Kiel, Germany, 25-26. April, 2006.

[3] N.N. Sørensen and H.Aa. Madsen, "Modelling of transient wind turbine loads during pitch motion" Poster at EWEC-2006, Athens, Greece, February 27th – March 2nd, 2006.

[4] W. Z. Shen, M. O. L. Hansen and J.N. Sørensen, " Determination of Angle of Attack (AOA) for Rotating Blades", EUROMECH, 2005

[5] J. Johansen and N.N. Sørensen, "Aerofoil Characteristics from 3D CFD Rotor Computations", *Wind Energy*, pp 283-294, vol. 7, issue 4 (October/December 2004).

[6] Sørensen J.N., Okulov V.L., Modeling of the Far Wake behind a Wind Turbine (invited lecture), *Abstract of Euromech Colloquium 464b "Wind Energy"* October 4-7, 2005, University of Oldenburg, Germany, p. 43

[7] D. Medici, P.H. Alfredsson (2004) Measurements on a wind turbine wake: 3D effects and bluff-body vortex shedding, In *The Science of making Torque from Wind* (ed. G.A.M. van Kuik) pp. 155-165. DUWIND, Deft University of Technology

3 Inboard rotor/blade aerodynamics and its influence on blade design

Helge Aagaard Madsen, Robert Mikkelsen, Jeppe Johansen, Christian Bak, Stig Øye, Niels N. Sørensen

A thorough study has been carried out in order to analyze the inboard rotor/blade aerodynamics and its influence on blade design. Besides the summary of the work in the present report a presentation was given at the EWEC-2006 [1] and a paper in the Journal Wind Energy is to be submitted [2]. Finally, the main results are also summarized in a fact sheet [3].

3.1 Background and motivation for the work

The aerodynamic design of wind turbine rotors and blades is typically done with a model where the aerodynamics are computed with the Blade Element Momentum (BEM) model. Furthermore, another characteristic is that the aerodynamic design has developed to be one part of an integrated design process involving consideration of loads on the complete turbine, cost modeling of the different turbine components as well as energy production. The design goal then ends up in maximizing energy production relative to the wind turbine cost. This is a complex design and optimization process which e.g. can be performed with the design tool "HAWTOPT" [4].

Figure 3-1 *Graph showing loss in power coefficient by thrust coefficient CT deviating from 0.89 which is the value at which CP_{max} =0.59 is achieved according to the BEM theory.*

Such an integrated design process where the optimal solution is a design with reduced loads combined with a high aerodynamic performance will typically not result in a design point at the maximum rotor power coefficient $CP_{max.}$ which is obtained at a rotor thrust coefficient CT=0.89 according to the BEM theory. The loss in CP when running at a reduced CT is shown in Figure 3-1 and it appears that if CT is reduced to e.g. 0.8 (a reduction of about 10%) the corresponding reduction of CP is only reduced 2-3%.

Typically, the aerodynamic design is not exactly at CP_{max}

Motivation for the work is the renewed interest in designs with maximum CP

However, recently there has been renewed interest from the industry in aerodynamic rotor designs with the main focus on maximum CP. This is partly due to the new Enercon design [5] which should have a considerable higher aerodynamic efficiency compared to an older Enercon rotor.

Another part of the motivation for the work is that it is well-known that the BEM model which being the most common design model, is derived on basis of a number of assumptions on the flow properties through the rotor and in the wake. In particular the uncertainty is high on the inboard part of the rotor where the local velocity ratio $\lambda_l = \frac{r\Omega}{V}$ is low.

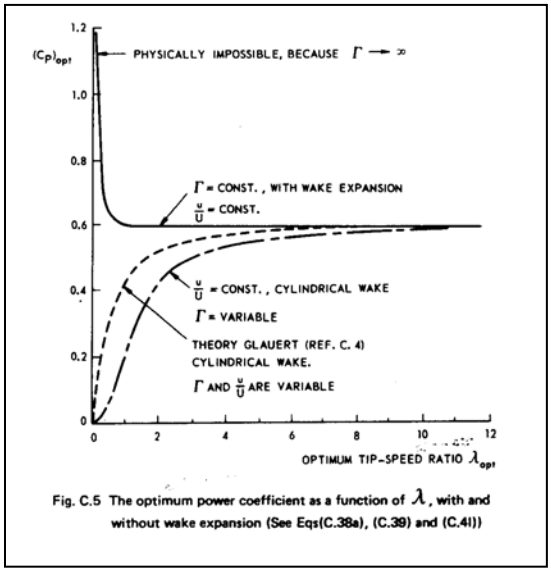

Fig. C.5 The optimum power coefficient as a function of λ, with and without wake expansion (See Eqs(C.38a), (C.39) and (C.41))

Figure 3-2 *The influence on the rotor power coefficient CP from the pressure variation in the wake due to wake rotation and from the influence of wake expansion as derived by de Vries [6].*

de Vries [6] has considered the influence of making other assumptions than Glauert [7]. One main issue is how the pressure variation from wake rotation (tangential induction) is handled. Glauert disregards this pressure variation and we get a reduced CP at decreasing λ_l due to the loss by rotation of the wake (dashed line in Figure 3-2). However, for a constant loaded disc de Vries [6] has shown that that CP remains constant for decreasing λ_l and even could increase for very low λ_l (solid line in Figure 3-2).

The main objective with the study is to clarify the uncertainties in the BEM code used for rotor design

The main objective of the present investigations has therefore been to clarify these uncertainties by using detailed models and to access the influence on maximum rotor efficiency and the influence on the rotor/blade design.

In section 3.2 we present two analytical derivations which show how the pressure term from wake rotation influences the flow through the rotor and the power conversion. Then follows in section 3.3 a brief description of the models used for the numerical simulations. The influence from the pressure variation from wake rotation is illustrated in section 3.4 on basis of different numerical results. Then follows a short description on how to modify the BEM code in order to take into account the pressure term caused by wake rotation. We then discuss what the maximum obtainable power coefficient for a rotor is and how the rotor loading should be. Next the influence of using a spinner is

considered and finally, we show results from numerical simulations including full 3D CFD simulations on different rotor designs

3.2 Two analytical solutions for the description of the influence from the pressure term caused by wake rotation

Influence on the rotor power coefficient, de Vries 1979 [6]

By using momentum considerations and introducing appropriate assumptions de Vries presents the following indication of the cancellation of the power loss due to wake rotation with the positive effect on the power conversion caused by the pressure component from wake rotation.

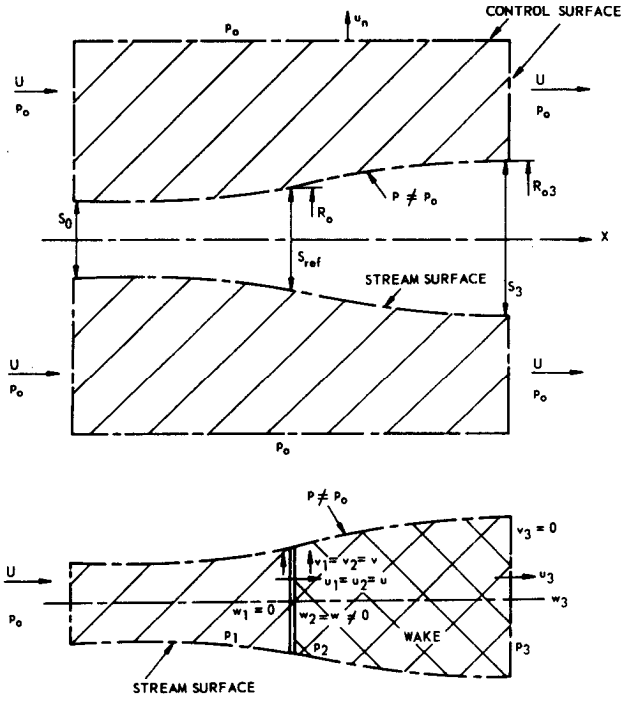

Fig. C.3 Control volumes for momentum considerations

Figure 3-3 *The notation used by de Vries 1979 [6] for momentum considerations on a stream tube around a rotor.*

The power conversion can be written as:

$$dP = \Omega\, dQ = u\, dD - \frac{1}{2}\frac{w}{r} dQ \qquad (3\text{-}1)$$

which states that the shaft power ($\Omega\, dQ$) is equal to the work done by the fluid which is the positive work by the axial force $(u\, dD)$ and the negative work by the torque $(\frac{1}{2}(w/r)\, dQ)$ where w is the tangential velocity downstream the rotor disc.

The axial force consists of a momentum term and a pressure term from the wake rotation here with reference to the far wake conditions:

$$dD = \rho u\left(U - u_3\right) dS_{ref} + \Delta p_3\, dS_3 \qquad (3\text{-}2)$$

Angular momentum yields the equations:

$$dQ = \rho u_3 w_3 r_3\, dS_3 = \rho u\, w r\, dS_{ref} \qquad (3\text{-}3)$$

From *(3-3)* we get:

de Vries has shown that the power losses due to wake rotation almost cancel due to the positive influence of the pressure term from wake rotation

$$-\frac{1}{2}\frac{w}{r} dQ = -u\frac{1}{2}\rho w^2\, dS_{ref} \qquad (3\text{-}4)$$

Now de Vries makes the following approximation:

$$\Delta p_3\, dS_3 \approx \frac{1}{2}\rho w_3^2\, dS_3 \approx \frac{1}{2}\rho w^2\, dS_{ref} \qquad (3\text{-}5)$$

This means that the positive energy conversion from the $\Delta p_3\, dS_3$ term in (3-2) cancels the loss of energy term $-u\frac{1}{2}\rho w^2\, dS_{ref}$ from wake rotation resulting in a higher power coefficient.

Influence of pressure from wake rotation analyzed with a distributed vortex method

An alternative way to analyze the rotor flow is based on the use of a vortex model. The idealized wind turbine is modeled with an infinite number of blades, each represented by a lifting line with constant vortex strength from the root to the tip. The total bound vortex strength of all the blade is Γ. Figure 3-4 depicts the system of trailing vortices from the root and the tip.

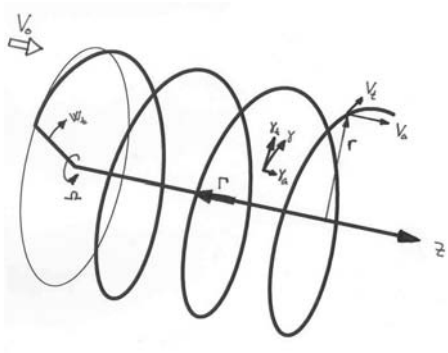

Figure 3-4 Wake geometry with one trailing tip vortex

The infinite amount of lifting lines forms a sheet of vorticity assuming a ball-bearing analogy with constant vortex strength. The vortex sheet is divided into an axial and tangential component, γ_a and γ_t, respectively, where

$$\gamma_t = \frac{\Gamma}{2\pi R}\frac{R\Omega + V_t}{V_a} = 2w_a \quad , \quad \gamma_a = \frac{\Gamma}{2\pi R} = 2V_t = 2w_t \quad , \quad V_a = V_o - w_a \,. \qquad (3\text{-}6)$$

where w_a and w_t is the axial and tangential induced velocity at the disc.

Note that the combined assumptions of a cylindrical wake and a constant pitch of the trailing vortex sheet, results in a model which produces a constant axial induced velocity w_a over the disc. The relation between the total bound vortex strength Γ and w_a can be found by solving the above equations for Γ. The total vortex strength and corresponding axial and tangential loadings are then given by

$$\Gamma = 2\pi R\left(-R\Omega + \sqrt{R^2\Omega^2 + 4w_a(V_o - w_a)}\right), \qquad (3\text{-}7)$$
$$F_a(r) = \rho\cdot\Gamma\cdot(\Omega r + w_t), \quad F_t = \rho\cdot\Gamma\cdot(V_o - w_a)$$

Introducing the usual non-dimensional local thrust and power coefficient C_T and C_{Pmek}, explicit expressions may be derived as

$$C_T(r) = \frac{F_a}{\frac{1}{2}\rho V_o^2\cdot 2\pi r} = 4a(1-a)\frac{\Omega + \frac{\Gamma}{4\pi r^2}}{\Omega + \frac{\Gamma}{4\pi R^2}}$$
$$= 4a(1-a) + \Delta C_T, \quad \Delta C_T = \left(\frac{\Gamma}{2\pi V_o}\right)^2\left(\frac{1}{r^2} - \frac{1}{R^2}\right) > 0 \qquad (3\text{-}8)$$
$$C_{P_{mek}} = \frac{F_t\cdot\Omega\cdot r}{\frac{1}{2}\rho V_o^3\cdot 2\pi r} = 4a(1-a)^2\frac{R\Omega}{R\Omega + w_t}$$

The thrust coefficient increases towards the root section for constant induction

showing that the added term ΔC_T, compared to classic axial momentum theory, increases towards the root section. Figure 1-3 displays computed distribution from the above expressions as function of λ=2, 5 and 8, with constant induced velocity w_a=1/3.

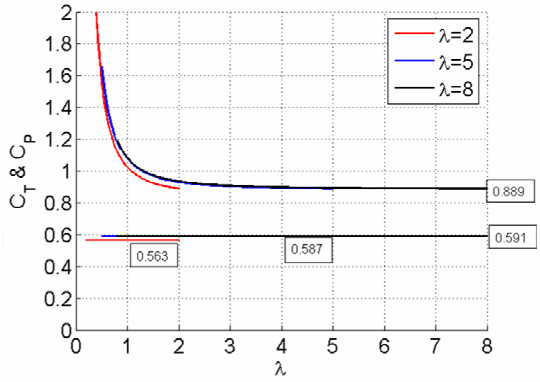

Figure 3-5 Distribution of local CT and CP as function of the velocity ratio λ.

The increased loading captured by the model, becomes singular at the root section, thus predicting infinite axial loading for r→0. Closer inspection of the radial pressure gradient due to the centrifugal acceleration yields

$$\frac{dp}{dr} = \rho\frac{w_t^2}{r} = \rho\frac{\Gamma^2}{4\pi^2}\cdot\frac{1}{r^3} \quad\Rightarrow\quad \Delta p_c = \rho\frac{\Gamma^2}{4\pi^2}\int_r^R\frac{1}{r^3}dr = -\rho\frac{\Gamma^2}{8\pi^2}\left(\frac{1}{R^2} - \frac{1}{r^2}\right) \quad\Rightarrow \qquad (3\text{-}9)$$
$$\Delta C_{T_c} = \frac{\Delta p_c}{\frac{1}{2}\rho V_o^2} = \left(\frac{\Gamma}{2\pi V_o}\right)^2\left(\frac{1}{r^2} - \frac{1}{R^2}\right)$$

The mechanical power does not vary with radii

revealing that a low pressure is present in the wake, corresponding exactly to the expression derived previously. In other words, the low pressure due the centrifugal acceleration should be included into the axial momentum equation. The mechanical

power does not vary with radii and is seen to decrease slightly with increasing tip speed ratio. Regarding the limitations of the model, the wake is prescribed thereby assumed not to expand. The model appears promising in terms of serving as an improvement to the classical BEM model. Presently, however, the model still needs to mature further before in can be incorporated into the BEM method, mainly because the circulation is constant in the above derivation. Real blades have varying circulation and the number of blades is finite, meaning that tip correction is needed as well as some kind of root correction since finite trailed vortex lines are released at the root section too. Further details about the vortex model may be found in Øye (1990) [8].

3.3 Overview of the numerical modeling used in the analysis

In the numerical analysis we have made use of three model types which will shortly be described below.

Actuator disc and BEM modeling

The BEM model will not be described here as it is a well-known model. The actuator disc (AD) model is based on the same physical model of the wind turbine rotor as the BEM model. This is the actuator disc but the simulation of the flow field through the disc is now performed with a CFD code, which solves the full set of equations for the flow. In this way the actuator disc AD model can be used for validation of the BEM model where assumptions are introduced in derivation of the final set of equations as discussed in section 3.2.

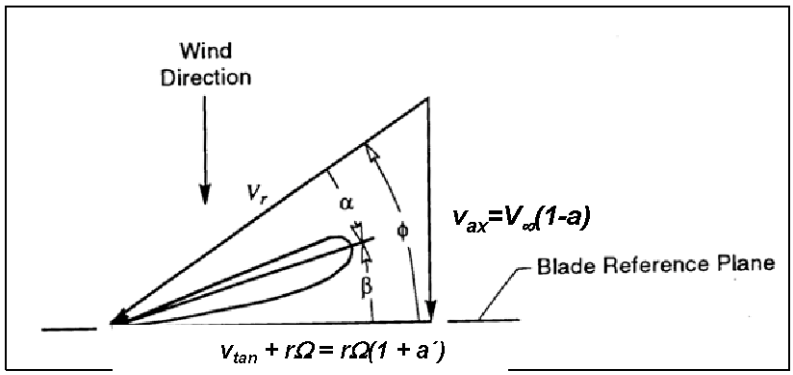

Figure 3-6 The notation used for the velocity components at the blade section

Two different AD models have been used in the analysis; one at Risoe where the commercial CFD code FIDAP is used to compute the flow field; and another actuator disc model at DTU where an in-house developed CFD code based on the vorticity-stream function formulation is used.

In the following a short description is presented on how the loading on the rotor disc is derived and how it is applied on the flow.

The projections of the lift and drag coefficients perpendicular and tangential to the rotor plane, respectively, are denoted C_y, C_x and are derived as (see Figure 3-6 for notation)

$$C_y = C_L \cos(\phi) + C_D \sin(\phi) \qquad (3\text{-}10)$$

and

$$C_x = C_L \sin(\phi) - C_D \cos(\phi) \qquad (3\text{-}11)$$

The infinitesimal thrust dT on an infinitesimal radius dr can be written as:

$$dT = \frac{1}{2}\, \rho v_r^2\; C_y\, c\, N_B\; dr \qquad (3\text{-}12)$$

where:

v_r is the relative velocity to the blade section

ρ density of mass

c chord length

N_B number of blades

Likewise the infinitesimal torque dQ is derived as:

$$dQ = \frac{1}{2}\, \rho v_r^2\; C_x\, c\, N_B\; r\; dr \qquad (3\text{-}13)$$

We then derived the local thrust coefficient *CT*:

$$CT = \frac{dT}{\frac{1}{2}\rho V_\infty^2\; 2\pi r\, dr} = \frac{v_r^2\, C_y\, c\, N_B}{V_\infty^2\, 2\pi r} \qquad (3\text{-}14)$$

and the local torque coefficient CQ:

$$CQ = \frac{dQ}{\frac{1}{2}\rho V_\infty^2\; r\, 2\pi r\, dr} = \frac{v_r^2\, C_x\, c\, N_B}{V_\infty^2\, r\, 2\pi} \qquad (3\text{-}15)$$

where V_∞ is the free stream velocity

Finally, we derive the ratio between the *CT* and *CQ*:

$$\frac{CQ}{CT} = \frac{\frac{dQ}{r}}{dT} = \frac{C_x}{C_y} = \tan(\phi) \;\Rightarrow\; CQ = CT\, \tan(\phi) \qquad (3\text{-}16)$$

This equation shows that if we specify a rotor loading by CT then we shall apply a corresponding tangential loading CQ specified by equation (3-16). However, as the tangential loading depends on the actual flow angle ϕ (see Figure 3-6), which is unknown, an iteration loop is necessary in order to reach the final result.

The energy conversion is studied by specifying a loading

We can now study the energy conversion on a rotor simply by specifying the loading expressed by CT and CQ, respectively, without considering how the load is actually created. However, if we then have found a load distribution and the corresponding flow field (induction), a blade design can be derived according to eq. (3-12). It should be noted that in the following all variables are non-dimensionalized as follows:

$v^* = v/V_\infty$, $r^*=r/R$, $p^* = p/\left(\tfrac{1}{2}\rho V_\infty^2\right)$ but * is not shown in the following.

We now define a shaft power coefficient CP_s as:

$$CP_s = CQ\, r\,\Omega \qquad (3\text{-}17)$$

However, we can also define the power coefficients for the power conversion in the fluid as:

$$CP_{ax} = CT\, v_{ax} \qquad (3\text{-}18)$$

and

$$CP_{\tan} = v_{ax}\, v_{\tan}^2 \qquad (3\text{-}19)$$

where:

v_{ax} is the axial velocity through the actuator disc

and

v_{tan} is the tangential flow velocity behind the disc

CP_{ax} is the power coefficient for extraction of power from the flow whereas CP_{tan} is the power coefficient for power added to the fluid due to the rotation of the wake. The difference between CP_{ax} and CP_{tan} is the total power coefficient CP_{tot} and must then be equal to the shaft power coefficient:

$$CP_{tot} = CP_{ax} - CP_{\tan} = CP_s \qquad (3\text{-}20)$$

Full 3D CFD analysis with EllipSys3D

Full 3D CFD computations used to analyze specific designs

Finally, to represent more accurately the real geometry, the three-dimensional flow and a more physical representation of the viscous drag full 3D CFD computations are performed with the incompressible Navier-Stokes solver EllipSys3D. The code is developed by Michelsen [9], [10] and Sørensen [11] and is a multiblock finite volume discretization of the incompressible Reynolds Averaged Navier-Stokes equations in general curvilinear coordinates. Using CFD the only input to the computations are the rotor geometry and the operational conditions. No assumptions are made regarding airfoil data or tip corrections.

3.4 The influence of wake pressure from wake rotation

In this section we will illustrate the influence of the pressure term from wake rotation which was discussed in section 3.2 and which is the term that is not included in the BEM model as derived by Glauert. We will therefore compare a BEM solution and an AD solution for the same loading (constant load form except close to the rotor axis) and see what the differences are.

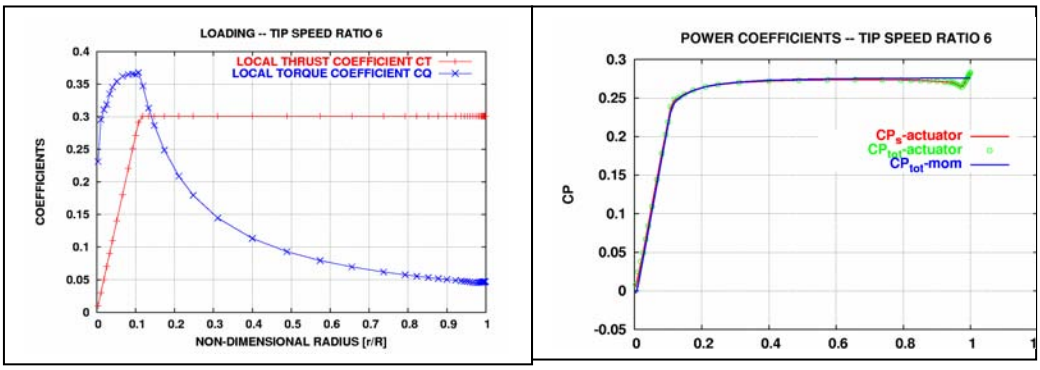

Figure 3-7 *The loading corresponding to CT=0.3 is shown in the left figure. To the right the comparison of local CP_{tot} computed by the BEM model and the AD model, respectively, shows good correlation.*

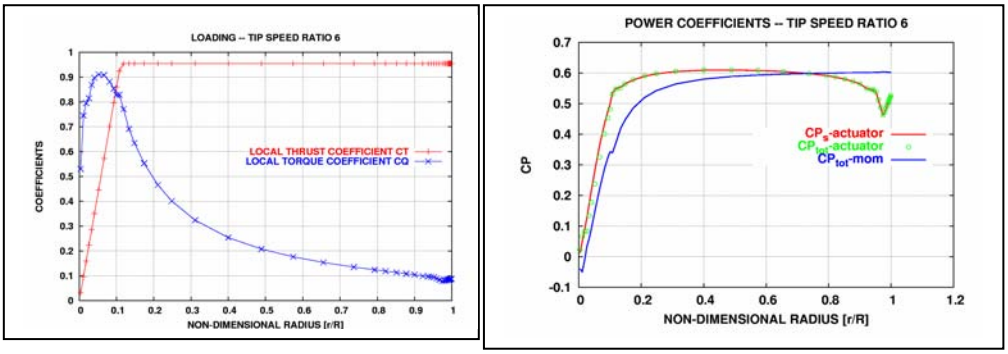

The BEM model underestimates CP on the inboard part of the blade and overestimates CP at the tip

Figure 3-8 *The loading corresponding to CT=0.95 is shown in the left figure. To the right it is seen that the BEM model underestimates the local CP_{tot} considerably when compared with the AD model whereas the opposite tendency is seen in the tip region.*

For a low loading with CT=0.3 there is a good correlation between local CP_{tot} computed with the two models as shown in Figure 3-7. However, at a high loading at CT=0.95 the BEM model underestimates the local CP_{tot} considerably on the inboard part of the blade, Figure 3-8. The underestimation of CP_{tot} is due to a lower axial velocity (higher induction) through the disc computed with the BEM model, left figure in Figure 3-9. However, if CP_{tot} is integrated over the entire rotor disc as shown to the right in Figure 3-9 the AD and BEM model gives almost the same total power coefficient for the rotor. This means that the underestimation of CP_{tot} on the inner part of the blade is counterbalanced by overestimation of CP_{tot} in the tip region.

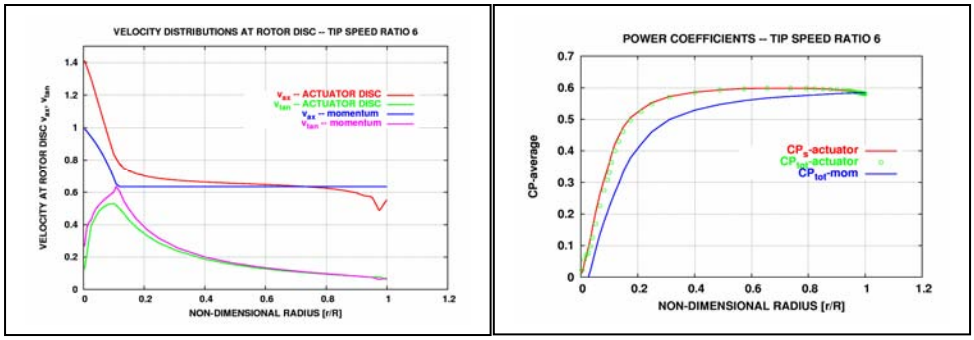

Figure 3-9 *Comparison of the axial and tangential velocities as computed with the AD and BEM model respectively, for CT=0.95. To the right is shown the accumulated CP_{tot} as function of radius for the same two models.*

Wake rotation decreases the pressure in the wake close to the rotor axis and this causes increased axial velocity on the inboard part of the rotor

Below we will illustrate that the underestimation of the axial velocity by the BEM model on the inner part of the blade is due to neglecting the pressure term from the wake rotation.

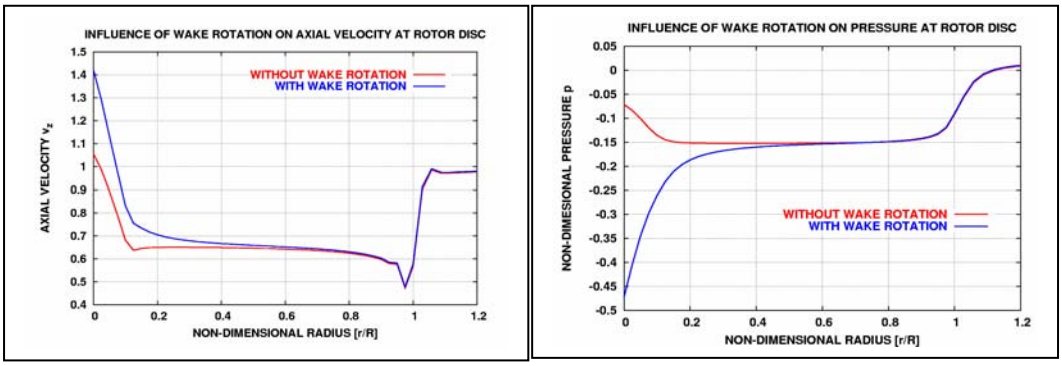

Figure 3-10 *To the left the axial velocity as computed with the AD model for a constant loading, with and without wake rotation (no wake rotation simulated by setting the tangential loading equal to zero). To the right the pressure variation for the two cases.*

We made two simulations with the AD model for a constant loading; one with the tangential loading and thus with wake rotation and one without the tangential loading. Comparing the axial velocity distribution for the two cases as shown to the left in Figure 3-10 it is seen that the wake rotation causes higher axial velocities through the disc. The pressure deficit from wake rotation is clearly seen in the pressure graph to the right in Figure 3-10. Finally, the influence of wake rotation on the pressure contours in the wake is shown in Figure 3-11.

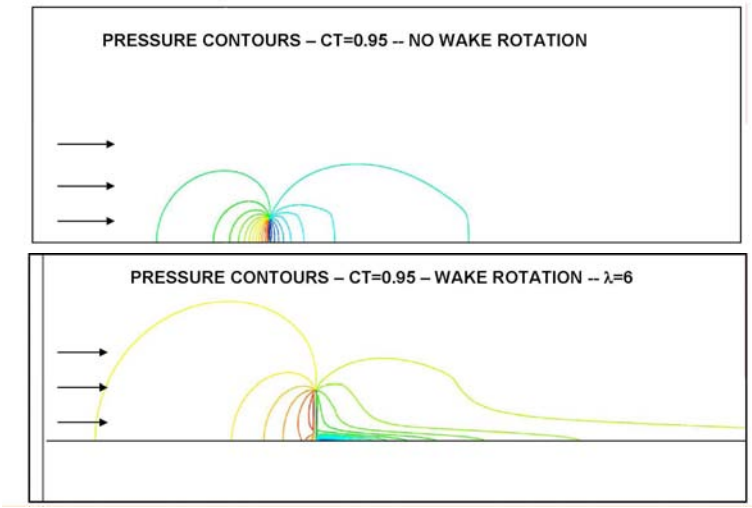

Figure 3-11 Influence of wake rotation on pressure contours.

3.5 A simple method to include the influence of wake pressure from wake rotation in the BEM code

In the section above we illustrated the close relation between the pressure term from the wake rotation and the increased axial velocity through the disc. On this background we have developed a simple modification to the BEM model so that the influence of the pressure term from the wake is include.

The pressure term from the wake rotation is computed as:

$$p_{wake} = -\int_1^r \frac{v_t^2}{r} dr \qquad (3\text{-}21)$$

where v_t is the tangential velocity computed in the BEM code: $v_t = a' r\Omega$. The minus sign on the integral indicates a pressure deficit. It should be noted that all the variables are non-dimensionalized as described in 3.3 and the integration is from the rotor tip (r=1) to r.

From the linearized equations for the actuator disc flow (Glauert [7] pp 365) we have:

$$\frac{\partial v_{ax}}{\partial x} = -\frac{\partial p}{\partial x} + X \qquad (3\text{-}22)$$

where X is the axial volume force. Integrating this equation, the velocity correction term $v_{ax-wake}$ should be equal to p_{wake}. However, comparisons with the numerical results from the AD model indicates that it is not the full pressure deficit that is converted to an increased velocity. The following relation gives the best correlation with numerical AD results:

$$v_{ax-wake} = 0.7\, p_{wake} \qquad (3\text{-}23)$$

The factor 0.7 has been tested for a number of different loadings and the reason why the full conversion from pressure to velocity is not obtained is probably due to the second order terms disregarded in equation (3-23)

The final axial velocity in the BEM code is then:

$$v_{ax} = (1-a) + v_{ax-wake} \qquad (3\text{-}24)$$

A few iterations inside the BEM model are now needed as the wake pressure depends on the corrected axial velocity.

A simple correction of the BEM model for the influence of the pressure term from wake rotation has been proposed

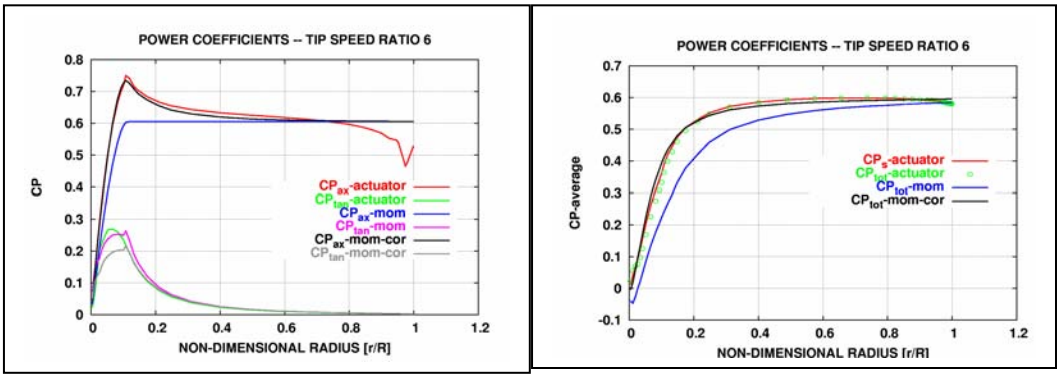

Figure 3-12 *The effect of the correction of the BEM model to include an additional velocity term from the wake pressure due to wake rotation. Correlation with the AD model is now excellent on the major part of the blade, both for the velocities shown to the left and the accumulated power coefficient to the right. However, the decrease in velocity at the tip of the blade is not modeled with the BEM code.*

The results with the BEM code with the described modification show excellent agreement with the AD model on the major part of the blade, both for the velocities as shown to the left in Figure 3-12 and the accumulated power coefficient shown to the right. However, the reduced inflow velocity in the tip region is not seen in the BEM model and this has the effect that the integrated power coefficient over the rotor is slightly above the AD results. This means that if the correction for the pressure on the inboard part of the blade is included, a modification should also be introduced in the BEM model for the reduced inflow in the tip region. One of the major causes of the reduced inflow in the tip region is thought to be due to the wake expansion. A method to correct for this is under development.

3.6 What is the maximum power coefficient for a rotor and what is the corresponding loading ?

Three different loadforms have been investigated

One of the main goals for the present research work on the rotor aerodynamics has been to investigate what the maximum power coefficient is for a rotor in the light of the increased power coefficient on the inboard part of the rotor from wake rotation as presented here. We have used AD simulations coupled to a numerical optimization routine but it turned out to be very difficult for the optimizer to find an optimal loading.

This indicates that the optimum is very flat. We have therefore used a more simple approach in the way that we have investigated different specific loadforms. First, we will present the loadings (they depend on the tip speed ratio) corresponding to constant axial induction which probably is the optimal loadform. Then we will also present the results for two other loadforms; 1) the constant loading and 2) a load where the load is highest on the mid part of the blade.

Loading corresponding to constant induction simulated with the DTU AD model

An incompressible, axi-symmetric Navier-Stokes model is used to analyze an actuator disc loaded to have constant induction a=1/3. The normal procedure using Navier-Stokes methods is to apply a known loading and compute the associated flow field. An inverse approach is pursued in the following in order to derive loadings producing constant axial induction, a=1/3, using Navier-Stokes. A numerical solution of the streamline patterns is depicted in Figure 3-13 with a vertical line indicating the axi-symmetric actuator disc.

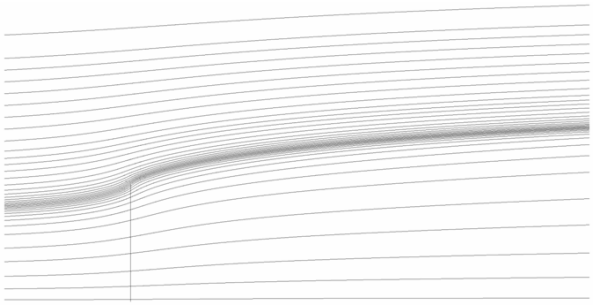

Figure 3-13 *Computed streamline patterns around loaded actuator disc, (axi-symmetric).*

Applying a purely axial loading does not result in corresponding axial induction. Figure 3-14, right, shows computed distribution for local C_T=0.4-1.0. Towards the tip or edge of the actuator disc the induction increases with increasing C_T, hence, in order to obtain constant axial induction the loading should be reduced slightly towards the tip. On the

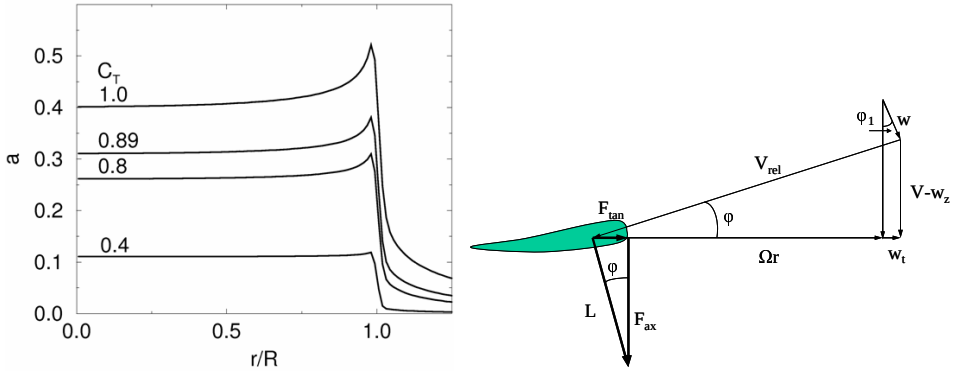

Figure 3-14 *Axial induction for a constant load actuator disc (left) and velocity triangle (right).*

other hand the previous analysis with the vortex method predicts that the loading should increase towards the root. Figure 3-14, left, displays the velocity triangle with

corresponding forces including the lift force normal to the relative velocity vector. Drag is not included in the present analysis.

In order to obtain an actuator disc with constant induction, the axial force component F_{ax} is adjusted using an under relaxation approach in the iterative solution process. The corresponding tangential force component is derived from the flow angle, which again is measured from the numerical solution. Figure 3-15, left shows the computed axial induction and Figure 3-15, right, the tangential velocity component for three different tip speeds λ. A 'cut of' radii of 0.15R is needed in order to obtain numerical convergence, since the solution becomes singular at r→0. Below the 'cut of' an increased axial velocity is found due to the low pressure as a result of the rotation.

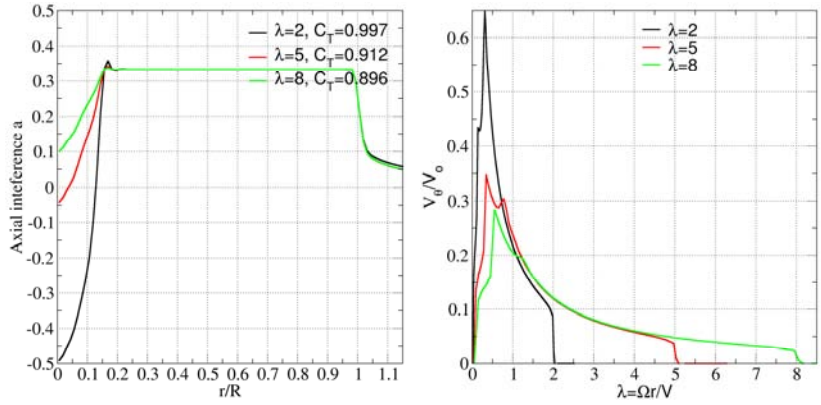

Figure 3-15 Constant axial induction (left), tangential velocities, λ=2, 5 and 8.

Corresponding distribution of thrust and power coefficient, C_T and C_P, are displayed in Figure 3-16. With the coefficients defined as

$$C_T(r) = \frac{F_{ax}}{\frac{1}{2}\rho V_o^2 2\pi r}, \quad C_P(r) = \frac{F_{ax} \cdot V_z}{\frac{1}{2}\rho V_o^3 2\pi r}, \quad C_{P_{mek}}(r) = \frac{F_{\tan} \cdot r \cdot \Omega}{\frac{1}{2}\rho V_o^3 2\pi r}$$

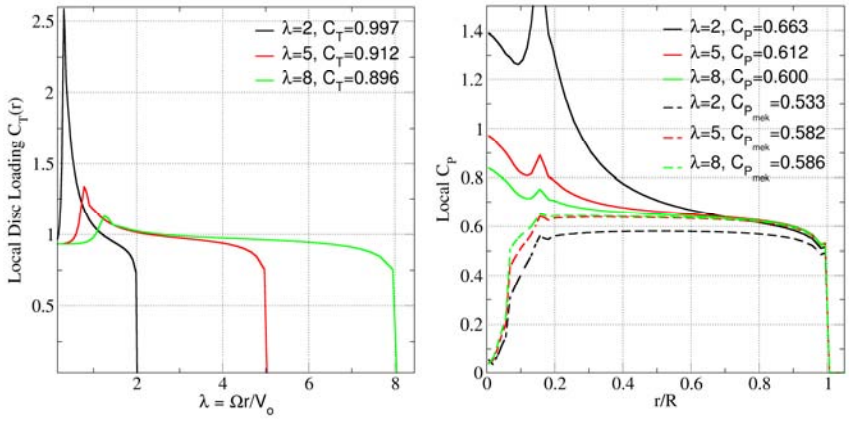

Figure 3-16 Left, local thrust coefficient corresponding to constant induction at three different tip speed ratios. Right, local power coefficients. Values in the figures are disc-average for CT, CP and CP_{mek}.

The two different power coefficients referrer to the kinetic energy and the shaft power, C_P and C_{Pmek}, respectively. Whereas the shaft power coefficient serves as the actual

usable energy conversion, the kinetic refers to the axial force (needed to establish the Betz-limit).

The values included into Figure 3-16 are the average over the actuator disc. Looking at the thrust coefficient, the loading varies across the disc from below C_T=0.89 at the tip to significantly above C_T=1.0 towards the root section, which corresponds well with the vortex analysis. The local C_{Pmek} is found to be well above the Betz limit (about 0.63) but the average value is found not to exceed the limit for the mechanical power coefficient. The average kinetic power coefficient is clearly above due to the increased axial loading. The higher value of the kinetic power coefficients also refers to the added kinetic energy in the wake given by the rotation.

The loadform for constant induction gives a maximum CP slightly above 0.58

Other Loadings simulated with the Risoe AD model

As mentioned in the introduction to this section we have also analyzed the constant loading and a loading with a maximum on the mid part of the blade. However, we also here present the solution for a constant induction as this is with another AD model, and we thus can see if the two model set-ups give comparable results.

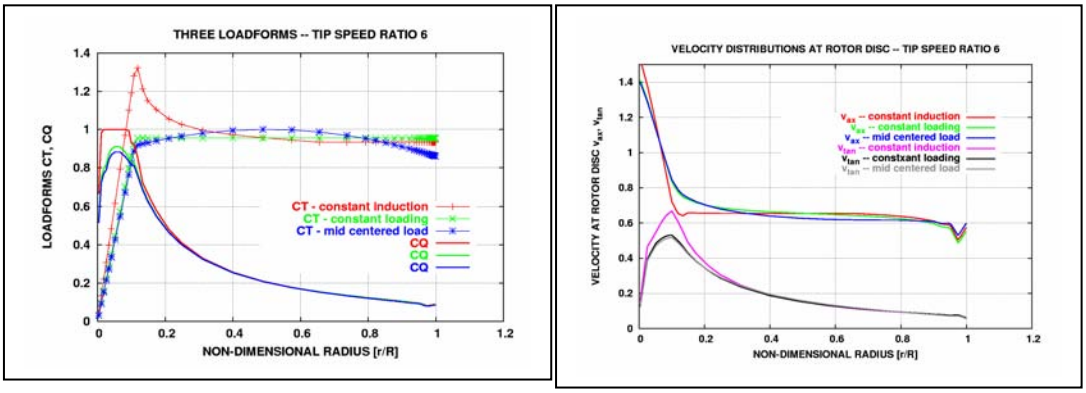

Figure 3-17 *To the left the three loadforms investigated with the AD model. To the right the axial and tangential velocity distributions.*

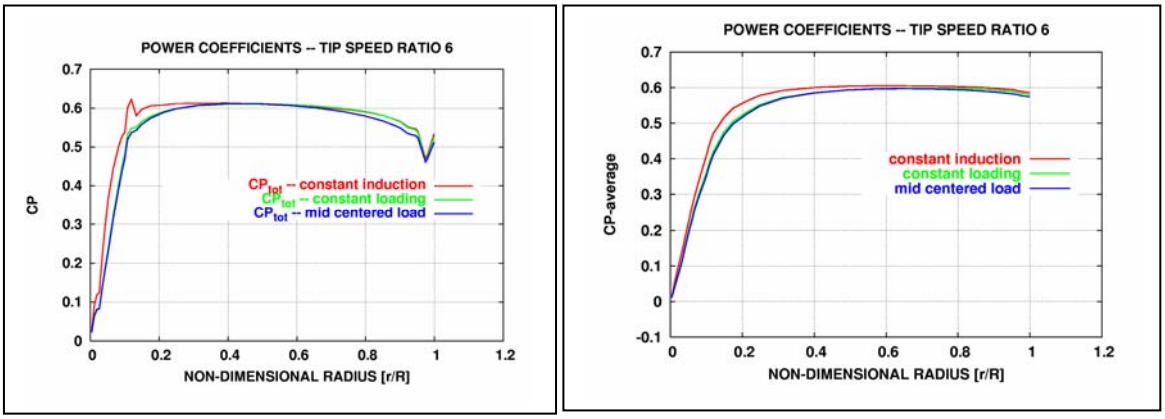

Figure 3-18 *The local power coefficients to the left and to the right the accumulated total CP for the three loadforms.*

The different loadforms give almost the same maximum CP

The three loadforms shown to the left in Figure 3-17 corresponds all to a total CT of 0.95. For the constant induction the load has to be increased considerably on the inner part of the rotor as shown earlier. It is also interesting to note that, although there is a

positive loading on the very inboard part of the rotor, the axial velocity increases above the free stream velocity in this region. The loadform corresponding to constant induction is seen to yield a higher local CP on the inner part of the rotor as can be seen in the left figure of Figure 3-18. However, when the local CP is integrated up over the rotor the three loadforms give almost the same CP; 0.584 (constant induction), 0.581 (constant loading) and 0.574 (mid centered load).

The influence of tip correction and blade drag

We have now seen that the maximum power coefficient for the ideal energy conversion in rotor is around 0.584 (tip speed ratio 6) based on a numerical model. But what is the corresponding maximum power coefficient for a real rotor then ?

The ideal energy conversion that we have investigated deviates from the real energy conversion by neglecting the tip losses and the losses from blade drag. Below, the reduction in CP from these two loss terms will be investigated.

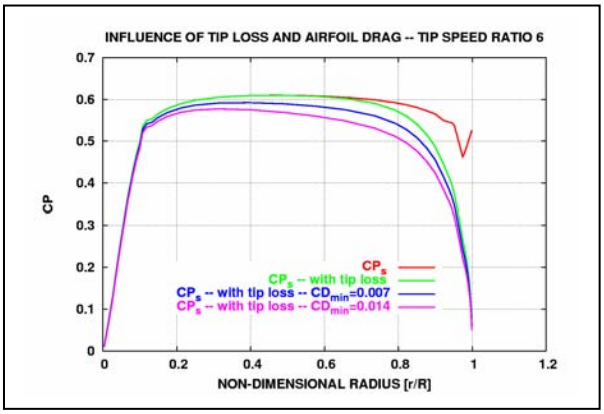

Figure 3-19 *The influence of tip losses and blade drag on the local power coefficient. Constant loading at CT=0.95.*

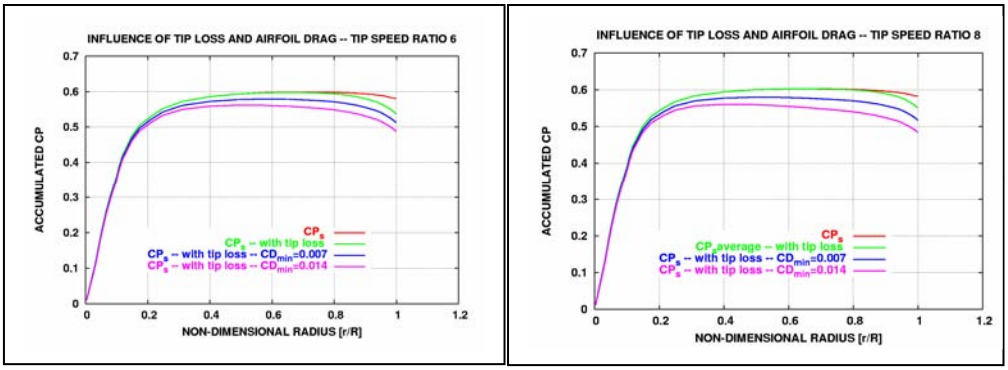

Figure 3-20 *The influence of tip speed ratio on the accumulated power coefficient including tip losses and blade drag. Constant loading CT=0.95*

The tip losses reduce the power coefficient considerably

The tip losses reduce the local power coefficient considerably on the outboard part of the blade as seen in

Figure 3-19. On the other hand the losses from drag are distributed over the major part of the blade. A minimum blade drag of 0.007 is close to the lowest drag that can be

obtained on a thin airfoil at low angle of attack and this cannot be obtained over the hole blade with thicker airfoils on the inner part of the blade. The curve for the double drag is therefore also shown for comparison.

Integrating the local power coefficient from the root of the blade we get the accumulated CP as shown in Figure 3-20 for two tip speed ratios. The results are summarized in Table 3-1 and the overall tendency with increasing tip losses for decreasing tip speed ratio and the opposite tendency for the influence of minimum drag is clear. To summarize, it seems that a realistic maximum of the power coefficient for a rotor seems to be in the range og 0.51-0.52.

Table 3-1 *Summary of the influence of tip loss and minimum blade drag coefficient for two tip speed ratios. Constant loading with CT=0.95.*

λ	CP	with tip loss	CD_{min} **0.007**	CD_{min} **0.014**
6	0.581	0.537	0.512	0.488
8	0.582	0.550	0.517	0.484

3.7 Influence of spinner – AD simulations

The influence on the rotor aerodynamics of a spinner with a radius 10% of the rotor radius, has been investigated using AD simulations for specified loadings and results will be presented in the present section. In the next section further results of using a spinner on a specific rotor design will be presented.

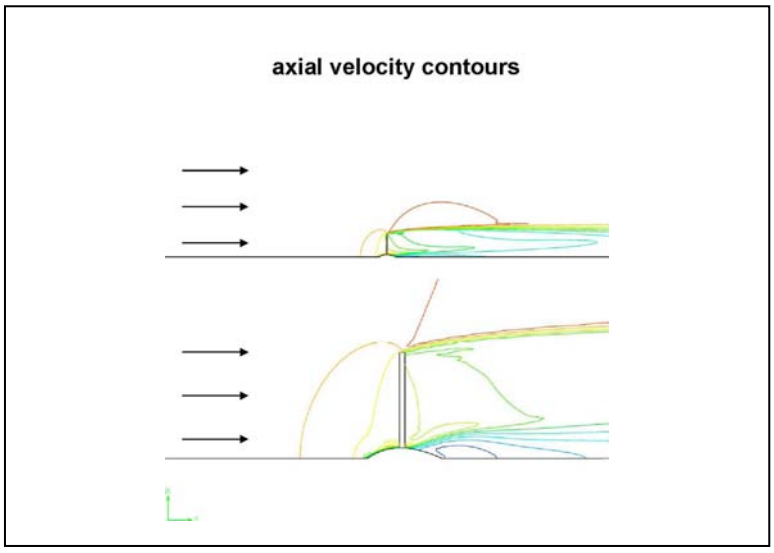

Figure 3-21 *Axial velocity contours computed on a rotor with a spinner 10% of rotor radius and with constant loading. At high loading (lower picture) the flow separates on the spinner.*

A spinner seems not to improve the power coefficient

The axial velocity contours for a rotor with a spinner 10% of rotor radius are shown in Figure 3-21. At high loadings (CT in the range above 0.8 - 0.9) a separation buble occurs on the backward side of the spinner due to the pressure rise here. It should be noted that the spinner is not rotating which will influence the flow separation.

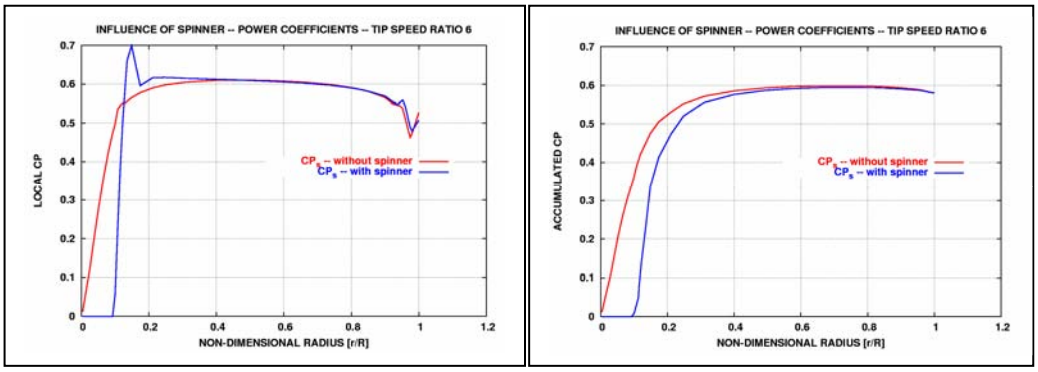

Figure 3-22 Comparison of local CP and accumulated CP for a rotor with and without a spinner. Constant loading and CT=0.95.

Due to the speed up effect from the spinner, the local CP is high just outside the spinner surface and reaches a value around 0.7, left graph in Figure 3-22. However, the integrated CP for the whole rotor is almost the same for a rotor with and without a spinner, right graph in Figure 3-22.

3.8 Results from analysis of a specific rotor design

To further investigate the above mentioned issues a specific rotor was designed where chord and twist distributions were increased towards the centre and compared to the original blade design. Additionally, the effect of the aerodynamically shaped spinner is investigated. The surface mesh topology on the rotor geometry with spinner, used in the CFD computations, is shown in Figure 3-23.

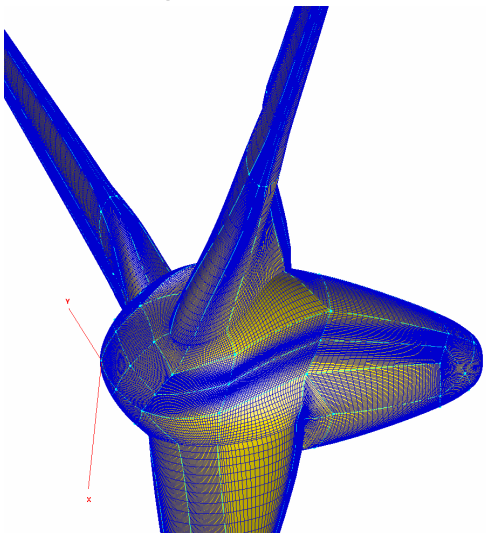

Figure 3-23: Surface mesh topology on the rotor with spinner used in the CFD computations.

Computations were performed using three different aerodynamic models. I.e. a standard BEM model, an actuator disc model and a fully 3D CFD code, EllipSys3D. The work has been published in ref. [12] and for further information the reader is referred to this. Three wind speeds are investigated: W = 8, 10 and 12 m/s and pitch and RPM are kept

constant. Results are presented as global power and thrust coefficients, CP and CT, shown in the following two tables.

Table 3-2: Mechanical power coefficient CP computed using BEM, Actuator Disc and EllipSys3D. % increase is shown in ( ).

Wind speed	Original blade	New design w.o. spinner	New design w. spinner
BEM			
8 m/s	0.507	0.512 (+1.0 %)	n.a.
10 m/s	0.472	0.478 (+1.3 %)	n.a.
12 m/s	0.409	0.416 (+1.7 %)	n.a.
Actuator Disc			
8 m/s	0.507	0.509 (+0.4 %)	0.509 (+0.4 %)
10 m/s	0.477	0.481 (+0.8 %)	0.482 (+1.0 %)
12 m/s	0.411	0.417 (+1.5 %)	0.418 (+1.7 %)
EllipSys3D			
8 m/s	0.501	0.506 (+1.0 %)	0.501 (+0.0 %)
10 m/s	0.475	0.480 (+1.0 %)	0.482 (+1.5 %)
12 m/s	0.400	0.414 (+3.5 %)	0.411 (+2.8 %)

A maximum CP of around 0.51 was obtained for a design with a high loading on the inboard part of the blade

Table 3-3: Thrust coefficient CT computed using BEM, Actuator Disc and EllipSys3D. % increase is shown in ( ).

Wind speed	Original blade	New design w.o. spinner	New design w. spinner
BEM			
8 m/s	0.844	0.853 (+1.1 %)	n.a.
10 m/s	0.692	0.702 (+1.4 %)	n.a.
12 m/s	0.574	0.583 (+1.6 %)	n.a.
Actuator Disc			
8 m/s	0.847	0.855 (+0.9 %)	0.853 (+0.7 %)
10 m/s	0.698	0.708 (+1.4 %)	0.706 (+1.1 %)
12 m/s	0.576	0.586 (+1.7 %)	0.582 (+1.0 %)
EllipSys3D			
8 m/s	0.842	0.850 (+1.0 %)	0.850 (+1.0 %)
10 m/s	0.693	0.704 (+1.6 %)	0.711 (+2.6 %)
12 m/s	0.556	0.576 (+3.6 %)	0.576 (+3.6 %)

Because the difference is quite small, CP and CT are given with three digits even though the uncertainty is not that small.

In general, all three aerodynamic models predict an increase in CP and CT for the new design without spinner with 12 m/s giving the largest relative increase. The new design with spinner also show a small increase but not as large as without spinner.

Figure 3-24 shows the local CP (left) and CT (right) as function of rotor radius for the new design at wind speed, W = 8 m/s for all three aerodynamic models. Two primary observations are made. The results using the actuator disc gives a large increase at r/R around 0.2 indicating that the actuator disc model takes into account the decrease in pressure in the wake near the centre leading to an increase swirl leading to increase local CP and CT. This is not captured by the BEM model. The CFD results also show a local increase but it is more smeared out over the blade span. Secondly, the CFD results show a lower CP and CT at the tip indicating lower loads due to the tip vortex. So even though

there is quite a difference in the spanwise distributions the global CP and CT are in good agreement. This could indicate that both tip correction and a root correction (as shown above) has to be proper implemented to get the right spanwise distributions.

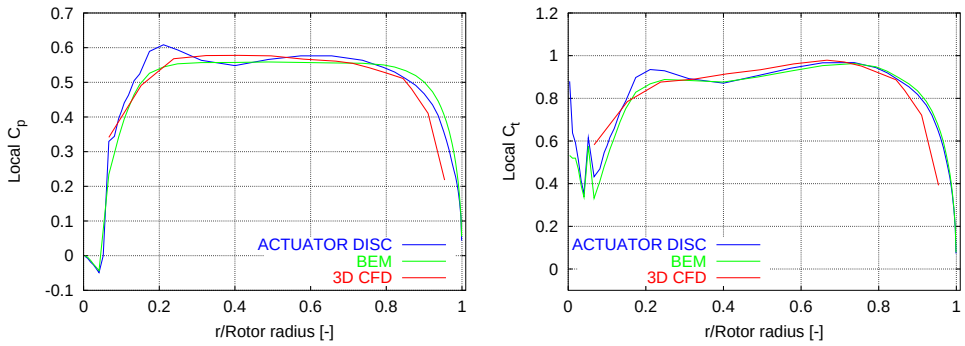

Figure 3-24: local CP (left) and CT (right) as function of rotor radius for the new design, W = 8 m/s.

3.9 Summary

A thorough investigation of the rotor aerodynamics with particular focus on the inboard part of the blade has been carried out comprising analytical work as well as numerical investigations with three model types; 1) the BEM model; 2) the actuator disc model and a full 3D CFD model. The main findings:

- The pressure term from wake rotation increases the axial flow velocity and thus also the local CP on the inboard part of the blade.
- Analytical derivations show that the positive effect on CP from pressure from wake rotation counteracts completely the increased losses from wake rotation as modeled in the common Glauert version of the BEM model.
- An analytical derivation shows that in order to obtain constant induction the thrust coefficient has to be increased considerably on the inboard part of the blade.
- A simple correction of the Glauert BEM model to account for the effect from the pressure term from wake rotation has been developed and tested.
- However, increased induction in the tip region computed with the actuator disc models is not seen in the BEM model. The origin of this increased induction is thought to be due to wake expansion.
- The AD simulations show that the Betz limit for CP locally can be exceeded but not the integrated CP over the hole rotor disc. A maximum CP of 0.586 at a tip speed ratio of 8 has been obtained.
- Including tip losses and the minimum blade drag coefficient a maximum rotor CP in the range of 0.51-0.52 has been obtained.
- Full 3D CFD simulations on different rotor designs resulted in a maximum CP of 0.51.

3.10 References

[1] Johansen, J. , Madsen, H.A., Sørensen, N.N., and Bak, C., ” Numerical Investigation of a Wind Turbine Rotor with an aerodynamically redesigned hub-region”. Proceedings of EWEC 2006.

[2] Madsen, H.A et al. ”Inboard Rotor/Blade Aerodynamics and its Influence on Blade Design”. Paper to be published in the Journal of Wind Energy.

[3] Madsen, H.A. et al. ”Inboard Rotor/Blade Aerodynamics and its Influence on Blade Design”. Fact sheet AEDXX. To be published

[4] Fuglsang, P.. “HAWTOPT User Manual Version 1.0a”. Risø-I-1817(EN), Risø National Laboratory, Roskilde, Denmark, January 2002

[5] ”Considerably Higher Yields – Revolutionary Rotor Blade Design”WindBlatt 3/2004, Enercon

[6] de Vries, O. “Fluid Dynamic aspects of Wind energy Conversion”. AGARD Advisory Group for Aerospace Research & Development”. AGARD-AG-243. July 1979

[7] Glauert, H. “Airplane Propellors”. Volume IV in Aerodynamic Theory edited by William Fredrick Durand. The Dover edition 1963.

[8] Øye S. A simple vortex model. In Proc. of the third IEA Symposium on the Aerodynamics of Wind Turbines, ETSU, Harwell, 1990, p. 4.1-5.15.

[9] Michelsen JA “Basis3D - a Platform for Development of Multiblock PDE Solvers.”, Technical Report AFM 92-05, Technical University of Denmark, 1992.

[10] Michelsen JA “Block structured Multigrid solution of 2D and 3D elliptic PDE's.” Technical Report AFM 94-06, Technical University of Denmark, 1994.

[11] Sørensen NN “General Purpose Flow Solver Applied to Flow over Hills.” Risø-R-827-(EN), Risø National Laboratory, Roskilde, Denmark, June 1995.

[12] J. Johansen, H.Aa Madsen, N.N. Sørensen and C. Bak, “Numerical Investigation of a Wind Turbine Rotor with an aerodynamically redesigned hub-region”, EWEC-2006, Athens, 27. feb. -2. March, 2006.

4 New Airfoil Family Considering Structural Stiffness and Compatibility

Christian Bak, Peter B. Andersen, Mac Gaunaa

This chapter presents the design of a new airfoil family for MW-size wind turbines with variable speed and pitch control. Five airfoils were designed with thickness-to-chord ratios between 15% and 30% to cover most of the span of a wind turbine blade. The airfoils were designed to have high maximum lift coefficient to allow a slender blade, while maintaining high aerodynamic efficiency. Given those characteristics the airfoils were designed with maximum stiffness and compatibility between the airfoils. Finally, the airfoils were designed to be roughness insensitive. The design was carried out with a Risø inhouse multi disciplinary optimization tool which was extended to 3D so that the complete blade shape and the rotor flow were taken into account.

A new airfoil family with high maximum lift considering structural stiffness and compatibility using a 3D design tool is described

4.1 Nomenclature

a	Axial velocity induction factor [-]
a'	Tangential velocity induction factor [-]
A	Weibull parameter [m/s]
AOA	Angle of attack [°]
AOA_0	Angle of attack at c_l=0[°]
AOA_r	Angle of attack relative to AOA_0 [°]
c	Airfoil chord [m]
C	Weibull parameter [-]
c_d	Drag coefficient [-]
c_l	Lift coefficient [-]
$c_{l,max}$	Maximum lift coefficient [-]
c_l-c_d-$ratio$	The ratio: c_l/c_d [-]
C_p	Pressure coefficient [-]
CP	Rotor power coefficient [-]
D	Drag force [N]
F	Resulting force on airfoil [N]
L	Lift force [N]
N	Airfoil force normal to the rotor plane [N]
r	Radius [m]
Re	Reynolds number [-]
T	Airfoil force in the rotor plane [N]
t/c	Thickness-to-chord ratio [%]
V_a	Axial flow speed in rotor plane [m/s]
V_0	Wind speed [m/s]
V_{rot}	Tangential flow speed in rotor plane [m/s]
x, y	Airfoil coordinates chordwise and perpendicular to chord, respectively
z_0	Roughness length [m]
Ω	Rotational speed [Rad/s]

4.2 Introduction

Design of tailored airfoils for rotor blades is important for the continuing development of wind turbines. It has been known for decades that wind turbine airfoils should differ from traditional aviation airfoils in choice of design point, off-design characteristics and structural properties. The development of wind turbine airfoils has been ongoing since the mid 1980's. Significant efforts have been made by Tangler and Somers (NREL)[1], Timmer and Van Rooy (DELFT)[2] and Björk (FFA)[3]. Other wind turbine airfoil developments can be found in [4], [5] and [6]. The development of the Risø airfoils was initiated in the mid 1990's and until now three airfoil families have been developed, Risø-A1, Risø-P and Risø-B1 [7]. Numerous two-dimensional wind tunnel tests have been carried out in the VELUX wind tunnel and field-testing has been carried out for wind turbine rotors from 600kW to 3MW.

The new airfoil family was designed for MW-size wind turbines with variable speed and pitch control and many characteristics from the Risø-B1 airfoil family were inherited because this airfoil family has shown to be both efficient and to have a high degree of insensitivity to leading edge roughness. However, evaluating the Risø-B1 family has also shown the need for maximizing the stiffness around the chord axis, i.e. the flap direction. Furthermore, the new airfoil family was designed to have a high degree of compatibility.

The new airfoil family has inherited many characteristics from the Risø-B1 family but has higher structural stiffness, compatibility and higher aerodynamic performance

Key design objectives for the new airfoil family were twofold: (1) To maximize the lift-drag ratio and (2) To have a high $c_{l,max}$. Insensitivity of maximum lift to leading edge roughness was ensured by two additional design objectives: (1) Having suction side transition from laminar to turbulent flow in the leading edge region for angles of attack close to but below $c_{l,max}$ and (2) Obtaining a high $c_{l,max}$ with simulated leading edge roughness. Additional design objectives ensured good structural and aerodynamic compatibility between the different airfoil sections and good structural properties for inboard airfoils.

The design was carried out with a Risø in-house multi disciplinary optimization tool that has been developed since 1996 [8], which was extended to include a complete blade with its structural surface characteristics and rotor aerodynamics. The numerical optimization algorithm works directly on the airfoil shape providing a direct and interdisciplinary design procedure, where multiple design objectives for aerodynamics and structure may be handled simultaneously.

This chapter describes the extension of the airfoil design tool and the development of a new airfoil family.

4.3 The airfoil design tool

The airfoil design tool can be divided into a 2D design tool and a 3D design tool. The 2D design tool has been used to design the former Risø airfoil families. It uses a direct method where numerical optimization is coupled with both the flow solver *XFOIL* [9], which is a panel code with inviscid/viscous interaction, and the flow solver *EllipSys2D*, which is a code based on the solution of the Navier Stokes equations in 2D [10], [11], [12]. A number of design variables form the airfoil shape, which is optimized subject to design objectives and constraints. Direct methods, such as the method used, are basically interdisciplinary and multi-point and they allow direct use of integrated response parameters such as airfoil c_l and c_d directly as design objectives. Also, boundary layer response parameters, e.g., skin friction and transition point location can be constrained or

used as objectives. Structural characteristics can be controlled by constraining the shape in terms of coordinates, gradients and curvatures.
The 3D tool is developed in this work and models a complete blade with all its airfoil sections to form the blade surface and compute the aerodynamic performance of the rotor. Gradients and curvatures in the direction from the root to the tip were included to quantify the compatibility. Also, the 3D tool opens up the possibility of maximizing the rotor power performance in terms of, e.g. the power coefficient *CP*. With the 3D tool follows a graphical user interface so that information about the geometry can either be extracted for use in the optimization process or existing blades can be inspected visually and quantitatively.

Design algorithm

The design variables are changed in an optimization problem to minimize the objective function. This is done subject to constraints. In this case the design variables are the control points that describe the airfoil shape. The constraints are side values for the design variables and bounds on response parameters from flow and structural calculations. A traditional Simplex optimizer was used with a finite difference sensitivity analysis. This is a simple and robust solution method, which however, is computationally expensive because of the large number of necessary flow calculations. The optimization process is iterative involving numerous calculations of flow and structural response parameters where the design gradually changes to improve the objective. The calculated flow and structural response parameters are used to estimate the value of the objective function and the constraints. Multiple angles of attack are calculated to allow offdesign optimizations. The combination of flow and structural responses allows multidisciplinary optimization (MDO).

Geometric description

A smooth shape is important for the optimization results. The 2D airfoil shape was represented by a single B-spline defined from the trailing edge around the airfoil contour by a set of control points. The blade shape was represented by cubic B-splines fixed at the top and bottom of the 2D sections and at the leading and trailing edge. In between these four fix points at the sections the splines are distributed evenly along the surface length. Creation of the blade is seen in the screen dump, Figure 4-1.

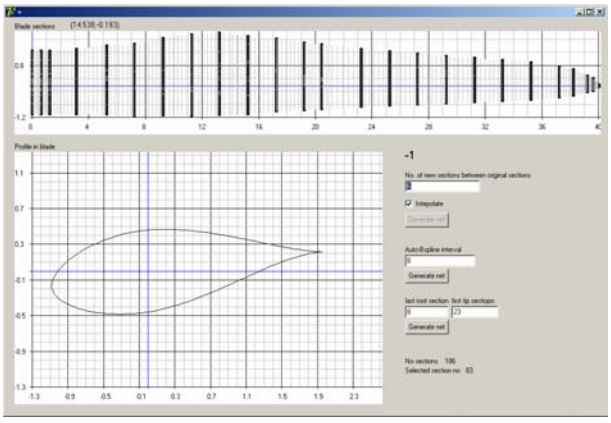

The design tool AIRFOIL-OPT is extended with a 3D tool

Figure 4-1 Screen dump from the 3D tool showing the blade planform at the top with a number of corresponding master airfoil sections with thick lines. In between the master airfoil sections are seen thin, grey lines showing the interpolated airfoil sections from the connecting curves from the root to the tip and forming the mesh. At the bottom of the screen dump is seen a 2D airfoil section in the blade.

The splines creating the 2D sections and the connection between the 2D sections form a mesh from where coordinates, gradients and curvatures can be extracted and used either for inspection or for use in the optimization process, see Figure 4-2.

From the 3D tool the quality of the blade surface can be investigated

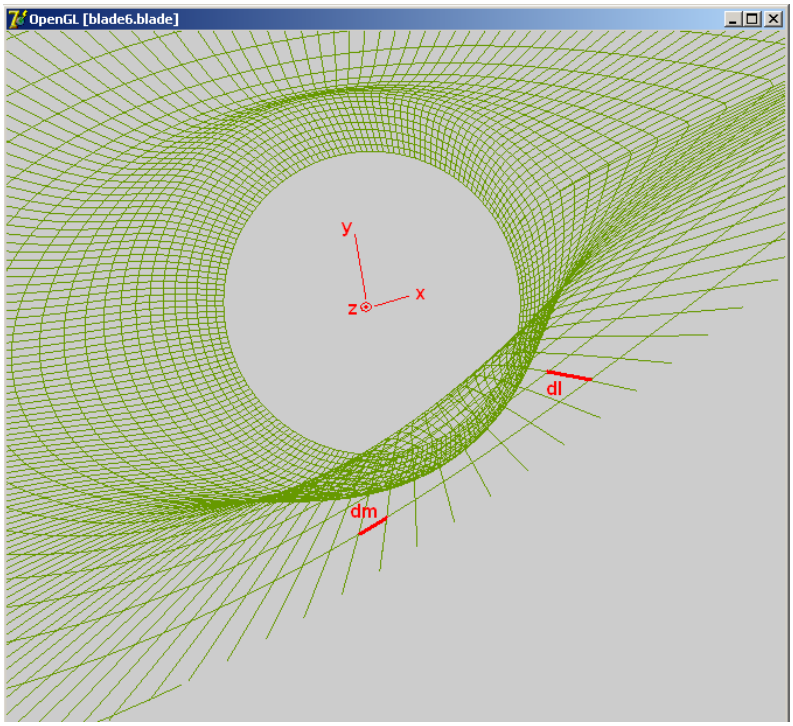

Figure 4-2 Part of a mesh creating the 3D blade shape and from where gradients, curvatures etc. can be extracted.

Flow analysis

The *XFOIL* code by Drela was used for the flow calculations during the optimization [13]. For a given *AOA* and *Re*, *XFOIL* provides the C_p-distribution and c_l, and c_d. In addition, numerous boundary layer parameters are calculated. Transition was modeled by the e^n method with n = 9. Prescribing transition to 0.1% after the leading edge on the suction side and at the trailing edge on the pressure side simulated leading edge roughness. *XFOIL* is well suited for optimization because of the fast and robust viscid/inviscid interaction scheme. However, the integral boundary layer formulation is not well suited for separated flows. *XFOIL* should be used with caution at $c_{l,max}$. Others find that it may be necessary to modify or even tune *XFOIL* to better match measured results [2]. The *EllipSys2D* CFD code was therefore used on the optimization results to verify the magnitude of $c_{l,max}$ and the shape of c_l in the post stall region. The *EllipSys* code is developed in co-operation between the Department of Mechanical Engineering at DTU and the Department of Wind Energy at Risø National Laboratory, see [10], [11] and [12]. It is a multi-block finite volume discretization of the incompressible Reynolds Averaged Navier-Stokes (RANS) equations in general curvilinear coordinates. The k-ω SST turbulence model by Menter was used for turbulent flow calculations [14]. *EllipSys* is highly validated for both 2D airfoil flow and 3D wind turbine rotor flow [15], [16].

4.4 Design strategy

The desirable airfoil characteristics form a complex matrix of properties of which some are in conflict with others. This has been a topic of discussion in the literature, e.g., in [17], [18] and [19]. There seems to be consensus on most of the general desirable

characteristics. However, the means of achieving them are strongly related to the design method and the philosophy of the designer. The new airfoils were designed for operation on a wind turbine rotor. Figure 4-3 shows an airfoil section corresponding to a wind turbine blade element. The force that contributes to the rotor power is the tangential force, *T*, whereas the force that contributes to the rotor thrust, is the normal force, *N*. Also, lift and drag, *L* and *D*, respectively, are shown because these values are common measures for airfoils describing the force orthogonal and parallel to the velocity, V_{rel}. As it was the case with Risø-B1 airfoil family *T* can be used as the objective function, but also the lift-drag ratio (*L/D*) can be used. The latter is a common measure of the airfoil efficiency because *L* can be considered as the production and *D* can be considered as the loss. The new airfoil family was designed maximizing the c_l-c_d ratio.

Maximizing the lift-drag ratio is a key design objective

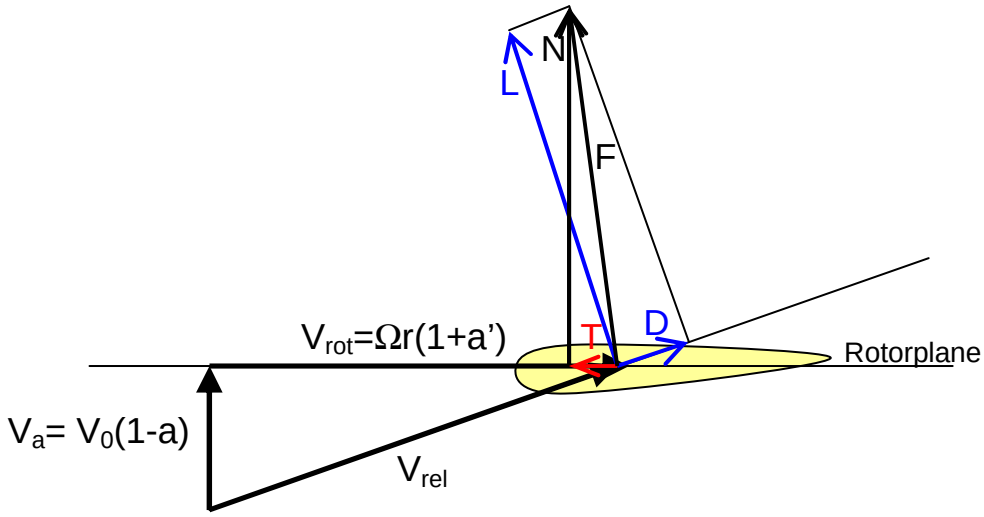

Figure 4-3 Forces on an airfoil section for a wind turbine rotor.

Structure

A wind turbine blade may be divided into the root, mid and tip parts. The mid and tip parts are determined mainly from aerodynamic requirements whereas structural objectives are relevant mainly for the inboard part of the blade, e.g., for *t/c* > 24%. The *t/c* ratio is the most important parameter and also important are the location of the maximum thickness on the chord and the local shape of the airfoil.

Another issue is the geometric compatibility between airfoils of the same family to ensure smooth transition from one airfoil to the other. Geometric compatibility was ensured by using the new 3D tool, where two airfoils with *t/c*=15% and 24%, respectively, designed with the 2D tool, formed the basis for the remaining airfoil sections, 18%, 21% and 30%, by interpolating and even extrapolating between the two airfoils. These interpolated and extrapolated airfoils were slightly adjusted to maximize the aerodynamically and structurally performance. Because of the desire for high $c_{l,max}$ significant undercamber was allowed on the pressure side. The thickness of the trailing edge was kept finite but thin to minimize trailing edge noise.

Insensitivity of $c_{l,max}$ to leading edge roughness

Insensitivity to roughness in the airfoil leading edge region formed by accumulation of dust, dirt and bugs is well recognized as a main design driver for wind turbine airfoils [20]. The new airfoils were designed for minimum sensitivity of $c_{l,max}$ to leading edge roughness by two separate design objectives: (1) The suction side natural transition point

was constrained to move to the very leading edge for AOA around 3° below $c_{l,max}$ predicted with forced transition. This determined the local shape of the leading edge region so that a small pressure rise at the leading edge caused natural transition to turbulent flow at the leading edge a few degrees before $c_{l,max}$. Premature transition caused by roughness will therefore be eliminated by a very forward position of the natural transition point. (2) The level of $c_{l,max}$ resulting from a flow analysis with simulation of leading edge roughness, i.e. forced transition, was constrained to a sufficiently high value compared to results from analysis with smooth flow. This shapes the airfoil suction side so that the pressure recovery region does not separate prematurely because of an increase of the boundary layer thickness caused by roughness, which would reduce $c_{l,max}$. Even with this constraint massive roughness will inevitably reduce $c_{l,max}$.

Many constraints were put on the airfoil in the design process

Design $c_{l,max}$

The airfoil sections were designed for high $c_{l,max}$. This was chosen because the airfoil sections can be used for design of slender blades and in general ensuring minimum fatigue loads and extreme loads. However, a disadvantage from this choice is the loss of stiffness for the blade if the relative airfoil thicknesses are maintained even though the chord distribution is reduced. Thus, the choice of high maximum lift is closely related to the choice of concept in the blade design. No matter which concept is used in the blade design, the inner part of the rotor needs airfoil sections with high maximum lift.

Design objective

A compound objective function was defined as a weighted sum of c_l-c_d-ratio values resulting from multiple angles of attack in the design *AOA*-range. Some were for smooth flow whereas others were for flow with simulated leading edge roughness to ensure good performance at both conditions. The airfoil design *AOA*-region is also determined from the requirements to the wind turbine off-design operation. Because of the stochastic nature of the wind, turbulence gusts and wind direction changes will always lead to some off-design operation due to non uniform inflow. However, the degree of offdesign is mainly given by the power control principle [21]. In most cases it is desirable that the design *AOA*-region is close to $c_{l,max}$ since this enables low rotor solidity and/or low rotor speed. For all the new airfoils the design point region was $AOA_r \in [9^o; 14^o]$. This should lead to an expected high $c_{l,max}$ at around $AOA_r = 16^o$ corresponding to $c_{l,max} \doteq 1.8$ at a lift curve slope of 2π/rad. The airfoil family was designed for $Re=6\text{x}10^6$, because this corresponds to the largest designs.

4.5 The new airfoil family

The evaluation of the new airfoil family will be divided into an evaluation of the 2D characteristics and the 3D characteristics. In the evaluation the new airfoil family will be compared to the Risø-B1 airfoil family.

2D evaluation

In the following c_l vs. c_d and c_l vs. *AOA* are shown for the five new airfoils. The characteristics were computed using *EllipSys2D* and assuming forced transition from the very leading edge (solid lines) and free transition from laminar to turbulent flow (dots). Earlier investigations have shown that *EllipSys2D* predicts the performance of the Risø-B1 airfoil family well [7] at $Re=1.6\text{x}10^6$. Therefore, it is believed that the predicted performance of the new airfoil family is trustworthy.

Figure 4-4 shows the characteristics for the 15% airfoil. Compared to the Risø-B1 airfoil the c_l-c_d ratio with forced transition is similar up to c_l=1.7. However, the maximum lift for the new airfoil is not as high as for the Risø-B1 airfoil. The c_l-c_d-ratio assuming free transition is significantly higher between c_l=1.2 and 1.6, which increases the possibility for increased performance if the airfoil is not exposed to leading edge roughness.

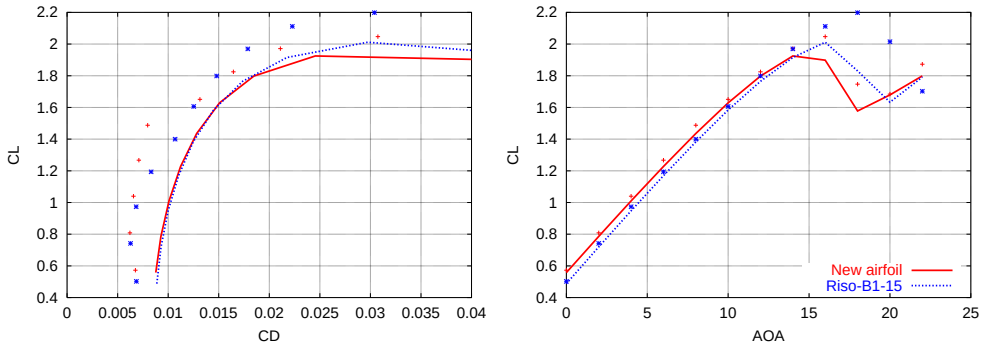

Figure 4-4 Aerodynamic characteristics for the t/c=15% section. Left: Lift coefficient vs. drag coefficient. Right: Lift Coefficient vs. α. Solid lines: Forced transition from the leading edge. Dots:Free transition from laminar to turbulent flow. Re=6x10^6.

Figure 4-5 shows the aerodynamic characteristics for the new 18% airfoil. The performance is similar to the 15% airfoil with nearly the same maximum lift and with high c_l-c_d-ratio when assuming both forced and free transition. Compared to the Risø-B1-18 airfoil the new airfoil is very similar concerning maximum lift and c_l-c_d-ratio with forced transition. However, the performance with free transition is improved.

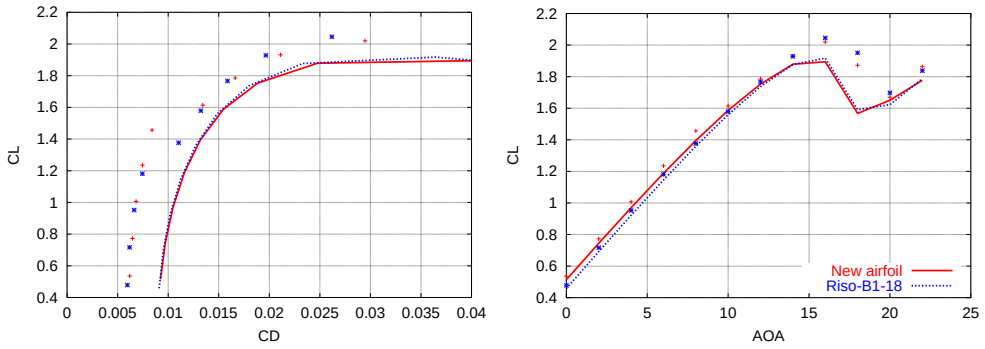

Figure 4-5 Aerodynamic characteristics for the t/c=18% section. Left: Lift coefficient vs. drag coefficient. Right: Lift Coefficient vs. α. Solid lines: Forced transition from the leading edge. Dots:Free transition from laminar to turbulent flow. Re=6x10^6.

The aerodynamic characteristics for the new 21% airfoil is shown in Figure 4-6. The performance is similar to the 18% airfoil with a slight reduction in $c_{l,max}$ and with high c_l-c_d-ratio when assuming both forced and free transition. Compared to the Risø-B1-21 airfoil the new airfoil is very similar concerning maximum lift and c_l-c_d-ratio with forced transition. However, the performance with free transition is somewhat improved between c_l=1.2 and 1.5.

The aerodynamic characteristics of the 15% to 24% thick airfoils in the new airfoil family are very similar to the Risø-B1 airfoil family, but is more efficient

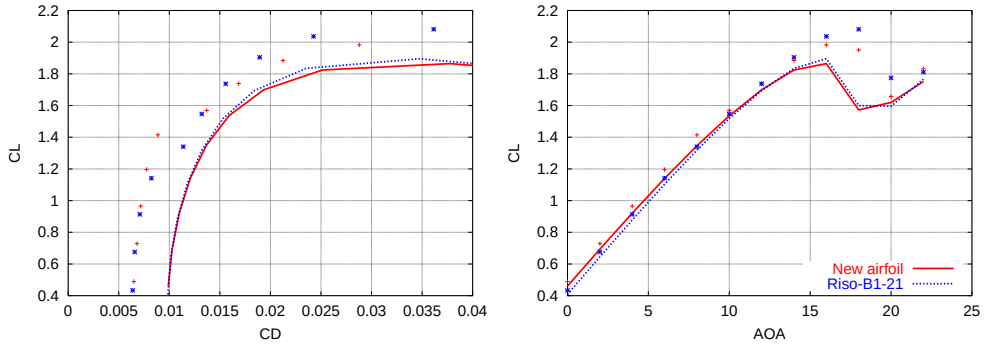

Figure 4-6 Aerodynamic characteristics for the t/c=21% section. Left: Lift coefficient vs. drag coefficient. Right: Lift Coefficient vs. α. Solid lines: Forced transition from the leading edge. Dots:Free transition from laminar to turbulent flow. Re=6x10^6.

Figure 4-7 shows the aerodynamic characteristics for the new 24% airfoil. The performance is similar to the 21% airfoil with yet a slight reduction in $c_{l,max}$ and with high c_l-c_d-ratio when assuming both forced and free transition. Compared to the Risø-B1-24 airfoil the new airfoil is very similar concerning maximum lift and c_l-c_d-ratio with forced transition. However, the performance with free transition is improved for c_l values between 1.0 and 1.4.

The aerodynamic characteristics for the new 30% airfoil is shown in Figure 4-8. Unlike the other airfoil thicknesses this airfoil is not similar to the Risø-B1-30 airfoil. It was not possible to retain the same excellent aerodynamic characteristics, when increasing the requirements for the structural stiffness. However, high $c_{l,max}$ and fair c_l-c_d-ratio like the FFA-W3-301 airfoil was obtained. Thus, requirements to the structure had a price at this airfoil thickness.

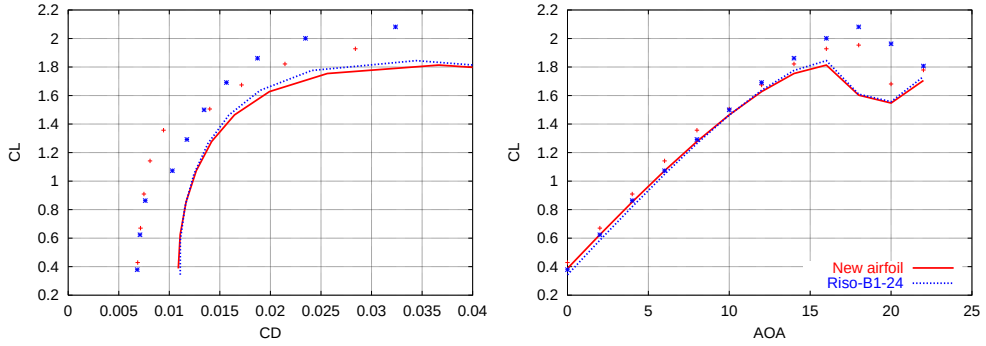

Figure 4-7 Aerodynamic characteristics for the t/c=24% section. Left: Lift coefficient vs. drag coefficient. Right: Lift Coefficient vs. α. Solid lines: Forced transition from the leading edge. Dots:Free transition from laminar to turbulent flow. Re=6x10^6.

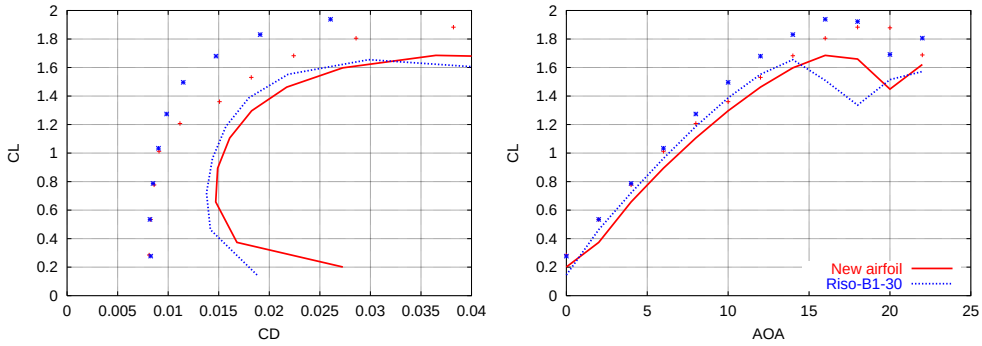

Figure 4-8 Aerodynamic characteristics for the t/c=30% section. Left: Lift coefficient vs. drag coefficient. Right: Lift Coefficient vs. α. Solid lines: Forced transition from the leading edge. Dots:Free transition from laminar to turbulent flow. Re=6x10^6.

The aerodynamic characteristics of the 30% thick airfoil in the new airfoil family differ from the Risø-B1-30 airfoil and has higher structural performance but reduced aerodynamic performance

Figure 4-9 shows the moment of inertia vs. *t/c* in the direction orthogonal to the chord direction, with a wall thickness of 0.01c except from positions between *x/c*=0.15 to 0.55, where it was 0.02*c*. Compared to the Risø-B1 family the new 15% airfoil showed only 2% increase in stiffness. However, airfoil thicknesses from 18% to 30% showed an increase in stiffness around 5% compared to the Risø-B1 family. Also, the moment of inertia of the commonly used airfoil combination NACA 63-6xx/FFA-W3-xxx is shown. These airfoils are significantly stiffer, but they do not show the same aerodynamically characteristics in terms of high $c_{l,max}$ and c_l-c_d-ratio. Therefore, they are not directly comparable, because they are not applicable to the design of low solidity rotors, but they are shown as a reference to well-known airfoils.

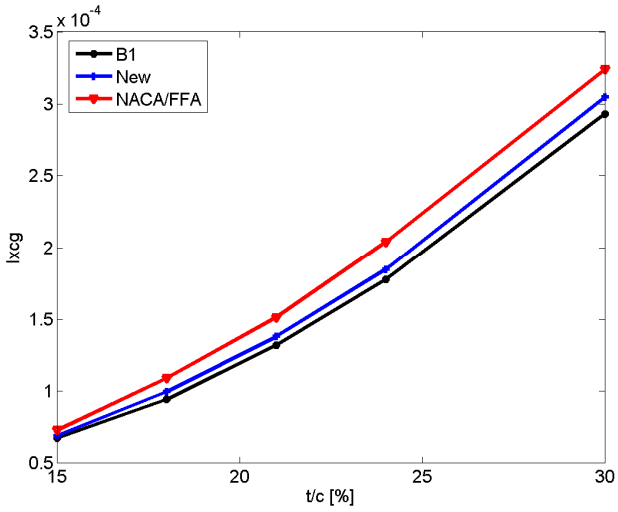

The new airfoil family is around 5% more stiff

Figure 4-9 Structural characteristics for the new airfoil family: Moment of inertia vs. relative airfoil thickness.

3D evaluation

Based on a blade equipped with Risø-B1 airfoils and designed to a tip speed ratio of 8.0, the two airfoil series were compared. Using the new airfoil series the blade planform was reused, however with an adjustment of the twist distribution. Figure 4-10 shows the power efficiency coefficients, *CP*, for a Pitch Regulated Variable Speed wind turbine with airfoil flow with forced transition simulating leading edge roughness (solid lines) and free transition simulating clean leading edge (dashed lines). It is seen that the performance for the two rotors with different airfoil families is very similar when

assuming forced transition on the airfoils, while 1% increase in *CP* is observed when using the new airfoils and assuming free transition on the airfoils. Thus, with a wind climate with roughness length z_0=0.025m, Weibull parameter *A*=9.03m/s and Weibull parameter *C*=2.0 the energy production with the new airfoil family is decreased with 0.05% assuming forced transition caused by a loss at wind speeds 11 and 12m/s and increased with 0.4% assuming free transition.

The new airfoil family equipped on a rotor performs similar to the Risø-B1 in turbulent flow conditions, but performs 1% better in smooth flow

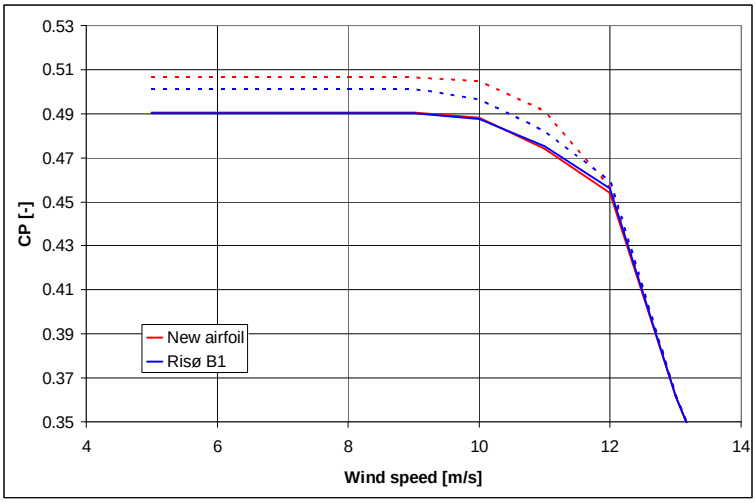

Figure 4-10 Aerodynamically characteristics for a rotor equipped with the new airfoil family and the Risø-B1 family. Solid lines show the rotor performance assuming forced transition on the airfoil suction side. Dashed lines show the rotor performance assuming free transition from laminar to turbulent flow on the airfoil suction side.

The stiffness of the blade was evaluated by predicting the tip deflection. For this evaluation the blade was equipped with three different airfoil series: the new airfoils, the Risø-B1 airfoils and the NACA 63-6xx/FFA-W3-xxx airfoils using the NACA series up to *t/c*=21% and FFA series from *t/c*=24%. The planform of the blade was identical in the three cases. Also, the blade was loaded the same way for all cases corresponding to the loading for the blade equipped with Risø-B1 airfoils. The deflections of those blades are reflected in Figure 4-11. The plot shows that a blade equipped with the new airfoils obtains a reduction of the tip deflection of 5% compared to the Risø-B1 family. Compared to the blade with NACA/FFA airfoils the tip deflection is 10% bigger. However, it should be noted that the new airfoils and the NACA/FFA airfoils should be used for rotors based on rather different concepts because the new airfoils should be used for low solidity rotors in contrast to the NACA/FFA airfoils.

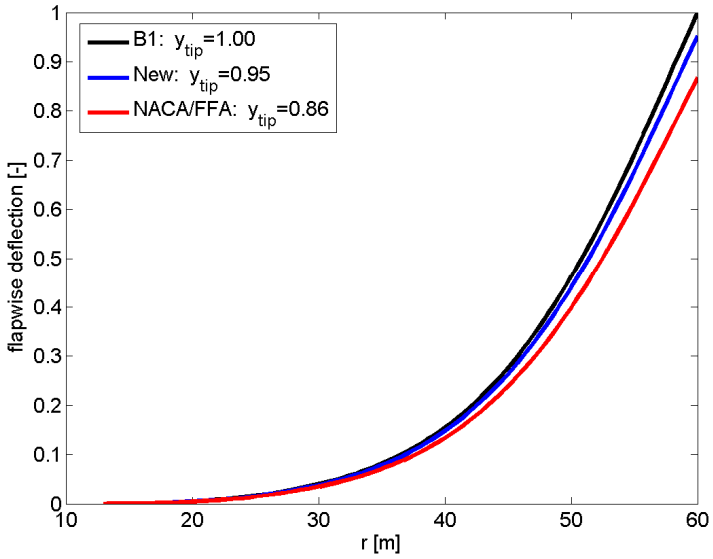

A blade equipped with the new airfoil family is 5% more stiff than a blade with Risø-B1 airfoil family

Figure 4-11 Structural characteristics for the new airfoil family: The stiffness of the airfoil families expressed in terms of deflection, where the blade with the Risø-B1 family is the reference.

The new 3D tool was used to extract several different gradients, curvatures and surface angles, such that the compatibility between the different airfoil thicknesses could be evaluated. Figure 4-12 shows a plot of the curvature of the curves connecting the 2D airfoil sections in the direction from the root towards the tip. Along the x-axis is seen the surface position starting at the trailing edge, moving along the pressure side via the leading edge up to the suction side, ending at the trailing edge. The numbers shown are the number of the curve connecting the 2D airfoil sections. Thus, the blade is resolved with 180 curves from the root towards the tip, where the trailing edge is positioned at number 1 and 180 and the leading edge is positioned at number 90. Along the y-axis is the radial position. The airfoil sections used in Figure 4-12 is NACA 63-615 to NACA 63-621 and FFA-W3-241 to FFA-W3-301. Around r=14m and 39m high values for the curvature are observed. This is due to the transition from the NACA to the FFA airfoils (r=39m) and the transition from FFA-W3-241 to FFA-W3-301 (r=14m). Figure 4-13 shows the same entities for the same blade but equipped with the new airfoil series. Here, no high values for the curvature are seen. However, medium values for the curvature at r=14m is observed. This is due to the fast changes in t/c because the inner third of the blade takes care of relative thickness changes from t/c=24% to 100%, which is a cylinder at the very root. This illustrates the high coupling between airfoil design and blade design.

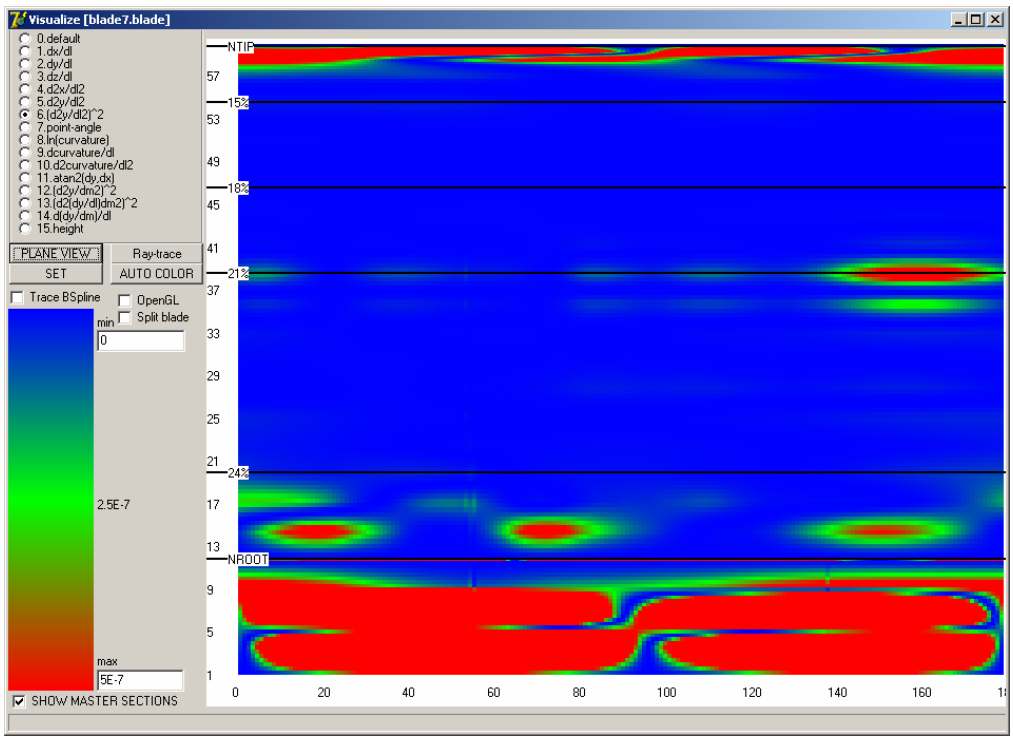

Figure 4-12 Spanwise curvature for a blade equipped with NACA/FFA airfoils: Compatibility visualized in terms of the curvature of curves following the blade surface from the root towards the tip.

The surface quality can be quantified using the new 3D tool

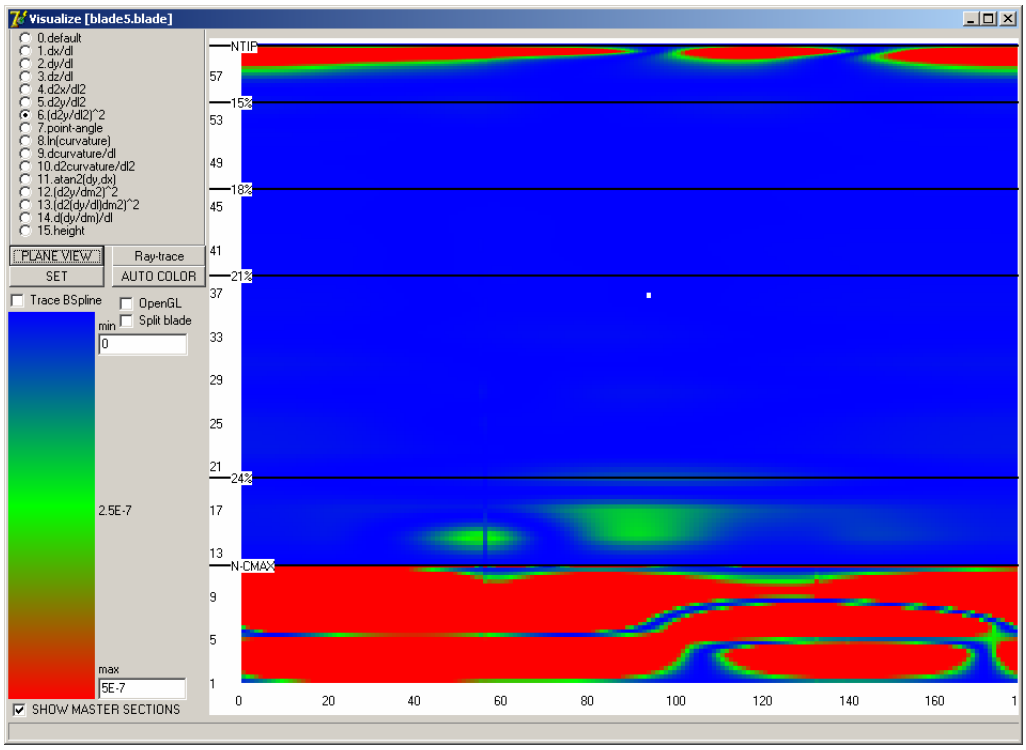

Figure 4-13 Spanwise curvature for a blade equipped with the new airfoil family: Compatibility visualized in terms of the curvature of curves following the blade surface from the root towards the tip.

4.6 Conclusions

This chapter presented results from the development of a new Risø airfoil family for wind turbines considering structural stiffness and compatibility in addition to excellent aerodynamics. For this purpose the airfoil design tool *AIRFOILOPT* was extended with a 3D description of the airfoils mounted on a blade and the possibility of computing gradients, curvatures and angles at the surface. The 3D extension can be used in the airfoil design process, but with the extensive graphical user interface it can as well be used to inspect existing blades and airfoils. Also, the extension of the design tool made it possible to compute the rotor flow in terms of the Blade Element Momentum theory.

Furthermore, a method of designing an airfoil family was developed. Two airfoils were designed without taking the 3D shape into account. They were positioned at the tip, t/c=15%, and close to the root, t/c=24%. Interpolation and extrapolation of these two airfoils made initial guesses for the remaining airfoil thicknesses. Based on these guesses the airfoils were adjusted both aerodynamically and structurally.

The airfoils were developed for variable speed operation and pitch control of large megawatt sized rotors. Design objectives were used with simultaneous use of airfoil flow assuming both free and forced transition. The main design objective was to maximize c_l-c_d ratio, contributing to the power efficiency of a wind turbine, over a range of design angles of attack along with numerous constraints on flow and structural response parameters to ensure a high maximum lift coefficient and insensitivity of this to leading edge roughness. An important feature of the new airfoils is the structural stiffness which is maximized and the high degree of compatibility subject to the high requirement to the aerodynamic characteristics.

4.7 References

[1] Tangler JL Somers DM. NREL Airfoil Families for HAWT's. *Proc. WINDPOWER'95, Washington D.C., 1995*; 117-123

[2] Timmer WA van Rooij RPJOM. Summary of the Delft University Wind Turbine Dedicated Airfoils. AIAA-2003-0352

[3] Björk A. Coordinates and Calculations for the FFAW1-xxx, FFA-W2-xxx and FFA-W3-.xxx Series of Airfoils for Horizontal Axis Wind Turbines. FFA TN 1990-15, Stockholm, Sweden 1990

[4] Hill, D.M., Garrad, A.D. (1988), "Design of Aerofoils for Wind Turbine Use", *Proc. IEA Symposium on Aerodynamics of Wind Turbines, Lyngby, Denmark*.

[5] Chaviaropoulos, P., Bouras, B., Leoutsakos, G., Papailiou, K.D. (1993), "Design of Optimized Profiles for Stall Regulated HAWTs Part 1: Design Concepts and Method Formulation", Wind engineering Vol. 17, 6 (1993) pp 275-287.

[6] Hoadley, D., Madsen, H.A., Bouras, B.(1993), "Aerofoil Section Design and Assessment", Final Rep. Contract JOUR 0079, The European Comisión DGXII

[7] *Fuglsang, P.; Bak, C.*, Development of the Risø wind turbine airfoils. *Wind Energy* (2004) **7** , 145-162

[8] Fuglsang P Dahl KS. Multipoint Optimization of Thick High Lift Airfoil Wind Turbines", *Proc. EWEC´97, Dublin, Ireland, 1997*, 468-471

[9] Drela M. *XFOIL*, An Analysis and Design system for Low Reynolds Number Airfoils. Low Reynolds Number Aerodynamics, Vol. 54 (1989) In Springer- Verlag Lec. Notes in Eng.

[10] Michelsen JA. Basis3D - a Platform for Development of Multiblock PDE Solvers. Technical Report AFM 92-05, Technical University of Denmark, 1992

[11] Michelsen JA. Block structured Multigrid solution of 2D and 3D elliptic PDE's. Technical Report AFM 94-06, Technical University of Denmark, 1994

[12] Sørensen NN. General Purpose Flow Solver Applied to Flow over Hills. Risø-R-827(EN), Risø National Laboratory, Denmark, June 1995

[13] Drela M. *XFOIL*, An Analysis and Design system for Low Reynolds Number Airfoils. Low Reynolds Number Aerodynamics, Vol. 54 (1989) In Springer- Verlag Lec. Notes in Eng.

[14] Menter FR. Zonal Two Equation k-ω Turbulence Models for Aerodynamic Flows. AIAA-932906

[15] Sørensen NN Michelsen JA Schreck S. Navier-Stokes Predictions of the NREL Phase VI Rotor in the NASA Ames 80 ft x 120 ft Wind Tunnel. J. Wind Energy 2002; 5:151-169.

[16] Bertagnolio, F.; Sørensen, N.N.; Johansen, J.; and Fuglsang, P., Wind Turbine Airfoil Catalogue, Risø-R-1280(EN), Risø National Laboratory, Roskilde, Denmark, August 2001.

[17] Tangler JL Somers DM. Status of the Special Purpose Airfoil Families. *Proc. WINDPOWER'87, San Fransisco,1987*

[18] Björk A. Airfoil design for variable rpm horizontal axis wind turbines. *Proc. EWEC'89, Glasgow, Scotland, 1989*

[19] Fuglsang P. Aerodynamic Design Guidelines For Wind Turbine Rotors. *Proc. 4th GRACM Congress on Computational Mechanics GRACM 2002, Patra, 27-29, June 2002*

[20] Tangler JL Somers DM. Status of the Special Purpose Airfoil Families. *Proc. WINDPOWER'87, San Fransisco,1987*

5 Profile Catalogue for Airfoil Sections Based on 3D Computations

Bertagnolio, F., Sørensen, N.N., and Johansen, J.

After the publication of the Wind Turbine Airfoil Catalogue [1] which presented two-dimensional computational results for a wide range of wind turbine airfoils, and compared these results with experimental data when available, it was surmised that some discrepancies might originate from the two-dimensional approximation. It was therefore suggested that an investigation of the three-dimensional effects on the prediction of airfoil characteristics using Navier-Stokes computations should be undertaken.

Study of the influence of 3D effects

The aim of this work is to evaluate the prediction capabilities of the computational code EllipSys3D compared to its two-dimensional version EllipSys2D on one side, and the experimental results (when available) on the other side. In order to perform this study, the flow around three-dimensional blade sections for chosen profiles will be computed. Several aspects of the numerical code are investigated. As it was clearly shown in the Wind Turbine Airfoil Catalogue [1], transition modelling is a decisive factor for airfoil characteristics prediction. Therefore, the influence of the implementation of (simplified) three-dimensional transition models will be investigated. In addition, turbulence modelling in the form of Reynolds-Averaged Navier-Stokes equations and of the Detached Eddy Simulation model, as well as their influence on characteristics prediction, are studied.

Due to the high computational cost of 3D Navier-Stokes calculations, the study concentrates on only 4 chosen profiles: RISØ-B1-18, NACA 63-430, S809, and DU 93-W-210. These were selected as their aerodynamic behaviors are quite different from each other, and therefore they are assumed to be representative for a wide range of turbine airfoils.

5.1 Description of the Navier-Stokes Solver

The fluid flow solver that is used for our numerical study is the in-house code EllipSys3D (and its two-dimensional version EllipSys2D) developed in a cooperation between DTU and Risø. It can solve the Navier-Stokes equations for a incompressible fluid. A complete description of the code can be found in the references [2,3,4].

As we are interested in high Reynolds number flows, turbulence modelling has to be considered. Firstly, the k-ω SST turbulence model was used [5]. Calculations using this model will be referred as Reynolds Average Navier-Stokes (RANS) calculations. Secondly, the more sophisticated Detached Eddy Simulation (DES) model which makes use of a Large Eddy Simulation model (and therefore more accurately simulates the dynamics of the turbulent vortices) in the far field, and a RANS approach in the vicinity of the airfoil (in order to avoid the need for highly refined grid in this region of the flow), was used [6,7,8].

Use of 3D Detached Eddy Simulation

As noticed above, transition location can be decisive for airfoil aerodynamic characteristics. In addition to fully turbulent computations, two simplified transition models were implemented. The first one, referred as ‘fixed transition model’, uses the transition location determined in the course of a 2D calculation using the transition

model by Drela [9]. It is enforced as a fixed transition location along the whole span of the 3D airfoil for the corresponding angles of attack. The second model uses also results of 2D computations with Drela's model for which the transition location was stored together with the stagnation point location for the whole range of angles of attack. When a 3D computation is performed, the stagnation point locations at some specified stations along the airfoil span are determined. Then, the transition locations are deduced from the above stored data for each span station. In between these stations, the transition location is linearly interpolated. This will be referred as 'simplified transition model' [15].

Prior to the actual evaluation of the 3D numerical model, a preliminary study was performed in order to investigate the influence of several numerical parameters on the results. In particular, the influence of the mesh refinement, the time-step, and the span width were studied. These results are not included in this report but can be found in [10]. However, it was thereby ensured that the subsequent computations and results that will be presented in the following are consistent.

In the following sections, the four different airfoils are individually studied. Thereafter, a summary of the results is given.

5.2 RISØ-B1-18 Airfoil

This 18% thick airfoil was developed at Risø National Laboratory and tested in the Velux wind tunnel [11]. Note that one of the design constraints was transition-insensitivity around maximum lift. The Reynolds number of the experiment (and computations) is equal to Re=1.6x10^6.

Lift and drag characteristics for the different calculations are gathered on Figure 5-1(a-b). It can be observed that there is a good agreement between all numerical computations and the experimental results in the linear region up to α=10^o. The 2D and 3D RANS calculations predict a lift increase up to an angle of attack equal to 14^o as in the measurements. The 2D calculations predict a lift drop just after stall similar to the measurements. In contrast, 3D DES computations (both fully turbulent and with transition model) predict an earlier stall at α=10^o, and therefore a rather smooth stall lift drop. At higher angles of attack (α>18^o), the 2D computations exhibit a new increase of lift which is not present in the 3D computations and the experimental results.

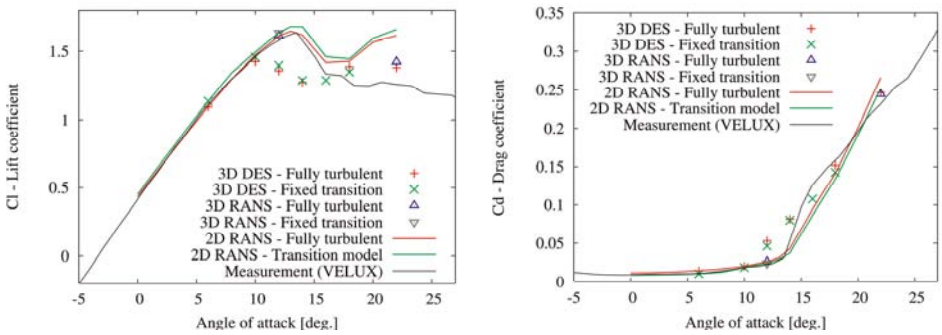

(a) Lift *(b) Drag*

Figure 5-1 Polar Characteristics for RISØ-B1-18 Airfoil

The pressure and skin friction coefficients for α=12^o are displayed in Figure 5-2(a-b). It can be seen that the 3D DES computations exhibit a larger trailing edge separation than the 2D and 3D RANS calculations. This explained the early stall for the 3D DES computations observed above.

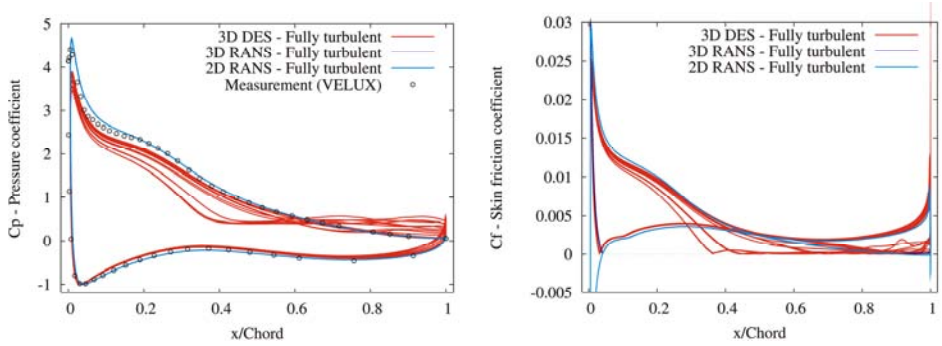

(a) Pressure coefficient *(b) Skin friction coefficient*

Figure 5-2 Pressure and Skin Friction Distributions for RISØ-B1-18 at $\alpha=12^o$

Time-series of the lift for the different calculations are presented in Figure 5-3(a) for $\alpha=22^o$, and for the 3D RANS calculation at several stations along the span of the airfoil in Figure 5-3(b). It can firstly be observed that the 2D calculations does not permit the formation of long time period flow structures, which can be observed in the 3D calculations (in particular the 3D RANS). These are identified as large oscillations of the flow, which form themselves over a long period of time during which the lift is slowly building up (with a non-dimensional characteristic time approximately equal to 80 for the 3D RANS calculation). Then, a rather abrupt lift drop occurs as it can clearly be observed for the 3D RANS calculation. These larger oscillations are superimposed over the 2D vortex shedding phenomenon of much smaller time-period (with a non-dimensional characteristic time approximately equal to 1) observed for most 2D and 3D calculations beyond stall. Figure 5-3(b) clearly shows that the low-frequency phenomenon is two-dimensional (but not captured by the 2D simulation) as both lift and drag time histories at several stations along the airfoil span are very well correlated, both in the case of the 3D RANS and 3D DES calculations. This particular pattern is obviously much more chaotic and three-dimensional in the latter case. It was identified as the shedding of larger vortex of the size of the detached region [10].

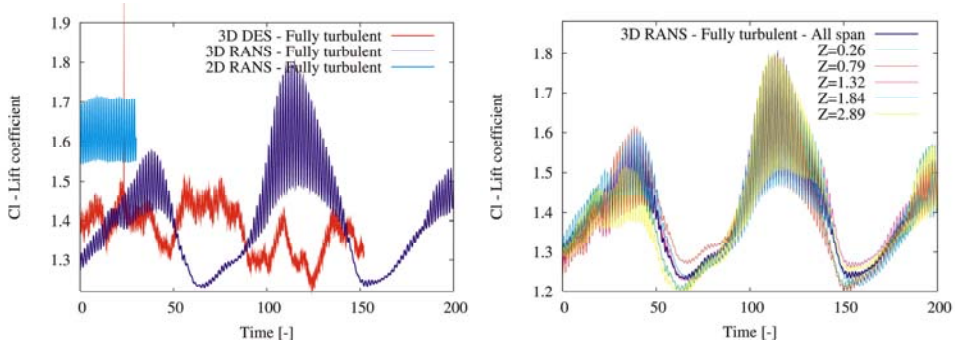

(a) Averaged along span *(b) Several stations along span*

Figure 5-3 Time-series of Lift for RISØ-B1-18 at $\alpha=22^o$

Summary:

This airfoil is characterized by its insensitivity to transition location, which was one of the objectives for its design. This characteristic is well reflected by the numerical calculations. Moreover, there is a general fairly good agreement between the experimental and the computational results. However, two major discrepancies are observed. Firstly, the 3D DES computations (with or without transition modelling)

predict stall occurrence too early. Secondly, the 2D RANS calculations predict a continued increase of lift for high angles of attack ($\alpha>20^o$) which is certainly non-physical, whereas 3D DES calculations are able to reproduce the correct chaotic three-dimensional structures of the fully detached flow.

5.3 NACA 63-430 Airfoil

This 30% thick airfoil belongs to the NACA wing section family. It was measured in the VELUX wind tunnel [12] for a Reynolds number equal to $Re=1.5x10^6$. This airfoil was chosen as large discrepancies between experimental study and 2D numerical computations were observed in a previous study [1].

Lift and drag characteristics for all computations are gathered in Figure 5-4(a-b). It is quite clear that there exist large discrepancies between the different computational results. In particular, the fully turbulent calculations and those with transition model produce quite different results.

Transition locations predicted in the 2D RANS calculations with the model by Drela are plotted on Figure 5-5(a), together with the predictions from the simplified transition model in the 3D DES computations. The discrepancies between the two models is getting larger from $\alpha=10^o$, i.e. when stall starts to occur. Although the transition locations predicted by the simplified transition model are extracted from the 2D RANS calculations with Drela's model, these discrepancies are caused by the downwash created by the three-dimensional airfoil wake which modifies the flow around the airfoil, including the stagnation point location on the pressure side near the leading edge of the airfoil as illustrated in Figure 5-5(b). This stagnation location is actually used for interpolating the transition location within the simplified model, which thus differs from the two-dimensional case and the fixed transition model. The modification of the transition location modifies in turn the flow around the airfoil and the airfoil wake. In the end, the final transition location predicted by the simplified model represents an equilibrium between the computed stagnation point location, airfoil wake and transition location.

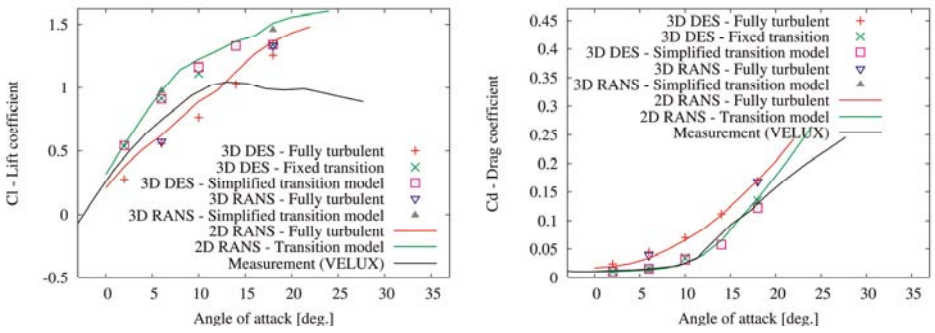

(a) Lift *(b) Drag*

Figure 5-4 Polar Characteristics for NACA 63-430 Airfoil

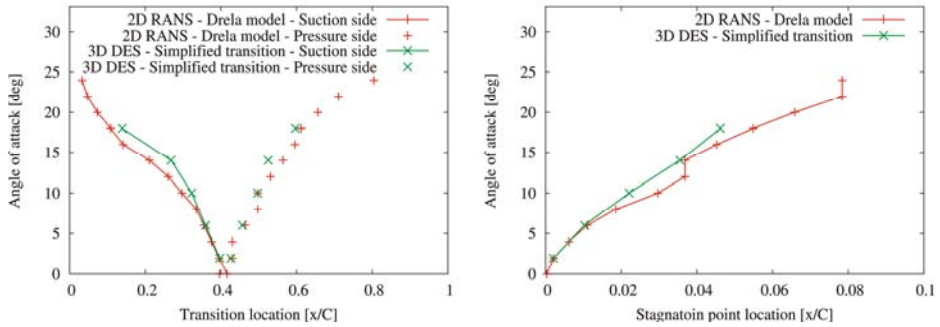

(a) Transition location *(b) Stagnation point location*

Figure 5-5 Transition Model Data for NACA 63-430 Airfoil

The lift (averaged over the airfoil span) time-series for the 3D fully turbulent computations and with the simplified transition model, both with RANS and DES models, are plotted in Figure 5-6(a-b) for angles of attack equal to $\alpha=6^o$ and 18^o, respectively. The data for the 2D RANS computations with transition model are added. It can be seen that, at $\alpha=6^o$, all RANS (2D and 3D) computations predict an almost steady flow, whereas the DES computations predict some degree of unsteadiness, in particular the fully turbulent one. The latter exhibits a longer transient, which can be seen at the beginning of the plotted time-series. At $\alpha=18^o$, both RANS and DES computations exhibit unsteadiness. However, RANS computations predict quasi-periodic flow patterns, whereas the DES computations predict more chaotic flow patterns. It is noted that, even if the 2D and 3D RANS computations with transition model give similar results in average, the amplitude of the oscillations are twice as large for the 2D calculations for $\alpha=18^o$.

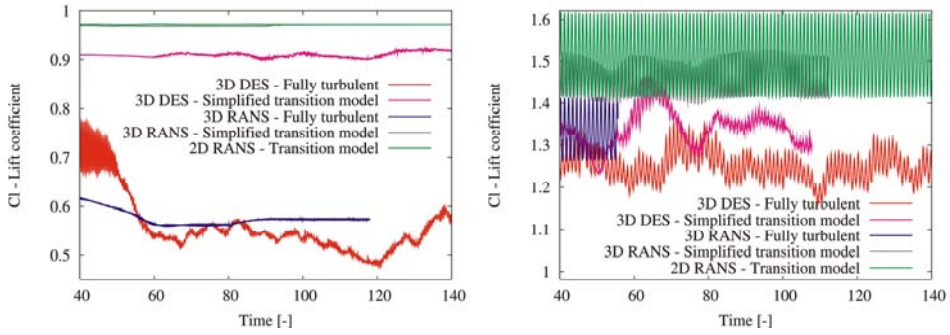

(a) $\alpha = 6^o$ *(b) $\alpha = 18^o$*

Figure 5-6 Time-series of Lift for NACA 63-430 Airfoil

It can be seen that the discrepancies between the computations with and without transition model for the pressure coefficient distribution are great even at lower angle of attack ($\alpha=6^o$, Figure 5-7(a)), resulting in a higher lift prediction for the computations with transition model. This is due to the transition to turbulence located quite far downstream (at $x/C \approx 0.35$) and preventing the development of a thicker turbulent boundary layer upstream this transition location as in the fully turbulent case, which in turn increases the pressure coefficient on the suction side, and therefore increases the lift. This modification of pressure on the airfoil suction side is directly related to the thickness of the boundary layer which modifies the curvature of the streamlines in the flow field in the vicinity of the boundary layer. Thereby, the pressure distribution in the

flow field is also modified, with a direct impact on the airfoil surface pressure distribution. As it can be seen on Figure 5-7(a-b), the computations with fixed transition predict a smaller trailing edge separation in comparison to the fully turbulent results, which seems to be in better agreement with the experimental results as indicated by the pressure coefficient distribution in the vicinity of the trailing edge on the suction side. However, the transition location might be enforced too far downstream as there is a poor agreement of the pressure coefficients before separation occurs.

At higher angle of attack ($\alpha=18^o$, Figure 5-7(b)), the discrepancies are less noticeable between fully turbulent computation and computation with transition. The pressure coefficient distributions around the airfoil contour are distributed in a slightly different way for the computations with and without transition. Moreover, the measured pressure coefficient is quite lower than the computed ones before separation occurs, most probably due to the higher turbulence level in the wind tunnel combined with the difficulty to accurately predict the transition location (possible occurrence of a by-pass transition as noticed in the previous section), or possibly due to the presence of a leading edge laminar separation bubble in the experiment.

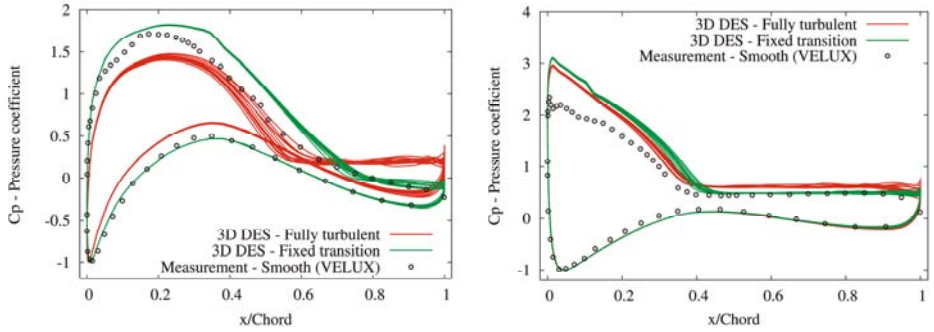

(a) α = 6^o *(b) α = 18^o*

Figure 5-7 Pressure Coefficient Distributions for NACA 63-430 Airfoil

Summary:

NACA 63-430: Airfoil difficult to simulate

The analysis of the results is quite difficult for this particular airfoil, and there is a poor agreement between the experimental and computational results.

RANS and DES computations give quite similar results in average. Nevertheless, the 3D DES computations allow the formation of chaotic three-dimensional structures which are not present in 3D RANS computations. There is no significant improvement by using 3D RANS simulations compared to 2D RANS in average, but 2D computations exhibit non-physical large amplitude oscillations at high angles of attack.

Highly dependent on transition location

This airfoil is highly dependent on transition location as shown by the numerical results. The poor agreement with experimental data probably originates from a by-pass transition phenomenon which is not modelled in the computations, combined with the free-stream turbulence present in the wind tunnel and not modelled in the computations.

5.4 S809 Airfoil

The S809 airfoil is a 21% thick wind turbine airfoil that has been designed at the National Renewable Energy Laboratory (NREL), Colorado, USA, by Somers [13]. The airfoil was tested in the low-turbulence wind tunnel at Delft University of Technology in

The Netherlands [13]. The Reynolds number of the experiment that is considered in this study is Re=1.0x10^6. Note that transition location was measured during the experiment for angles of attack before stall occurs.

Lift and drag characteristics for all computations are gathered in Figure 5-8(a-b).

Before stall occurs, slight discrepancies between the slope of lift predicted by fully turbulent computations and those with transition model can be observed. This is valid both for 2D RANS and 3D DES computations. However, 2D RANS and 3D DES computations are consistent with each other, both with and without the use of a transition model. The measurements are in good agreement with computational results obtained with transition model.

Stall initiates around α=6^o to 8^o in the experiment. Beyond that angle of attack, the experimental lift slowly levels until α=10^o before a small stall lift drop. Then it starts to slightly increase again, and finally drops again to the level measured just after the initial stall. As the angle of attack increases beyond stall, the 2D RANS computations exhibit a continued growth of lift with a slightly smaller slope than before stall. The 3D fully turbulent DES exhibits a similar behavior. However, as stall occurs at α=10^o, the computed lift slope is decreased (which does not occur for the 2D case), resulting in a computed lift very close to the experimental one. A similar conclusion can be drawn from the 3D DES computations with fixed transition model, which are actually giving rather good results in comparison to experimental ones for the whole range of angles of attack.

At α=18^o, all computational methods predict quite higher lift than observed from the experiment. 3D RANS and DES computations with transition model, as well as 3D fully turbulent RANS predict lift levels that are between the extremely high values of the fully turbulent 3D DES and 2D RANS computations and the experimental results.

Beyond α=18^o, all computational methods predict a distinct drop of lift and recover values somehow lower than the measurements for α=20^o.

The transition locations measured in the experiment, together with the one computed with the transition model by Drela [9] during 2D RANS calculations, are displayed in Figure 5-9. It can be seen that there is a relative good agreement between these results. Both data sets show that the transition location on the suction side is very sensitive to the angle of attack around stall (i.e. for angles of attack between α=6^o and 8^o).

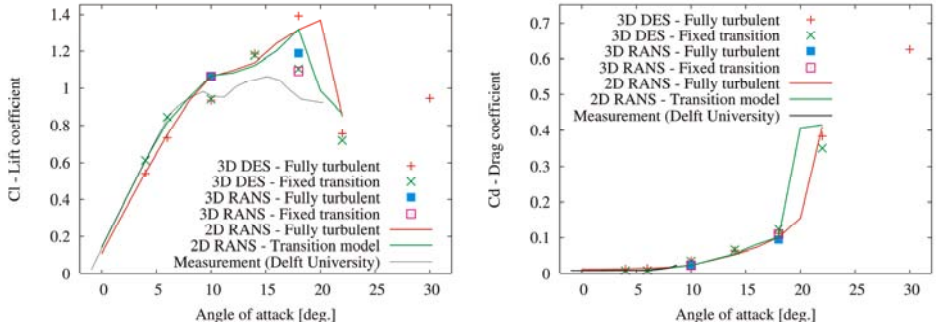

(a) Lift *(b) Drag*

Figure 5-8 Polar Characteristics for S809 Airfoil

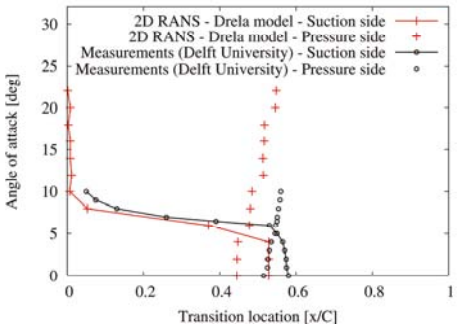

Figure 5-9 Transition location for S809 Airfoil

Figure 5-10 and Figure 5-11 display the pressure and skin friction coefficient distributions computed with transition model for angles of attack equal to $\alpha=10^o$ and 18^o, respectively. Again, at $\alpha=10^o$, the 2D and 3D RANS calculations predict a smaller trailing edge separation than the 3D DES calculation. At $\alpha=18^o$, both 3D RANS and 3D DES gives similar results in average, although the DES computation is more three-dimensional and chaotic along the airfoil span. These three-dimensional chaotic structures of the 3D computations seem to be responsible for the lower pressure coefficient distribution on the suction side, and thereby the lower lift level observed in Figure 5-8(a).

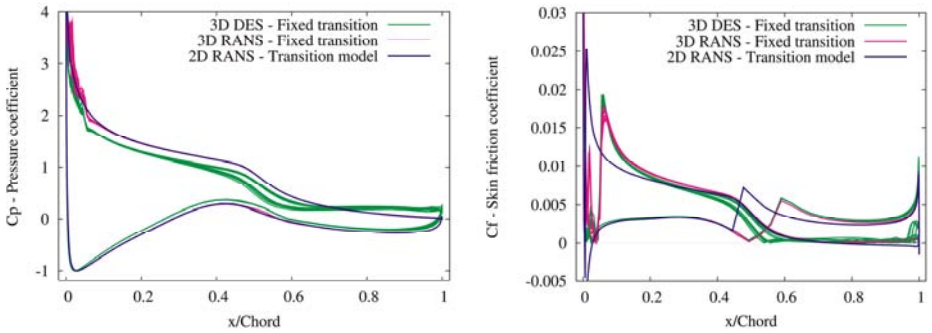

(a) Pressure coefficient *(b) Skin friction coefficient*

Figure 5-10 Pressure and Skin Friction Distributions for S809 at $\alpha=10^o$

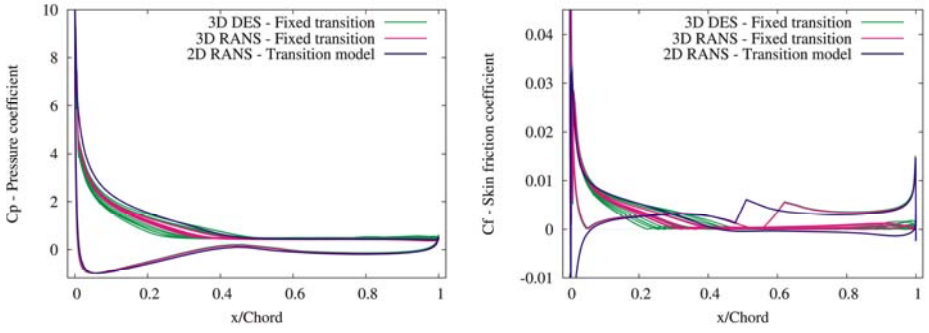

(a) Pressure coefficient *(b) Skin friction coefficient*

Figure 5-11 Pressure and Skin Friction Distributions for S809 at $\alpha=18^o$

The effect of the turbulence model can clearly be observed on Figure 5-12(a-b) which display both the airfoil surface pressure isovalues, and the vorticity isovalues at two cross-sections along the blade. Indeed, the 3D DES computation exhibit turbulent

structures both near the airfoil and in the wake which are not present in the 3D RANS computation.

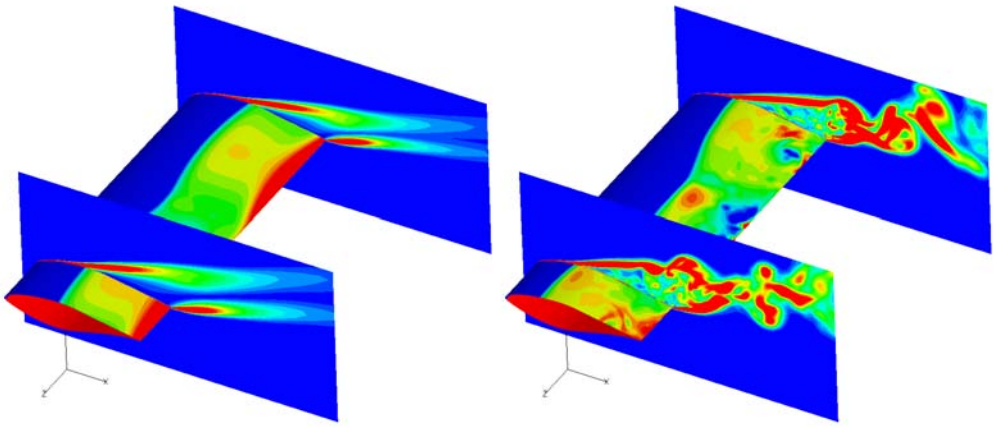

(a) 3D RANS computation *(b) 3D DES computation*

Figure 5-12 Surface Pressure and Cross-section Vorticity Isovalues at α = 18^o

Summary:

According to the computational results, this airfoil is sensitive to transition both in the linear and in the stall region. It is clear that DES modelling is necessary to accurately predict stall occurrence. Some discrepancies with the experimental results are observed after stall and before full separation of the flow on the suction side. Indeed, all computational methods predict a too high increase of lift as the angle of attack increases in this region. Transition modelling seems to improve the results in this case. Moreover, the 3D computations perform better than the 2D ones, except for the fully turbulent 3D DES calculation just before full separation of the flow. The 3D DES computations with transition model are performing quite well compared to experimental results.

S809: 3D DES with transition correctly captures stall

5.5 DU 93-W-210 Airfoil

This 21% thick airfoil was designed by Timmer at Delft University of Technology, The Netherlands [14]. It was tested in their low-turbulence wind tunnel. Measurements were performed at a Reynolds number equal to *Re*=1.0x10^6.

Lift and drag characteristics for all cases are gathered in Figure 5-13(a-b). It is clear that computations with transition model give results in better agreement with measurements before stall, and a marginal improvement after stall. However, it seems that all computations predict a continued growth of lift after stall (for α>14^o), whereas experimental results exhibit a nearly constant lift after stall. However, 3D DES computation predicts a distinct drop in lift for α=24^o. Drag is quite well predicted by computational methods, except for the fully turbulent computations (as it was observed for the lift), and around stall.

The transition locations as a function of the angle of attack predicted by the 2D RANS computations with the model by Drela, together with the results of the simplified transition model in the 3D DES calculations, are plotted on Figure 5-14. A discussion on the discrepancies between the transition locations predicted by the simplified transition model and the 2D RANS computations is available in section 5.3.

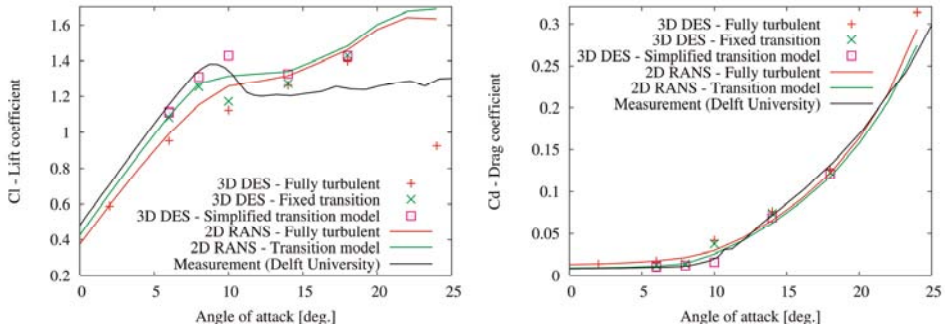

(a) Lift *(b) Drag*

Figure 5-13 Polar Characteristics for DU 93-W-210 Airfoil

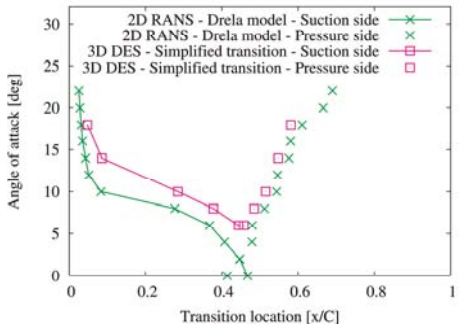

Figure 5-14 Transition location for DU 93-W-210 Airfoil

It is interesting to note that the fixed transition model and the simplified transition model behave very differently around stall, i.e. for $\alpha = 10^o$. The only difference between the two models is the fact that the simplified transition model uses the stagnation point to determine the transition location. Indeed, it can be seen both on Figure 5-15(b), and from the transition location on Figure 5-14, that transition occurs much closer to the leading edge for the computation with fixed transition model (the 2D RANS transition location being the one enforced in the 3D DES computation with fixed transition). This results in a trailing edge separation for the computation with fixed transition model, which does not occur with the simplified transition model, explaining the earlier stall for the computations with fixed transition model observed on Figure 5-13.

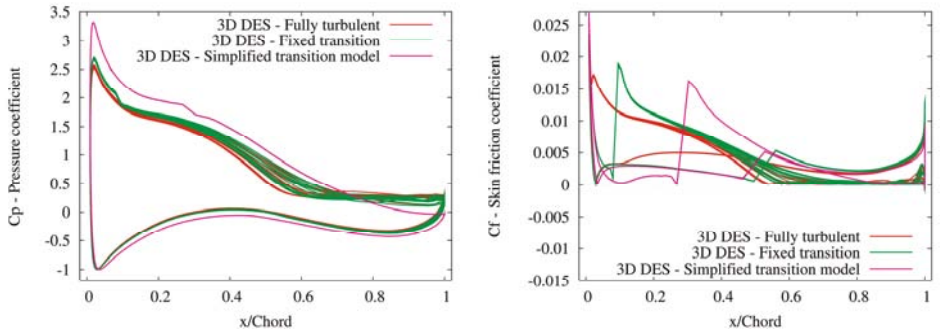

(a) Pressure coefficient *(b) Skin friction coefficient*

Figure 5-15 Pressure and Skin Friction Distributions for DU 93-W-210 at $\alpha = 10^o$

At $\alpha = 24^o$ (Figure 5-16(a-b)), it can be seen that the 3D DES computation is detached almost everywhere on the suction side of the airfoil explaining the drop of lift in Figure

5-13 for that angle of attack, whereas 2D computations only predict a detachment starting around the 1/4 chord.

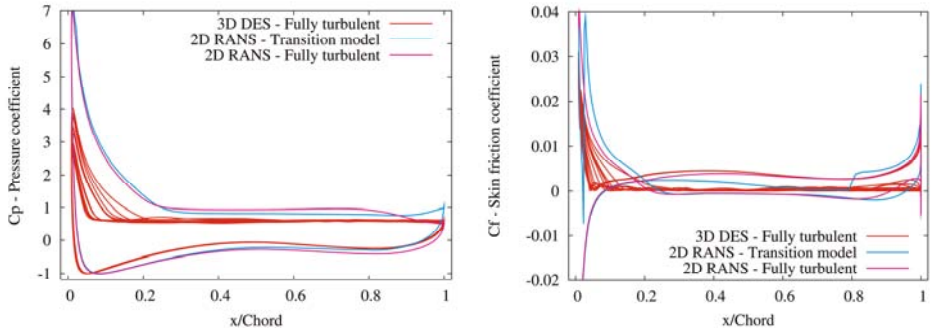

(a) Pressure coefficient *(b) Skin friction coefficient*

Figure 5-16 Pressure and Skin Friction Distributions for DU 93-W-210 at $\alpha=24^o$

Summary:

DU 93-W-210: Sensitivity to transition in linear region

According to the computational results, this airfoil is sensitive to transition in the linear region and around stall, but in a lesser degree beyond stall. The same phenomenon of continued lift increase after stall is occurring again as observed for the S809 airfoil (see section 5.4). 3D computations are necessary to simulate the three-dimensional chaotic structures present at high angles of attack.

5.6 Analysis and Summary of the Results

Classification of the results of the study

In this section, it is attempted to make a synthesis of the results obtained for the different airfoils. Considering the rather large amount of data, and the many conclusions that can be drawn for general and particular cases, the results will be classified in a two-entry array fashion. On one side, the results will be interpreted according to the ranges of angle of attack that characterize different types of flow conditions:

- *Linear region*, i.e. angles of attack for which the lift slope is nearly constant (at least according to potential theory), and nearly constant drag.
- *Around stall*, i.e. for angles of attack immediately preceding stall occurrence as well as immediately following.
- *Stall region*, i.e. angles of attack for which stall has already occurred, usually characterized by a rather constant lift but rapidly increasing drag.
- *Deep stall*, i.e. higher angles of attack relatively far from stall occurrence for which the flow over the airfoil suction side is completely detached.

The second parameter for our classification will be the comparison of results according to the physical models that are used for the computations. The following comparisons are performed:

- Comparison between 2D and 3D computations
- Comparison of RANS and DES computations
- Influence of transition modelling

Note that in these comparisons, the experimental results will be taken to a certain extent as a reference, but it is important to keep in mind that in this study we are actually more

interested in the analysis of the different numerical and physical models relatively to each other (i.e. 2D vs. 3D computations, RANS vs. DES, and fully turbulent vs. transition modelling).

The conclusions that will be drawn in the following are not always general, and cannot be taken for granted for all types of airfoils. Indeed, the four different airfoils that are studied in this work are quite different from each other insofar as they exhibit quite different behaviors.

Linear Region

Comparison 2D/3D

3D effects are usually not relevant, except for thick airfoils (such as the NACA 63-430 airfoil, which anyway does not exhibit a distinct linear region before stall. In particular, trailing edge separation and unsteady effects are already present for low angles of attack).

Comparison RANS/DES

There is a low sensitivity to RANS/DES computational models, as the LES component of the DES model is not active in this case.

Influence of Transition

Transition is usually decisive for the prediction of lift slope. However, airfoils which are designed to be transition-insensitive (such as the RISØ-B1-18 airfoil) do not follow this rule.

Around Stall

Comparison 2D/3D

3D effects always play a role in the prediction of stall occurrence. However, in some cases, 2D computational results can be closer to experimental ones.

Comparison RANS/DES

3D RANS computations usually give results closer to the 2D RANS than the 3D DES calculations. Note that 3D RANS calculations can give results closer to the experimental ones than the 3D DES calculations.

Influence of Transition

The implementation of a transition model, as well as the type of transition model, modifies noticeably the stall characteristics. It is indeed an essential component of the computations as it directly affects separation and the subsequent stall.

Stall Region

Comparison 2D/3D

3D effects always play a role for stalled airfoil. In particular, it can usually be observed that oscillations associated to vortex shedding have higher amplitudes in the 2D computations than in 3D.

Comparison RANS/DES

3D RANS computations doesn't capture the full turbulent wake structure that develops after stall, however they usually give sensible results as far as averaged values are concerned.

Influence of Transition

Transition modelling is playing an important role for 2D RANS computations. It can induce unsteady effects for 3D DES computations which are not present in the fully turbulent case.

Deep Stall

Comparison 2D/3D

3D computations are necessary. 2D calculations usually become non-physical.

Comparison RANS/DES

The conclusions are the same as in the stall region. But again, usually the discrepancies observed between the mean values of lift and drag are not large. Discrepancies are mainly observed on the time-variations of these values.

Influence of Transition

Transition is not relevant as the flow is always completely detached on the suction side of the airfoil, and can therefore be considered as fully turbulent.

Summary

Several factors can play a role at the same time which can make it difficult to correctly analyze the results. Therefore, it is quite difficult to give general answers. Moreover, only four airfoils (even if representative of typical airfoil behaviors) have been studied.

Importance of transition modelling

One of the main conclusions of the study, even if already well-known, is the fact that transition is a major factor for the prediction of aerodynamic characteristics. In one case (for the NACA 63-430 airfoil), it is surmised that the transition model used in our computation is not suitable for comparison with the available experimental results. Indeed, in this case a by-pass transition model is probably needed (as indicated by 2D calculations in [15]). Another possible remedy might be the implementation of an actual 3D transition model, as the three-dimensionality of the flow might interact with transition location along the blade.

3D DES computations necessary to capture 3D turbulent wake

Another important conclusion is the fact that only 3D DES computations are able to reproduce the actual chaotic and three-dimensional of the turbulent wake in stall. This becomes relevant as far as one is interested in the unsteady aerodynamic loads that can be experienced by an airfoil.

3D DES computations not always closest to measurements

Finally, it was observed in some cases that models which are expected to be more accurate (3D vs. 2D, DES vs. RANS) are not always giving the best results when compared to experimental ones. Several conclusions can be drawn from this fact. Firstly, the validity of the experimental data is always a subject of concern as there is never full control of all experimental and measurement conditions, as well as the wind tunnel effects. Secondly, and which is more relevant for the present study, it is not always given beforehand that the use of a particular model is valid or justified. For example, 3D DES computations with a too coarse or too distorted computational grid, or a transition model ill-calibrated for the considered experiment, will most probably produce erroneous results.

5.7 Conclusion

A large number of numerical Navier-Stokes simulations involving two- and three-dimensional computations, RANS and DES modelling, fully turbulent computations or

with transition model, have been performed. Four different airfoil profiles were considered. The results were compared and analyzed.

Several mechanisms explaining the discrepancies between the different numerical simulations, and some of the experimental results, have been identified. However, these conclusions cannot in general be applied to all types of airfoils. The two major conclusions of this work are the dependency of computational results to transition modelling, and the ability of 3D DES calculations to realistically simulate the turbulent wake of an airfoil in stall.

5.8 References

[1] Bertagnolio, F., Sørensen, N.N., Johansen, J. and Fuglsang, P., 2001, ``Wind Turbine Airfoil Catalogue", Tech. Report Ris{\o}-R-1280(EN), Ris{\o} National Laboratory, Roskilde, Denmark, 2001.

[2] Michelsen, J.A., ``Basis3D - A Platform for Development of Multiblock PDE Solvers", Tech. Report AFM 92-05, Technical University of Denmark, Lyngby, Denmark, 1992.

[3] Michelsen, J.A., ``Block Structured Multigrid Solution of 2D and 3D Elliptic PDE's", Tech. Report AFM 94-06, Technical University of Denmark, Lyngby, Denmark, 1994.

[4] Sørensen, N.N., ``General Purpose Flow Solver Applied to Flow over Hills", PhD Thesis, Tech. Report Risø-R-827(EN), Risø National Laboratory, Roskilde, Denmark, 1995.

[5] Menter, F.R., ``Zonal Two-Equations k-ω Turbulence Models for Aerodynamic Flows", AIAA Paper 93-2906, 1993.

[6] Spalart, P.R., Jou, W-H., Strelets, M. and Allmaras, S.R., ``Comments on the Feasibility of LES for Wings, and on a Hybrid RANS/LES Approach", Proc. of 1st. AFOSR Int. Conf. on DNS/LES, Ruston, LA, Greyden Press, Columbus, OH, August 4-8,1997.

[7] Strelets, M., ``Detached Eddy Simulation of Massively Separated Flows", 39th AIAA Aerospace Sciences Meeting and Exhibit, AIAA Paper 2001-0879, Reno, NV, 2001.

[8] Johansen, J., Sørensen, N.N., and Michelsen, J.A., ``Detached-Eddy Simulation of Flow around the NREL Phase-VI Blade", Wind Energy, Vol.5, pp.185-197, 2002.

[9] Drela, M. and Giles, M. B., ``Viscous-Inviscid Analysis of Transonic and Low Reynolds Number Airfoils", AIAA Journal, Vol.25, No.10, pp.1347-1355, 1987.

[10] Bertagnolio, F., Sørensen, N.N., and Johansen, J., ``Profile Catalogue for Airfoil Sections Based on 3D Calculations'', Tech. Report, Risø National Laboratory, Roskilde, Denmark (to be published).

[11] Fuglsang, P., Bak, C., Gaunaa, M. and Antoniou, I., ``Wind Tunnel Tests of Risø-B1-18 and Risø-B1-24", Tech. Report Risø-R-1375(EN), Risø National Laboratory, Roskilde, Denmark, 2003.

[12] Fuglsang, P., Antoniou, I., Sørensen, N.N. and Madsen, H.Aa., ``Validation of a Wind Tunnel Testing Facility for Blade Surface Pressure Measurements", Tech. Report Risø-R-981(EN), Risø National Laboratory, Roskilde, Denmark, 1998.

[13] Somers, D.M., ``Design and Experimental Results for the S809 Airfoil", Tech. Report NREL/SR-440-6918, National Renewable Energy Laboratory, Colorado, USA, 1997.

[14] Timmer, W.A., ``The Design and Testing of Airfoil DU 91-W2-250", 6th IEA Symposium on the Aerodynamics of Wind Turbines, Petten, The Netherlands 1992.

[15] Aeroelastic Research Program EFP-2001, Madsen, H.A. (ed.), Tech. Report Risø-R-1349(DA), Risø National Lab., Roskilde, Denmark, 2002.

6 Aeroelastic response in extreme wind cases

Gunner C. Larsen, Kurt S. Hansen, Torben J. Larsen, Jakob Mann

Verification of the structural integrity of a wind turbine structure involves analyses of *fatigue loading* as well as *extreme loading* arising from the environmental wind climate.

Traditionally, the *fatigue load* estimation is based on detailed aeroelastic simulations of turbines subjected to (time/space) high resolution synthetic turbulent wind fields reflecting correctly the second order statistics of the natural turbulence. Contrary to the fatigue loading, the *ultimate loading* is presently dealt with in a somewhat rudimentary manner based on the specifications in the draft IEC-standard, IEC61400-1 [1], where wind gust events are formulated as coherent gusts of an inherent deterministic character, whereas the gusts experienced in realistic physical situations are of a stochastic nature with a limited spatial extension. This conceptual difference may cause substantial differences in the load- and response patterns of a wind turbine when a gust event is imposed [2].

The purpose of the present work is to initiate a process where todays state-of-the-art extreme load specifications eventually are replaced by physically more realistic stochastic extreme load cases. To achieve this goal the following is required:

- A "gust generator" that facilitate generation of consistent synthetic turbulence fields, consisting of fully 3D multiple correlated stochastic processes, containing one or more extreme events (arbitrarily distributed in space and/or time), with the second order structure functions correctly represented;
- A statistical model that, for a given set of turbulence characteristics and an arbitrary selected return period, can predict realistic (most likely) gust amplitudes as input for the "gust generator" on a rational basis.

This work is carried out to initiate a process, where todays extreme load specifications eventually are replaced by physically more realistic stochastic extreme load cases

The requested "gust generator" has been formulated and implemented in a numerical tool as part of a previous EFP-project (*A 3D wind simulator for determination of extreme- and fatigue loads*) [3], [4].

The present contribution deals partly with illustration of the capacity of the "gust generator", partly with development of a statistical model for an especially simple gust event, and it falls accordingly in two parts. The *first part* uses the developed "gust generator" to demonstrate the importance of considering stochastic gust events as an alternative to today's stylized deterministic coherent gust specifications. This study furthermore stresses the importance of a site specific determination of gust amplitudes. In line with that, the *second part* deals with development of a consistent statistical extreme value model for the simplest possible gust type – a one point wind speed increase.

6.1 The importance of a stochastic formulation of extreme gusts

The capacity of the "gust generator" is demonstrated by emulating a measured full scale extreme negative wind shear event. The measured shear gust amplitude turns out to be of the same order of magnitude as the magnitude of the stylized coherent shear gust event specified in the IEC61400-1 code, although the experiment lasted 3 months only, whereas the IEC gust specifications represents a 50 year recurrence period.

Subsequently, a comparison of the different *response patterns*, resulting from these two load cases, is conducted by assing the respective aeroelastic responses of a fictitious wind turbine. A slightly more detailed version of the work was presented at the EWEC'06 conference [5].

The concept of constrained simulation

A very versatile theory for simulation of Gaussian turbulence driven gust situations has been developed

To introduce more realistic extreme load situations of a stochastic nature, a very versatile theory for simulation of Gaussian *turbulence driven* gust situations has been developed [3], [4].

The theory meets the requirements stated in the introduction and provides generation of consistent synthetic turbulence fields with arbitrarily defined extreme events embedded. The spatial extent of these events results directly from the cross correlation properties of the "basic" stochastic field in which they are imbedded.

Within the framework of the derived formalism, an extreme event is defined in terms of an arbitrary number of constraints, each expressed as a linear combination of an arbitrary number of turbulence field velocity components and/or their derivatives. The theory has, in the present context, been implemented in a framework, where the basic stochastic field is generated using the Mann spectral tensor formalism as developed in [6], [7]. However, the gust theory also allow for alternative formulations of the basic stochastic turbulence field.

Constrained simulation applied on an extreme shear event

The capacity of the developed "gust generator" is demonstrated by emulating a measured violent extreme negative wind shear event from the complex Tauste site in Spain. The orography of this site is illustrated in Figure 6-1, where also the positions of the two erected meteorological masts are indicated.

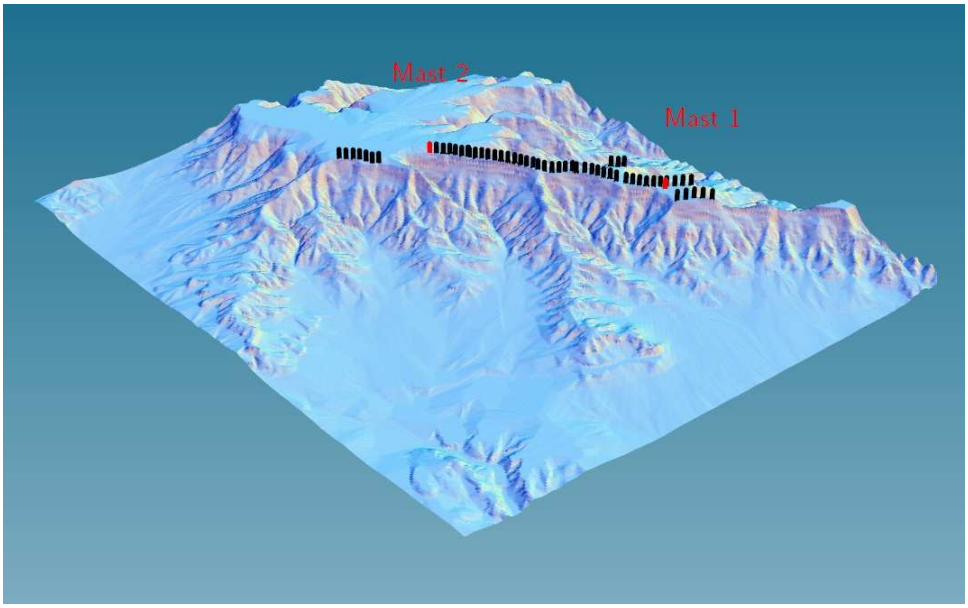

Figure 6-1. Tauste site with indication of positions of the meteorological masts.

The analysis relates to measurements monitored at Mast 2, which is instrumented in five different levels. Detailed information on the instrumentation is given in Table 6-1.

Table 6-1. Instrumentation of Mast 2.

Height[m]	Wind speed sensor	Wind direction sensor
48.0	Cup anemometer	-
42.3	Cup anemometer	Vane
30.6	Cup anemometer	Sonic
18.7	Cup anemometer	Vane
10.0	Cup anemometer	Vane

Only the four upper sensor levels are relevant for the wind conditions imposed on a medium size wind turbine, as the lower level is below the area swept by the rotor, and of the remaining the sensor in 48.0m has further been neglected due to the limited separation between the two upper sensors. An analysis of available wind speed time series, referring to the relevant three levels, has identified the serious/violent negative shear gust event depicted in Figure 6-2. This event is associated with a 10-minute mean wind speed in 42.3m equal to 12.4m/s, and the corresponding turbulence intensity equal to 34%. It is noted that, in a (pitch controlled) wind turbine load context, the observed mean wind speed is in the critical mean wind speed regime, where the wind turbine is starting to pitch its blades and where, as a consequence, the blade loading/deflections are expected to peak.

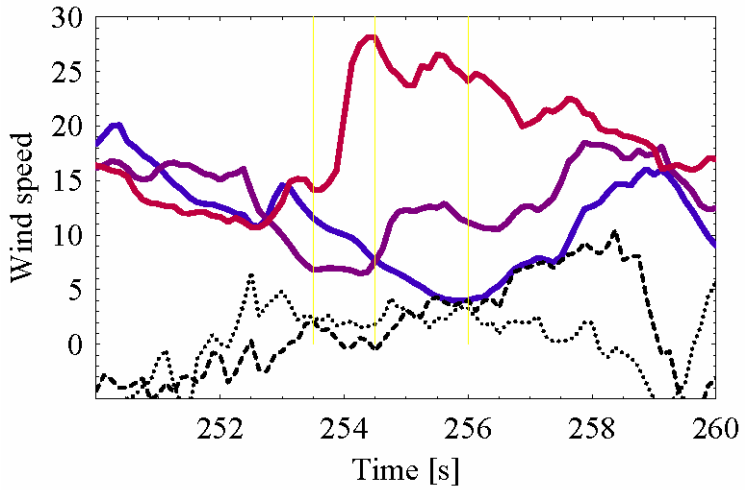

Figure 6-2. Extreme negative shear event identified from measurements (blue: u *at 42.3m; purple:* u *at 30.6m; red:* u *at 18.7m; dashed:* v *at 42.3m; blue:* v *at 18.7m).*

A synthetic stochastic field with a gust event embedded that exhibits the same characteri-stics as a measured gust event is generated

To simulate a synthetic stochastic field with a gust event embedded that exhibits the same characteristics as the measured gust event, constraints reflecting these characteristics have to be defined. Two different realizations of such fields are generated (in the following referred to as realization 1 and realization 2, respectively). These realizations are defined by up to 15 constraints, representing/covering different time instants, different turbulence components, and different locations in space. Denoting the longitudinal turbulence component by *u*, and the transversal turbulence component by *v*, the detailed constraints imposed in the stochastic turbulence simulation are specified in Table 6-2. All the constraints defined in Table 6-2 have been used in the simulation of realization 2, whereas only 6 constraints have been used to define realization 1 (the specifications marked with blue numbers).

Table 6-2. Definition of imposed wind field constraints.

Time	254s-0.5s	254s+0.5s	254s+2.0s
u; 42.3m	11.58m/s	7.73 m/s	4.05m/s
u; 30.6m	6.81 m/s	7.62 m/s	11.19m/s
u; 18.7m	14.16 m/s	28.1 m/s	24.11m/s
v; 42.3m	2.13m/s	-0.59m/s	4.00m/s
v; 18.7m	2.46m/s	1.86m/s	3.30m/s

The measured *mean wind speed shear* has been parameterized as (19.1m–0.156 × z)/s, where z denotes the height above ground level in meters. The parameters used in the Mann turbulence model are L = 72m; $\alpha\varepsilon^{2/3} = 1.4\ \mathrm{m}^{4/3}\mathrm{s}^{-2}$; and $\Gamma = 0.15$; i.e. rather isotropic turbulence.

For *realization 1*, the resulting synthetic turbulence field is shown in several slices along the time axis in Figure 6-3 and Figure 6-4 for the *u*- and *v*-turbulence component, respectively. This 3D-like depiction gives a good impression of the spatial extent of the defined gust event, which is determined partly by the defined constraints, partly by the second order structure functions associated with the stochastic wind field in which the gust event is embedded.

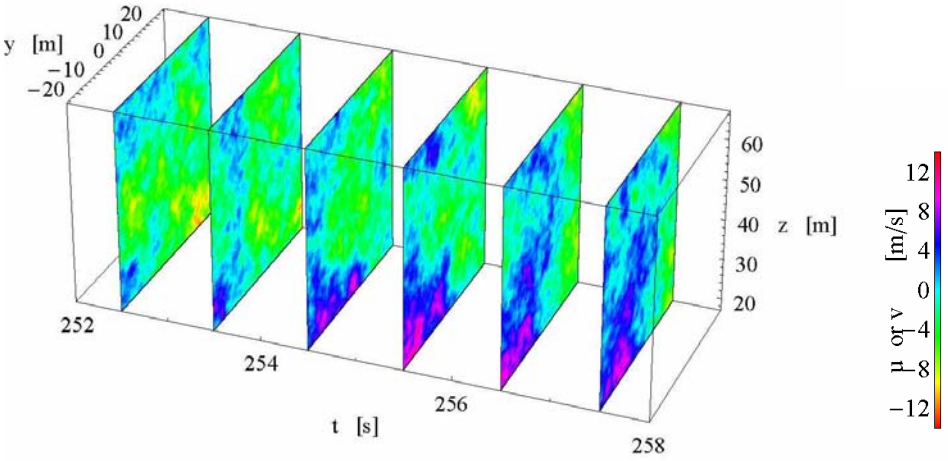

Figure 6-3. The synthetic 3D u-turbulence field; realization 1.

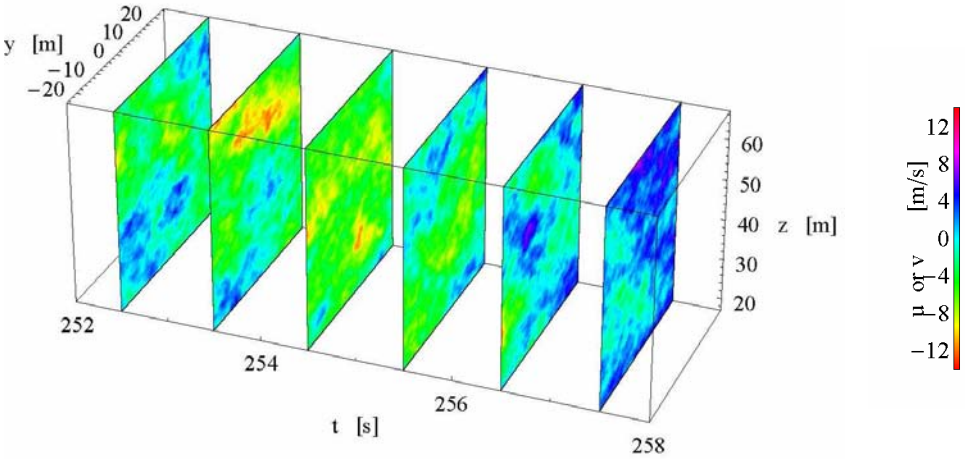

Figure 6-4. The synthetic 3D v-turbulence field; realization 1.

The simulated analogies to the graph displaying measured wind speeds (in the mean wind direction), shown in Figure 6-2, are presented for the two stochastic realizations in Figure 6-5 and Figure 6-6, respectively, for the three heights used in the definition of the imposed constraints. As seen the measured and synthetic fields are identical at the time/spatial points where the constraints are imposed as expected. The turbulence "regime" outside the points, in which the constraints are imposed, are stochastic realizations and will as such differ from simulation to simulation, when different seeds are applied in the turbulence generation. However, in the time regime close to the time instants where constrains are imposed, there is a good qualitative agreement between measured- and simulated fields, indicating that the selected constraints are sufficient for generating the requested wind gust event.

Extreme Wind Shear event as specified in IEC 61400

The IEC 61400 [1] code prescribes a range of wind load conditions to be considered in the design of a wind turbine to assure its structural integrity. For extreme tilt- and yaw loading, the load case denoted Extreme Wind Shear (EWS) applies. The EWS load case specifies two *deterministic* completely *coherent* transient wind gusts describing a vertical and a horizontal shear, respectively. The sign of the horizontal wind shear transient must be chosen such that the most critical loading occur. The parameters defining the deterministic gust events depend on the selected turbulence category through the representative turbulence standard deviation, the relevant longitudinal turbulence scale parameter (defined by the hub height), and the rotor diameter. The specified deterministic (shear) gust is to be superimposed upon mean wind speeds corresponding to the cut-out wind speed and to the wind speed at which rated power is achieved, respectively. The relevant vertical extreme shear event, applicable for the selected turbine, is illustrated in Figure 7, whereas the horizontal shear event is shown in Figure 6-8.

Aeroelastic modelling of the extreme shear event

The generated stochastic extreme shear wind field has subsequently been used as input to an aeroelastic simulation along with an extreme shear event as specified in the IEC 61400 code [1].

The generated stochastic extreme shear wind field has been used as input to an aeroelastic simulation along with an extreme shear event as specified in the IEC 61400 code

The aeroelastic code HAWC2 is used to simulate the response from a turbine subjected to the synthetic stochastic gust event. HAWC2 is an aeroelastic code recently developed at Risø National Laboratory. The code replaces the older code HAWC [8], which for many years have been state-of-the-art within wind turbine response codes. The HAWC2 code is based upon a structural multi-body formulation, where the turbine is divided into a number of bodies: Each body is modelled by using a specified number of Timoshenko beam elements, and the bodies are interconnected by a set of coupling constraints. This method allows for arbitrarily large rotations between the bodies and their associated nonlinear effects, where the deformation within a body is based on linear calculations. The benefits from this approach, compared to the old HAWC model, are especially pronounced for turbines that have a high flexibility and are subjected to large external loading and consequently submitted to large deflections. A previous study has shown that these effects are important for a proper calculation of the tip deflection, for the coupling between blade flap and blade edgewise deflections, and for the twist of the blade [9]. The aerodynamics are based on the BEM-theory but extended to handle effects from large deflections, dynamics in the induction (dynamic inflow), large yaw errors and dynamic stall.

For the present simulations a typical PRVS (pitch regulated with variable speed) turbine with a nominal power of 600kW has been modeled. The rotor diameter is 47m, and with a hub height of 46m, the lowest tip position is 22.5 m above ground. The clearance between blade tip and tower is 3.5m in the non-deflected situation.

Regarding the deterministic wind conditions to be combined with the stochastic gust event, a linear negative wind shear with a gradient of 0.15577 (m/s)/m, corresponding to the measured mean wind field, has been used. The turbulence intensity is 0.34 at hub height, and a high resolution turbulence grid with 64x64 points for the horizontal and vertical directions has been used. The measured violent gust event refer to a mean wind speed at hub height equal to 12.5m/s, and thus allows for a meaningful comparison with the code extreme shear case in the *rated power* mean wind speed situation.

Structural response

The generated stochastic extreme shear wind field has been used as input to an aeroelastic simulation along with an extreme shear event as specified in the IEC 61400 code

The results from the aeroelastic computations are shown in Figure 6-5 – Figure 6-8, where different structural loads are assessed with respect to their damaging potential. In Figure 6-5 the structural transients caused by gust realization 1 are shown. The specified shear gust event is imposed at the low part of the rotor, which causes *large blade deflections* and *significant tilt and yaw loads*. It is rather obvious that the tilt loads are affected by a gust of the specified type, whereas the resulting large yaw loads are a bit more surprising. A detailed analysis reveals that these yaw loads result from the combination of a high longitudinal wind speed with negative shear, and a rather high lateral wind speed (cf. Figure 6-4) of approximately 8m/s. As seen the induced yaw moments are negative (clockwise seen from above). The main reason for these yaw moments being negative, when the turbine is subjected to high wind speeds in the lower part of the rotor (when blade pitch angles are higher than zero), is caused by a combination of negative angles of attack for the inflow at the upper part of the rotor, and high angles of attack characterizing the inflow at the lower part of the rotor. The negative angle of attack at the upper part of the rotor causes a blade force characterized by its component in the mean wind direction being directed opposite to the wind direction, and thus resulting in a negative yaw moment contribution. The high angle of attack characteristic for the lower part of the rotor results in blade forces with their component in the mean wind direction being directed along the wind direction, and consequently also causing a negative yaw moment contribution. For this reason, it should be expected that wind turbines, positioned at locations where negative shear gusts occur frequently (mountainous terrain), will often be exposed to severe negative yaw moments.

Yaw loading is also observed to result from the deterministic load case characterized by an extreme vertical shear (cf. Figure 6-1), but the size of the induced yaw loads are, however, higher for the specified stochastic gust event, which in addition displays a significantly more violent dynamic behavior. For the present wind turbine it is moreover interesting to notice that the tip deflection, as caused by the specified stochastic gust event, is larger than the tip deflecting resulting from the extreme shear gusts event defined by the IEC 64100 code, whereas the imposed tilt loading is less. Note, however, that stochastic tilt loading refer to a turbulence loading where constraints are imposed on the lower part of the wind turbine rotor, as measurements are available in this regime only. As a consequence of the limited spatial extent of gust events generated with the applied “gust generator”, the gust generated part of the shear, in the regime of the upper part of the rotor, is expected to diminish with increasing distance to the highest altitude at which constraints are imposed (cf. Figure 6-3). If measurements were available for the upper part of the rotor, and if these measurements had shown that measured extreme

shear events should be extended to the upper part of the rotor (as is the case for the deterministic shear specified in the IEC code), a constrained simulation of such an event would most likely result in increased tilt loading, but probably also lead to a decrease in the tip deflection.

Figure 6-5 shows the wind turbine loading caused by the second stochastic gust realization. The character of the dynamic turbine response, as evaluated in terms of deflection and rotor loading, deviates somewhat, reflecting the stochastic character of the imposed load event outside the space/time points where the constraints are imposed. The observed deflection and load magnitudes are, however, in general of comparable sizes. As an exception, note that the blade deflections resulting from the first stochastic realization, except for the expected phase shift, are very similar, whereas large deviations between the individual blade peak deflections are observed to result from the second stochastic realization.

The observed deviations between the two stochastic realizations, where e.g. some of the observed extreme responses are associated with time instants before the extreme gust event is imposed, illustrate that it may be difficult *a priori* to determine the "anatomy" of a *critical* extreme (shear) gust event due to the complicated interaction between wind turbine aerodynamics, control, and structural dynamics. Related to this recognition is that some scatter between stochastic realizations of the same gust "basic" event is to be expected, and therefore more than one realization needs to be considered.

As mentioned, the observed yaw loading, caused by the stochastic *vertical* shear event, exceeds the similar response caused by the code specified extreme *vertical* shear event. To investigate whether the large observed yaw loads, originating from the *vertical* stochastic gust event, are "captured" by the extreme *horizontal* IEC 64100 load case, the aeroelastic response associated with this load case has been simulated. The results are presented in Figure 6-8. Comparing the two deterministic code specified load cases (Figure 6-6 and Figure 6-8), the main result is (as expected) that the roles of the tilt and yaw loading are more or less interchanged. The resulting yaw loads are seen to exceed the yaw loading arising from the stochastic *vertical* shear. It should, however, be noted that, intuitively, extreme yaw loading is expected to be closely related to a stochastic *horizontal* shear, and that analysis of such an event most likely will result in increased yaw loading compared to the investigated stochastic gust events.

Finally, it should be noted that the extreme shear event specified in the IEC 64100 code refers to a recurrence period of *50 years*, whereas the measured shear event is obtained from a *3 month* recording period only. Therefore, it is expected that if an extreme value analysis is performed on the available measured shear gust events, the resulting estimate, corresponding to a 50 year period, will display a substantial increase in the shear gust magnitudes, and thus potentially be much more critical for the turbine than the directly recorded event. This fact accentuates the need for a tool for site specific determination of the most likely gust amplitudes, given that a recurrence period has been specified.

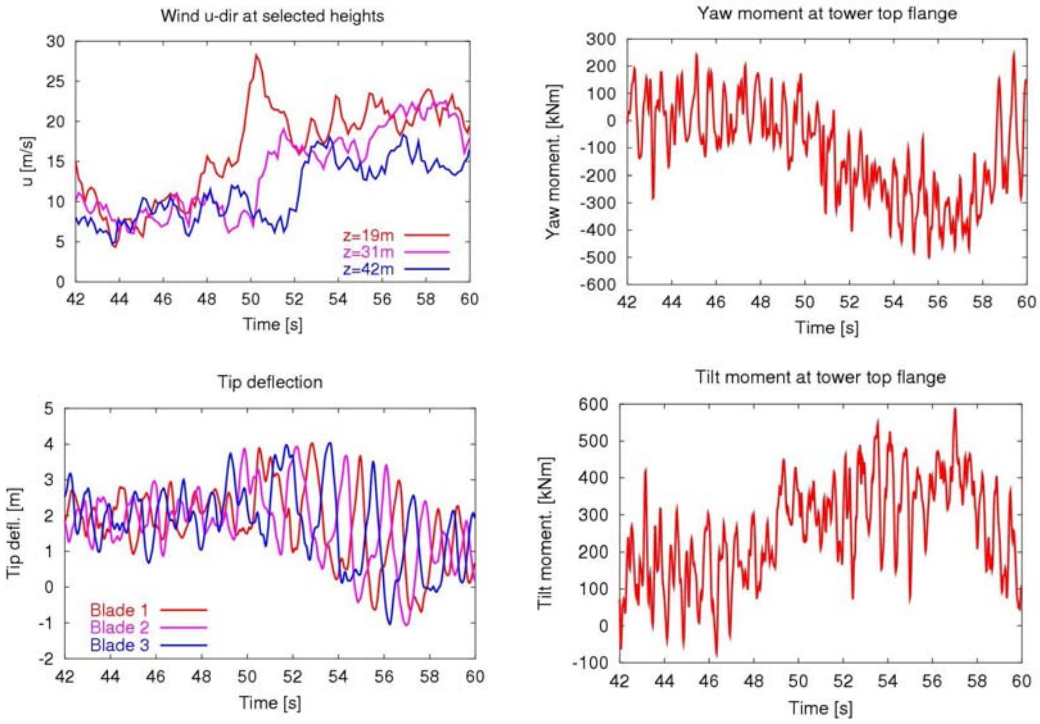

Figure 6-5. Structural loads at gust realization 1 – a severe gust in the lower part of the rotor strikes at time=48s. Large blade deflection as well as rotor structural loading loads occur.

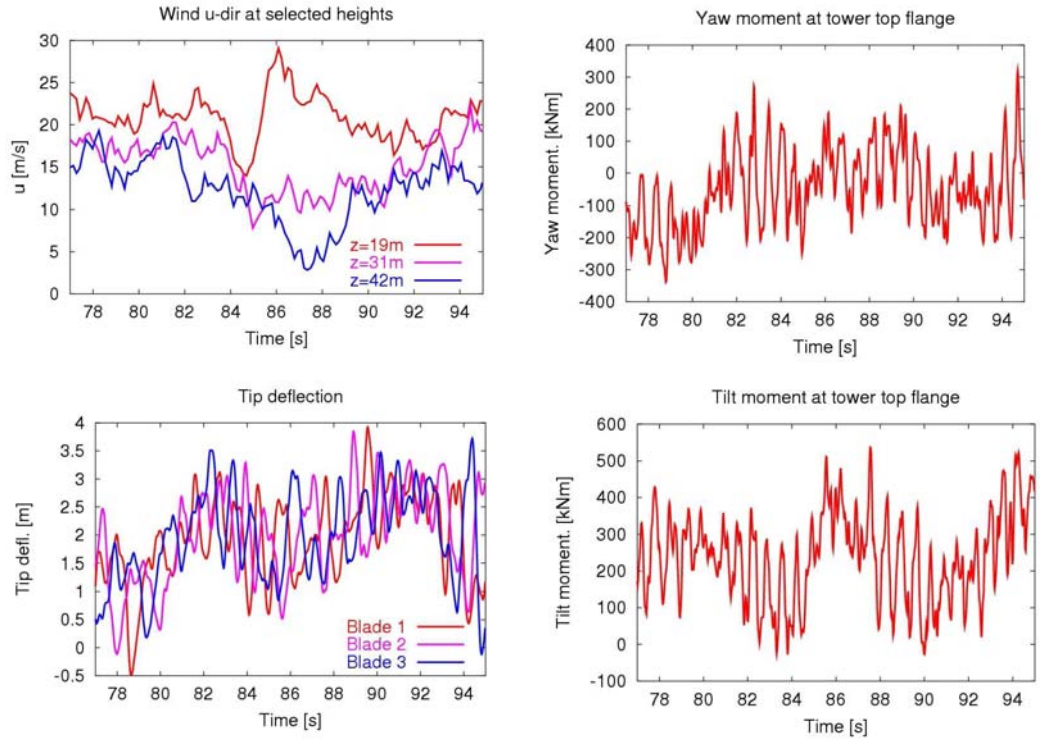

Figure 6-6. Structural loads associated with gust realization 2. Large loads and deflections are seen, but with a slightly changed appearance than for realization 1.

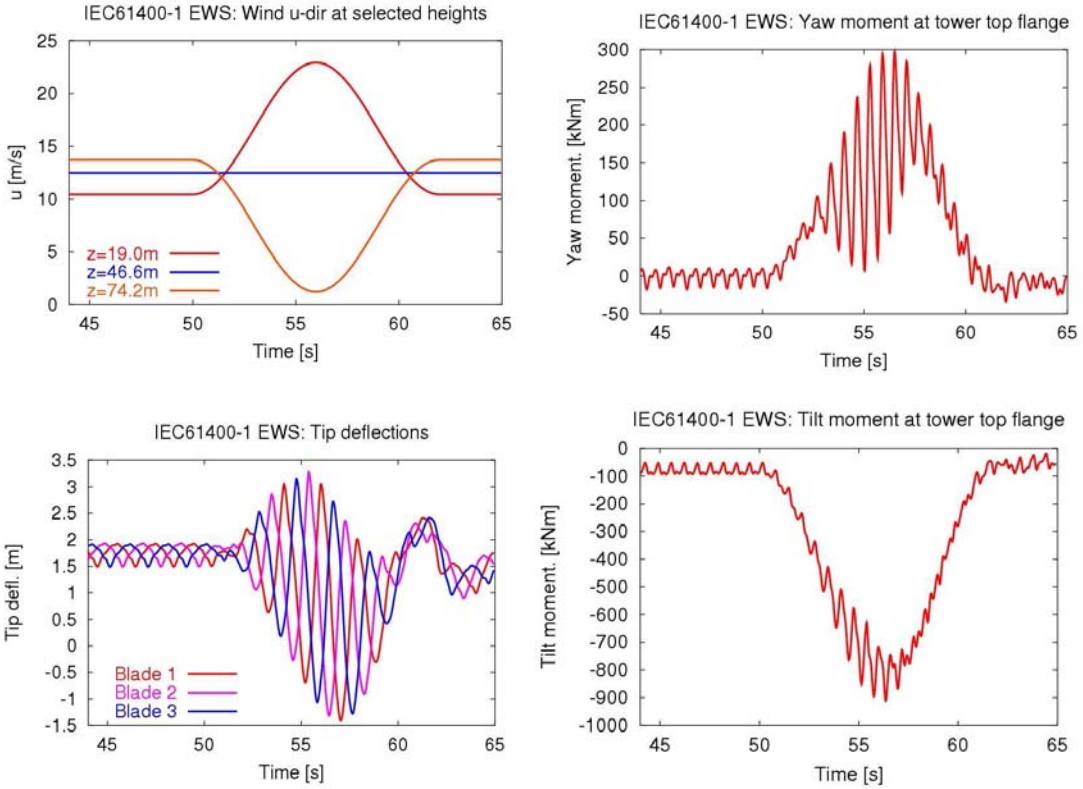

Figure 6-7. Extreme vertical wind shear from IEC61400-1 and corresponding loads for selected sensors.

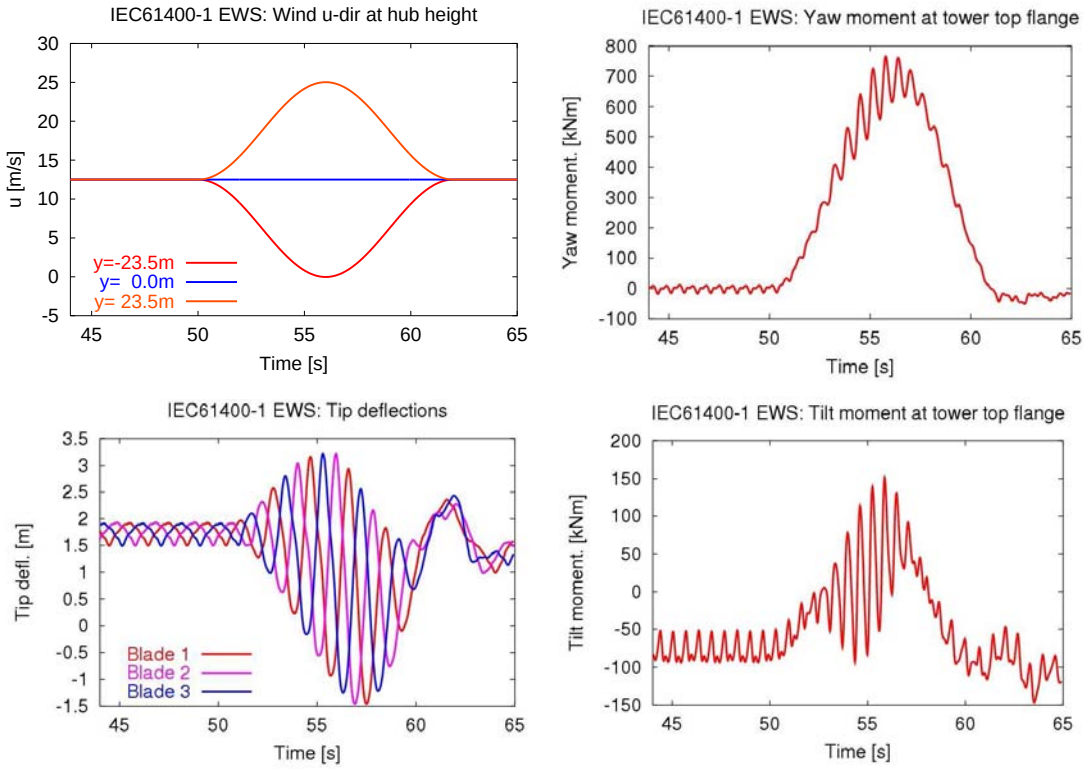

Figure 6-8. Extreme horizontal wind shear from IEC61400-1 and corresponding loads for selected

6.2 The statistical distribution of turbulence driven one point velocity extremes

A statistical model of the extreme value distribution of the amplitude of a one point wind speed increase is presented

As demonstrated in the previous section site specific determination of gust amplitudes might be of crucial importance. The present section describes a statistical model of the extreme value distribution of the amplitude of the simplest possible gust event – a one point wind speed increase. The model has been reported in more detail in [10] and was presented at the EUROMECH colloquium 464b [11].

Preludium

The statistical distribution of extreme wind speed excursions above a mean level, for a specified recurrence period, is of crucial importance in relation to design of wind sensitive structures. This is particularly true for wind turbine structures.

Assuming the stochastic (wind speed) process to be Gaussian, Cartwright and Longuet-Higgens [12] derived an *asymptotic* expression for the distribution of the *largest excursion* from the mean level during an arbitrary recurrence period. From its inception, this celebrated expression has been widely used in wind engineering as well as in off-shore engineering - often through the peak factor, which equals the mean of the Cartwright/Longuet-Higgens asymptotic distribution.

However, investigations of full scale wind speed time series, recorded in the atmospheric boundary layer, has revealed that the *Gaussian assumption* is inadequate for wind speed events associated with *large* excursions from the mean [3], [13], [14]. Such extreme turbulence excursions seem to occur significantly more frequent than predicted

according to the Gaussian assumption, which may under-estimate the probability of large turbulence excursions by more than one decade. This obviously has unfortunate consequences for the applicability of the Cartwright - Lounguet-Higgens asymptotic extreme distribution in the description of extreme turbulence excursions. Another related problem with the Cartwright - Longuet-Higgens expression, associated with description of extreme wind speed events in the atmospheric boundary layer, is, that many investigations of full-scale wind speed gusts (e.g. [15], [16], [17]) have shown, that the observed occurrences of these are excellently described by the Gumbel EV1 distribution. This distribution differs from the asymptotic Cartwright - Longuet-Higgens distribution.

Model

The basic idea behind the present model is, in analogy with Cartwright - Longuet-Higgens, to derive an *asymptotic* expression for the distribution of the *largest excursion* from the mean level during an arbitrary recurrence period, however based on a "mother" distribution, different from the Gaussian distribution, which reflects the observed Exponential-like behaviour for *large* wind speed excursions. This is achieved on the expense of an acceptable distribution fit in the data population regime of small to medium excursions which, however, for an extreme investigation is considered unimportant. Thus, contrary to previous attempts [13], [14] to present a unifying approach describing the entire data range from small to extreme excursions, the present approach is dedicated extreme events only.

More specifically, we postulate the following *conjecture*: Given a Gaussian fit of the total population of velocity fluctuations, the tails of this fit can better approximate the measured data if, in this range, a square root variable transformation is performed in the probability density function (PDF). Thus, replacing the velocity variable with a constant times the square root of the (absolute value of the) velocity variable in the Gaussian fit, and thus essentially replacing the Gaussian fit in this data range with a Gamma fit, will result in a much better fit in the upper range of turbulence velocity excursions. However, at the same time the proposed variable transformation will spoil the nice Gaussian agreement for small and moderate excursions. Therefore, the Gaussian approximation should be retained for small and moderate velocity excursions, whereas the proposed Gamma fit should be used for large excursions only, and consequently should be considered an "asymptotic" distribution.

The focus in the present analysis is on extreme events, and it is therefore appropriate to introduce the proposed transformation in this context. Let us first introduce a (stationary) Gaussian stochastic wind speed process U(z,t) *as*

$$U(z,t) = \overline{U}(z) + u(z,t)\,, \tag{6-1}$$

where an upper bar denotes the mean value operator, *z* denotes the altitude above terrain, and *t* is the time co-ordinate. The small to medium scale turbulence excursions are assumed Gaussian. To capture the extreme excursions, we introduce the variable *v(t)*, given by the monotone and memoryless (time independent) transformation defined by

$$v = g(u) = \frac{C(z)}{\sigma_u}\, sign(u)\, u^2\,;\; C(z) > 0\ , \tag{6-2}$$

with the inverse transformation

$$u = g^{-1}(v) = \sqrt{\frac{\sigma_u}{C(z)}}\, sign(v)\sqrt{|v|} \;;\; C(z) > 0 \;, \qquad (6\text{-}3)$$

where σ_u is the standard deviation of the *total* data population. Note, that with the definition of the transformation expressed in (6-2) and (6-3), the constant *C(z)* is dimensionless. Formulated in terms of the Gaussian PDF, f_u, the PDF of the transformed variable, f_v, is expressed as

$$f_v(v) = \frac{\sqrt{\sigma_u}}{2\sqrt{C(z)}\sqrt{|v|}}\, f_u\left(\sqrt{\frac{\sigma_u}{C(z)}}\, sign(v)\sqrt{|v|}\right) = \frac{1}{2\sqrt{2\pi C(z)\sigma_u}\,\sqrt{|v|}}\, Exp\left(-\frac{|v|}{2C(z)\sigma_u}\right). \qquad (6\text{-}4)$$

The resulting PDF for the transformed variable, *v*, is recognized as a (double-sided) Gamma distribution with shape parameter 1/2. Note, that the Gamma distribution has a singularity at the point defined by *v* = 0, which is, however, without practical relevance for the present application, as we are concerned with modelling of the distribution tails of a wind speed fluctuation population (where *v* is large and thus different from zero).

As the introduced transformation, *g*, is monotone, every local extreme in the *u*-process, ξ, is transformed into a local extreme in the *v*-process. Thus, the number of local extremes (and their position on the time-axis) is unaltered by the performed transformation. Furthermore, due to the symmetry of the transformation, the mean value of the transformed processes is zero like the mean value of the original processes. The philosophy is now the following: Let us perform an asymptotic analysis of the stochastic process in the *v*-domain analogues to the one performed by Cartwright - Longuet-Higgens in the Gaussian case. This is performed by first transforming from the *v*-domain to the *u*-domain. In the *u*-domain, the process is Gaussian, and the analysis performed by Cartwright - Longuet-Higgens thus applies. The derived asymptotic probability density function for the largest maxima, during a time span *T*, is given in terms of velocities normalized with σ_u , η_m, as [12], [17]

$$f_{max}(\eta_m) = \eta_m\, Exp\left\{-e^{-\frac{1}{2}\eta_m^2 + ln(T\upsilon)}\right\} e^{-\frac{1}{2}\eta_m^2 + ln(T\upsilon)} \;, \qquad (6\text{-}5)$$

where υ is the zero-upcrossing frequency multiplied by 2π. Note, that (6-5) is a slight reformulation of the expression given in [12], performed in order to highlight similarities as well as differences between (6-5) and an EV1 type PDF.

The final step is now to transform this asymptotic result from the *u*-domain to the *v*-domain. Denoting *normalised* local extremes in the *v*-domain by

$$\zeta = \frac{C(z)\, sign(\xi)\xi^2}{\sigma_u^2} \;, \qquad (6\text{-}6)$$

we finally obtain the requested asymptotic distribution for the largest normalized maxima during the time span *T*, ζ_m, as

$$f_{max\zeta}(\zeta_m) = \frac{f_{max}\left(\frac{1}{\sqrt{C(z)}}\, sign(\zeta_m)\sqrt{|\zeta_m|}\right)}{2\sqrt{C(z)}\sqrt{|\zeta_m|}} = \frac{1}{2C(z)}\, Exp\left\{-e^{-\frac{1}{2C(z)}|\zeta_m| + ln(T\upsilon)}\right\} e^{-\frac{1}{2C(z)}|\zeta_m| + ln(T\upsilon)} \;. \qquad (6\text{-}7)$$

The asymptotic probability density function expressed in equation (6-7) is seen to be of the EV1 type, which is consistent with the finding from several experimental studies

[15], [16], [17]. For this type of Gumbel distribution, the mean, E(ζm), and root mean square, σ(ζm), is known and given as [18]

$$E(\zeta_m) = 2C(z)(\gamma + ln(\upsilon T)), \qquad (6\text{-}8)$$

and

$$\sigma(\zeta_m) = \pi C(z)\sqrt{\frac{2}{3}}, \qquad (6\text{-}9)$$

where γ denotes the Euler constant (≈ 0.5772). The root mean square is seen to be independent of the time span considered, contrary to the asymptotic PDF described by Cartwright - Longuet-Higgens, and the present asymptotic extreme value distribution thus doesn't narrow with increasing time span. The mode, $m(\zeta_m)$, is obtained by solving the equation

$$\frac{d}{d\zeta_m} f_{max\zeta}(\zeta_m)\Big|_{\zeta_m = m(\zeta_m)} = 0. \qquad (6\text{-}10)$$

The mean, the standard deviation and the mode of a normalized variable are expressed with the statistical model

We find

$$m(\zeta_m) = 2C(z)\, ln(\upsilon T). \qquad (6\text{-}11)$$

Equations (6-8), (6-9) and (6-11) express the mean, standard deviation and mode of a *normalised* variable. The associated physical quantities are obtained simply by multiplying the right hand side of these expressions by the standard deviation of the process, σ_u.

What remains now is to determine the transformation constant, $C(z)$, such that the best possible agreement between the upper tails of measured PDF's and the proposed asymptotic fit is obtained. This is addressed in the next section.

Calibration of the transformation constant

The constant, $C(z)$, entering the proposed variable transformation is "calibrated" to obtain the best possible distribution fit for the upper range of turbulence velocity excursions for available measurements from extensive measuring campaigns, representing three different terrain types – offshore/coastal, flat homogeneous terrain and hilly scrub terrain. The measured data series have initially been de-trended, and to improve statistics we determine the PDF of the measured wind speed fluctuations based on normalised wind speed fluctuations given by

$$\tilde{u} = \frac{u}{U}. \qquad (6\text{-}12)$$

Investigations performed in [3] indicate that this is a valid procedure.

The standard deviation of the normalised variable, $\sigma_{\tilde{u}}$, thus relates to the standard deviation of the physical variable, σ_u, as

$$\sigma_{\tilde{u}} = \frac{\sigma_u}{U}. \qquad (6\text{-}13)$$

Introducing

$$\tilde{v} = \frac{v}{U}, \qquad (6\text{-}14)$$

it is easily verified that the transformations given by expressions (6-2) and (6-3) also apply between quantities normalised according to expressions (6-12) – (6-14). The PDF of the transformed normalised variable is subsequently obtained from the Gaussian PDF of the original normalised variable, expressed by

$$g_{\tilde{u}}(\tilde{u}) = \frac{1}{\sigma_{\tilde{u}}\sqrt{2\pi}} Exp\left(-\frac{\tilde{u}^2}{2\sigma_{\tilde{u}}^2}\right), \qquad (6\text{-}15)$$

by introducing the variable transformations, defined in (6-2) and (6-3), between normalised variables. The resulting PDF is given by

$$g_{\tilde{v}}(\tilde{v}; C(z)) = \frac{1}{2\sqrt{2\pi C(z)\sigma_{\tilde{u}}}\sqrt{|\tilde{v}|}} Exp\left(-\frac{|\tilde{v}|}{2C(z)\sigma_{\tilde{u}}}\right). \qquad (6\text{-}16)$$

The calibration of the transformation constant is performed against a large number of independent data sets originating from “Database on Wind Characteristics” [19]. The details of these appear from Table 6-3 (note, that all sectors with mast effects present have been excluded).

We perform a least square fit of the transformed PDF, expressed by equation (6-16), to the measured PDF in the upper tail regime - here defined as the part of the distribution where

$$\tilde{v} > 3\sigma_{\tilde{u}} . \qquad (6\text{-}17)$$

Denoting the measured PDF by $g_m(*)$, the transformation constant, $C(z)$, is thus determined by minimizing the functional defined by

$$\Pi(C(z)) = \int_{3\sigma_{\tilde{u}}}^{\infty} d\tilde{v}\,(g_{\tilde{v}}(\tilde{v}; C(z)) - g_m(\tilde{v}))^2 . \qquad (6\text{-}18)$$

A common feature of the C-values resulting from the performed data fit, is a moderate, but significant, dependence with height, which may be interpreted as the effect of the gradually increasing size of the biggest turbulence eddies contributing to extreme events, as the distance to the blocking ground increases. These eddies will of course also contribute to the standard deviation in general, which is already included in the expressions, even for constant C. However, these big eddies will be relatively more important as drivers for the very extreme events than as contributors to the overall turbulence standard deviation, thus leading to the monotone dependence of C with the altitude. An example of the fit obtained for the upper distribution tail regime is shown in Figure 6-9. The estimated maximum likelihood fits of $C(z)$ for the investigated terrain classes are shown in Figure 6-10.

Table 6-3 The data sets used in the calibration of the model to the 3 selected terrain categories.

Site	Type of site	Obs. height [m]	No. hours	Scan freq. [Hz]	C
Gedser rev	Offshore	45	385	5	0.357
Rødsand	Offshore	45	390	5	0.325
Horns Rev	Offshore	50	629	20	0.387
Nasudden	Coastal; flat	40	1122	1	0.340
Nasudden	Coastal; flat	98	1548	1	0.401
Nasudden	Coastal; flat	118	1589	1	0.459
Skipheya	Coastal; roling hills	11	5200	0.85	0.307
Skipheya	Coastal; roling hills	21	5737	0.85	0.339
Skipheya	Coastal; roling hills	41	6408	0.85	0.373
Skipheya	Coastal; roling hills	72	4446	0.85	0.386
Skipheya	Coastal; roling hills	101	3904	0.85	0.434
Skipheya	Coastal; roling hills	101	3550	0.85	0.463
Cabauw	Flat, hom. (Pastoral)	40	377	2	0.297
Cabauw	Flat, hom. (Pastoral)	80	421	2	0.313
Cabauw	Flat, hom. (Pastoral)	140	440	2	0.331
Cabauw	Flat, hom. (Pastoral)	200	404	2	0.358
Oak Creek (M1)	Hill, scrub	79	1671	8	0.437
Oak Creek (M2)	Hill, scrub	10	2593	8	0.366
Oak Creek (M2)	Hill, scrub	50	1916	8	0.404
Oak Creek (M2)	Hill, scrub	79	3210	8	0.426

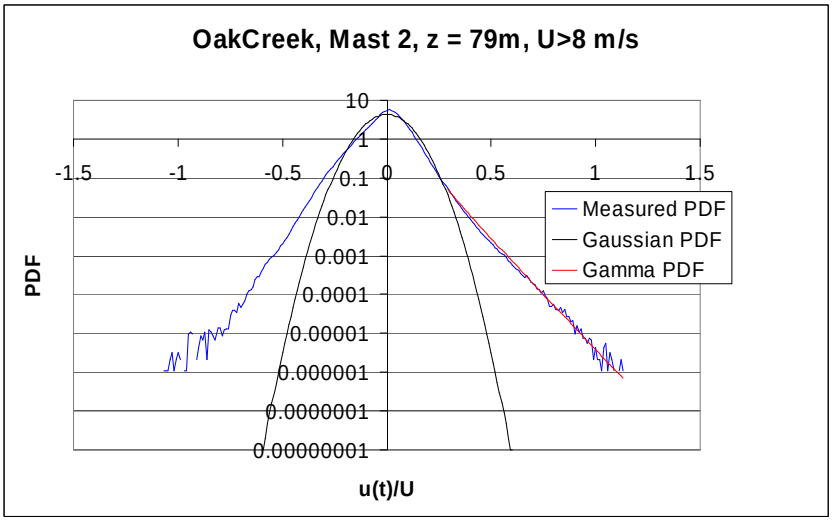

Figure 6-9. Gaussian and Gamma fits compared for the large excursion regime.

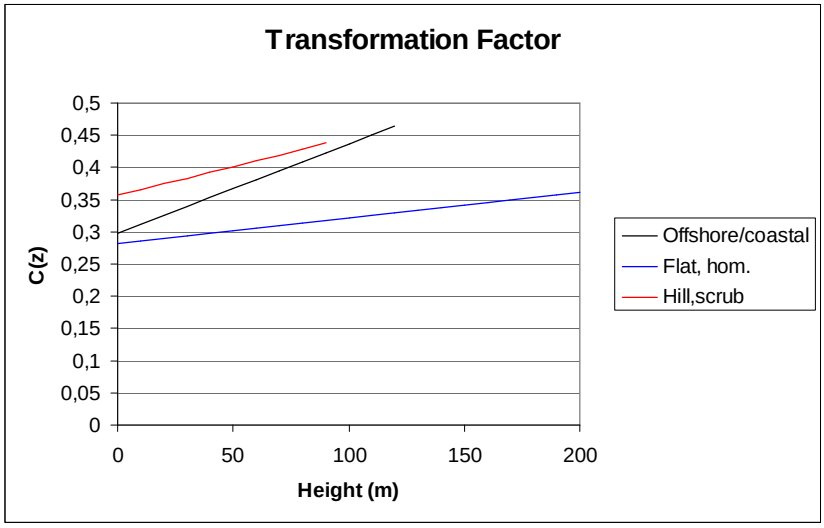

Figure 6-10. The estimated dependence of the transformation parameter C with height for three terrain types.

Based on a big amount of measure-ments the statistical model was calibrated to handle offshore, flat and hilly terrain

The estimated parameters defining the linear dependence,

$$C(z) = a\,z + b\,, \qquad (6\text{-}19)$$

of the transformation constant with height above terrain, obtained for the three investigated terrain categories, are given in Table 6-4.

Table 6-4 Estimated parameters defining the transformation constant for various terrains.

Terrain type	a	B
Offshore/coastal	0.0014	0.2972
Flat, homogenous	0.0004	0.2820
Hilly, scrub	0.0009	0.3566

6.3 Conclusions

We have demonstrated the capability of a very versatile theory for simulation of Gaussian *turbulence driven* gust events by emulating a violent shear gust event from a complex site in Spain. The generated stochastic gust event has been demonstrated to exhibit the requested characteristics imposed by defining a number of constraints in the turbulence simulation.

The resulting turbulence field has subsequently been imposed on a fictitious but realistic pitch regulated turbine with variable speed using the aerolastic code HAWC2. Selected structural responses parameters have been analyzed and compared with the analogue parameters resulting from replacement of the stochastic gust event with the extreme shear gust load case from IEC 64100.

Significant differences are seen in the character of the response from the stochastic gust event and the deterministic one

The comparison shows (as expected) *significant differences in the character* of these responses. The blade deflection caused by the stochastic gust event exceeds the similar deflection caused by the deterministic code specified load case. The peak tilt loading, caused by the deterministic loading, exceeds the peak tilt loading arising from the stochastic loading, but the *dynamic character of the stochastic response is much more violent*. The peak loading of the stochastic shear gust is, however, likely to increase if turbulence constraints could be specified in upper rotor plane (where measurements do not exists at the investigated site). The yaw loading, arising from the stochastic *vertical* shear event, exceeds the yaw loading caused by the deterministic vertical extreme shear both concerning the peak performance and the violence of the dynamic performance.

The extreme shear event specified in the IEC 64100 code refers to a recurrence period of *50 years*, whereas the measured shear event is obtained from a *3 month* recording period only. It is therefore expected that if an extreme value analysis is performed on the available measured shear gust events, the resulting estimate, corresponding to a 50 year period, will display a substantial increase in the shear gust magnitudes, and thus potentially be much more critical for the turbine than the directly recorded event. This obviously calls for statistical models for direct determination of site specific gust amplitudes.

From a fatigue point of view, the stochastic gust events are observed to be much more severe than the deterministic extreme shear event defined in the IEC 64100, and for wind turbines, positioned at locations where negative shear gusts occur frequently (mountainous terrain), the fatigue contribution arising from such events may be significant.

An asymptotic model for the PDF of the largest excursion from the mean level has been derived for a stochastic wind speed process

From a control design point of view, the stochastic gust events present challenges for the control system that may not be experienced and/or modeled properly, using the code specified deterministic extreme events from IEC 64100. Therefore, these stochastic gust events are most suitable for test of wind turbine control systems, and necessary for optimal design of load reducing controllers, cf. [20], [21], and [22].

As a follow up on the need for rational statistical models of gust amplitudes, an *asymptotic* model for the PDF of the *largest excursion* from the mean level, during an arbitrary recurrence period, has been derived for a stochastic wind speed process driven by atmospheric turbulence. The model requires only a few, easily accessible, input parameters, and it accounts for variation of the magnitude of large excursions with height above terrain. It has been calibrated against a huge number of full-scale wind speed time series measurements for application in three of the most common terrain categories.

If required, the derived conditional extreme value distribution can be convoluted with the probability density function of the turbulence standard deviation (for various mean wind speeds) to yield the overall extreme probability density function of turbulence driven short term wind excursion events.

Finally, it should be noted that the methodology presented is easily adjusted to apply also in other types of turbulence driven extreme events. Such extensions are planned in a forth coming EFP project (*A simulation platform for generation of wind loads applicable for aeroelastic computations)*.

6.4 References

[1] Wind Turbine Generator Systems: part 1, Safety Requirements.

[2] J.B. Dragt and W. Bierbooms (1996): Modeling of Extreme Gusts for Design Calculations. European Union Wind Energy Conference, pp. 842-845, Göteborg, May 20-24.

[3] Nielsen, M., Larsen, G.C., Mann, J., Ott, S., Hansen, K.S. and Pedersen, B.J. (2003). Wind Simulation for Extreme and Fatigue Loads. Risø-R-1437(EN).

[4] Larsen, G.C., Ott, S., Nielsen, M. and Mann, J.. Simulation of Extreme Gaussian Gust Events. In preparation.

[5] Mann, J.; Larsen, G.C.; Larsen, T.J. (2006). Towards more realistic extreme load predictions. In: Proceedings (online). 2006 European Wind Energy Conference and Exhibition, Athens (GR), 27 Feb - 2 Mar 2006. (European Wind Energy Association, Brussels, 2006) 8 p.

[6] Mann, J. (1994). The Spatial Structure of Neutral Atmospheric Surface-Layer Turbulence. J. of Fluid Mech., 273, 141-168.

[7] Mann, J. (1998). Wind field simulation. Prob. Eng. Mech. **13**, 269-282.

[8] Petersen, J.T. (1990). Kinematically Nonlinear Finite Element Model of a Horizontal Axis Wind Turbine. Part 1: Mathematical Model and Results. PhD thesis, Risø National Laboratory.

[9] Larsen, T.J., Hansen, A., and Buhl, T. (2004). Aeroelastic effects of large blade deflections for wind turbines. Proceedings of the special topic conference "The Science of making Torque from Wind". Delft University of Technology. The Netherlands.

[10] G.C. Larsen and K.S. Hansen. The statistical distribution of turbulence driven wind speed velocity extremes – Cartwright/Longuet-Higgins revised. To appear.

[11] Larsen, G.C.; Hansen, K.S. (2005). The statistical distribution of turbulence driven velocity extremes in the atmospheric boundary layer - Cartwright/Longuet-Higgins revised. In: [Program and abstracts]. EUROMECH colloquium 464b: Wind energy. International colloquium on fluid mechanics and mechanics of wind energy conversion, Oldenburg (DE), 4-7 Oct., p. 28.

[12] D.E. Cartwright and M. S. Longuet-Higgins (1956). The statistical distribution of the maxima of a random function, Proc. Royal Soc. London Ser. A 237, pp. 212-232.

[13] F. Boettcher, C. Renner, H.-P. Waldl, and J. Peinke (2003). On the statistics of Wind Gusts. Boundary Layer Meteorology, **108**, 163-173.

[14] H.A. Panofsky and J.A. Dutton (1984). Atmospheric Turbulence - Models and Methods for Engineering Applications. John Wiley & Sons.

[15] G.C. Larsen, K.S. Hansen and B.J. Pedersen (2002). Constrained simulation of critical wind speed gusts by means of wavelets, 2002 Global Windpower Conference and Exhibition, France.

[16] G.C. Larsen and K.S. Hansen (2001). Statistics of Off Shore Wind Speed Gusts, EWEC'01, Copenhagen, Denmark, 2-6 July.

[17] G.C. Larsen and K.S. Hansen (2004). Statistical model of extreme shear. Special topic conference: The science of making torque from wind, Delft (NL), 19-21 April, Delft University of Technology, pp. 433-444.

[18] Gumbel, E.J.(1966). Statistics of Extremes. Columbia University Express.

[19] "Database on Wind characteristics". www.winddata.com.

[20] Larsen, T.J., Madsen, H.A., Thomsen, K. (2005). Active load reduction using individual pitch, based on local blade flow measurements. Wind. Energ.; **8**:67-80

[21] Caselitz, P. Kleinkauf, W., Krüger, T., Petschenka, J., Reichardt, M., Störzel, K. (1997). Reduction of fatigue loads on wind energy converters by advanced control methods. Proceeding of the IWEA International Conference, Dublin; pp. 555-558.

[22] Bossanyi, E.A. Individual blade pitch control for load reduction (2003). Wind Energ.; **6**:119-128.

7 Influence of soil and water on tower dynamics

Torben J. Larsen, Helge A. Madsen, Anders M. Hansen, Kenneth Thomsen

7.1 Introduction

During the last years more focus on the offshore wind turbines have forced the development of aeroelastic codes to include effects of tower foundation loading from waves, ice etc. This was also the case for the original aero elastic code HAWC [1],[2] developed at Risø, but due to limitations in the code at that time some simplifications were done which is now the key point for the present investigation. The old simplifications were that the water acceleration and velocity in the Morison's equation were neglecting the relative movement of the tower and that the soil suspension was modeled by extending the tower to an equivalent depth where it was fixed at the bottom. Now a completely new aero elastic code HAWC2 has been developed at Risø, which among other improvements makes further extensions of the model easy and straightforward.

An offshore monopile foundation is analysed with the HAWC2 aeroelastic code

The multibody formulation used in the HAWC2 code is very generally formulated which means that it can handle any structural object (body) as well as large rotations between the bodies and their associated nonlinear effects. This means e.g. that complex foundation types as very flexible monopile foundations, tripod structures and floating support structures can be simulated in the code. In the present investigation the monopile foundation will be considered. It is possible to apply non-linear springs and dampers on the structure, which are used for soil properties. In the hydrodynamic module of the code the hydrodynamic forces are calculated using Morison's equation. The investigations performed are based on time simulations of a typical 2MW turbine during operation and standstill. Parameter variations are carried out to investigate the influence of wind speed, water depth, monopile length and diameter.

The results presented in this chapter have previously been published in proceedings of the conference Copenhagen Offshore Wind 2005 [3].

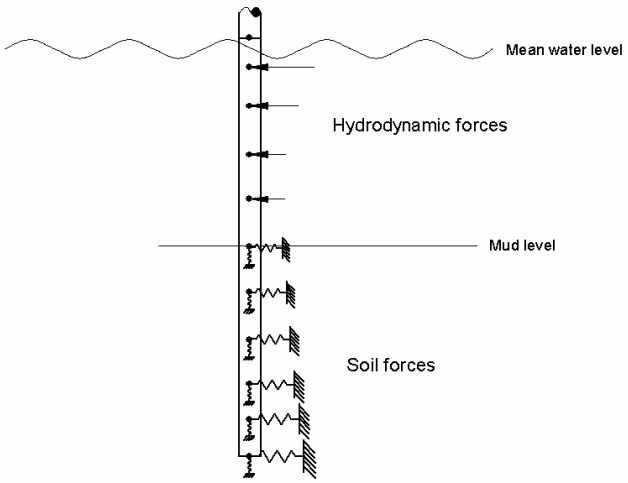

Figure 7-1: Illustration of external forces on the monopile foundation. The soil forces are illustrated as linear springs even though they are highly nonlinear. The stiffness increases with soil depth.

7.2 Symbols

A	[m^2]	Cross sectional area
C_m	[-]	Coefficient of inertia
C_d	[-]	Coefficient of drag
C_{1-3}	[-]	Coefficients as function of friction angle
D	[m^2]	Cross sectional diameter
G_0	[Pa]	Initial shear modulus of the soil
K	[Pa/m]	Initial modulus of sub grade reaction
U	[m/s]	Velocity of water
U_{rel}	[m/s]	Relative velocity between water and pile
$\dot{U}_{rel}$	[m/s^2]	Relative acceleration between water and pile
V	[m^2]	Volume of construction pr. length
V_R	[m^2]	Reference volume of construction pr. length
P_u	[N/m]	Ultimate lateral soil strength
Y	[m]	Lateral deflection
X	[m]	Height above mud level
Z_{IF}	[-]	Radius of influenced soil zone divided by pile radius
ρ	[kg/m^3]	Density of water
γ'	[N/m^3]	Submerged unit weight of soil

7.3 Model

HAWC2 is extended to include hydrodynamic loading and soil support

The present investigation was made by use of Risø's newly developed aero elastic code, HAWC2. HAWC2 is primarily aimed for time simulations of the aero elastic response of wind turbines. However, the model is continuously extended to fulfill the demands for new features e.g. wind turbines mounted offshore. For the present investigation HAWC2 is extended to include hydrodynamic loading and soil support as well.

The main parts of HAWC2 are the structural part, the external loading part, and the control part. The structural model of HAWC2 is based on flexible multibody dynamics [4]. The wind turbine structure is modeled by a number of bodies, e.g. a tower body or a shaft body, and these bodies are then connected by a set of constraint equations. The flexibility of the structure is modeled by Timoshenko beam elements with 6 degrees of freedom for each node. Normally, the tower and shaft are modeled by a single body each, while the blades are divided into several bodies in order to capture geometric non-linear effects [5]. Further, all inertia forces and external loading are based on the deformed shape of the structure. The nonlinear equations are solved in time domain using the Newmark beta and modified Newton-Raphson method.

The aerodynamic part is based on the BEM principle with input data from Cl, Cd, Cm, alpha curves. The calculation points on the blades are positioned independently of the structural node/element discretization to provide an optimal distribution of these points, which normally differs from the optimal structural discretization. The spacing between aerodynamic calculation points are closest at the tip and root where the large aerodynamic force gradients normally occur. The BEM method used for calculation of the induced velocities is modified to handle dynamic inflow, large yaw errors. The specific implementation method is described in [6]. The dynamic stall models by Beddoes and Leishmann [7] and Stig Øye [8] are implemented.

Control of the wind turbine is handled by external DLLs so that the actual control algorithm needs not be linked directly with the code. However, HAWC2 includes standard control DLL algorithms for common ways of controlling wind turbines. For controlling the rotational speed and the pitch position two methods exist. One is by specifying constraints for the current body which acts as a bearing (free to rotate in one direction) and controlling the position, speed and acceleration by servo forces. The other method is by specifying constraints that fix the body to a neighboring body and control

the angle between the bodies by external demands. Both methods provide full update of all inertia forces etc. within the iterations.

The soil and hydrodynamic loads are applied as external distributed loads on the structure varying in time and through the internal iterations.

The hydrodynamic forces are based on Morison's equation for drag and inertia loads as written in (7-1)

$$dF_{hydro} = \rho V\dot{U} + \rho V_r C_m \dot{U}_{rel} + \tfrac{1}{2}\rho D C_d U_{rel}\left|U_{rel}\right| \quad (7\text{-}1)$$

Since Morison's equation includes a large force component in phase with the acceleration, the added mass part, the solver in HAWC2 had some troubles with the iterations at each time step. The reason for this is that the external forces are implemented as explicit formulations exactly as in (7-1). Since the added mass of the water is app. 10 times larger than the steel of the monopile the solver will not predict the accelerations well. This problem which also occurs when external forces acts as large stiffness (e.g. for the soil stiffness) was solved by adding the equivalent mass and stiffness to the prediction part of the solver.

The soil spring forces are as for the hydrodynamic forces modeled as external forces which enables the possibility of using the exact non-linear spring characteristic as stated in the standards for pile foundations [9],[10]. Since the current monopile for the investigation is mounted in sand, the lateral spring stiffness p-y curves are based on the expression in (7-2). Such a p-y curve is normally intended for static analysis of the pile. This means that information regarding hysteresis effects and effects of how the p-y curve shall be when soil previously has been submitted to large deflections are lacking. These effects that could very well increase the structural damping on the construction have therefore not been considered.

$$p(y) = AP_u \tanh\left(y\,k\frac{X}{AP_u} \right) \quad (7\text{-}2)$$

P_u is the ultimate lateral resistance of soil based on the expression (7-3). The p-y characteristics for several soil depths are illustrated in Figure 7-2 .

$$P_u = \min\begin{cases} (C_1 X + C_2 D)\gamma' X \\ C_3 D\gamma' X \end{cases} \quad (7\text{-}3)$$

In the present investigation the coefficients chosen are for sand with a friction angle of 40°: C_1=4.5, C_2=4.2, C_3=100, γ'=2000N/m^3

The vertical spring stiffness is based on a t-z curve (7-4) assuming small vertical shears. This stiffness causes the total turbine to move app. 2 mm downwards due to gravity.

$$t(z) = \frac{2G_0}{D\ln(Z_{IF})} z \quad (7\text{-}4)$$

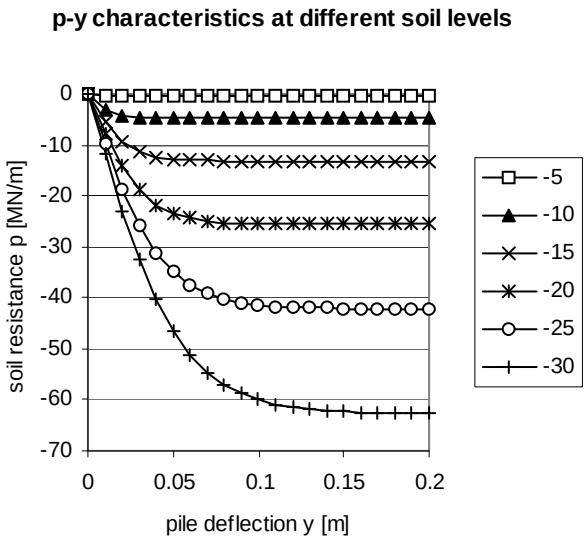

Figure 7-2: Relation between soil resistance and lateral deflection for a monopile in sand.

7.4 Investigation of soil support

The foundation is modeled using a soil support model and not fixing the lowest part of the tower which is a normal simplification

Normally the soil support is not taken into consideration or simply taken into consideration by extending the tower down to an equivalent fix point. This is clearly a simplification of the boundary conditions from the soil, which is mainly due to limitations in the aero elastic codes so far.

The monopile chosen for the investigation is a pile with a diameter of 4.5m, wall thickness of 0.05m and a length of 24 m in the soil. The deflection shape of tower and monopile when the tower is submitted to a lateral force of 1MN at the tower top can be seen in Figure 7-4. The more correct way of modeling results in a deflection shape of the pile where the lower part moves in counter phase with the tower motion.

The size of the pile is essential for its support of the wind turbine above. The natural frequencies of the tower were excited at standstill by applying a lateral external random force on the tower top. In Figure 3 the influence of pile diameter and length can be seen. A constant wall thickness of 0.05m is used. It is seen that the frequency increases with increasing diameter and pile length. When the pile is longer than a certain length, which in this case is app. 20m, the frequency is no longer affected by further pile elongation and only the pile diameter influences the frequency.

The first natural frequency of the tower is 0.347Hz when the tower is fixed at the mud level. This is decreased to 0.328 Hz for a pile of 24m and a diameter of 4.5m. However if we assumed the pile to be fixed at –11m, which is the zero crossing for the static deflection in Figure 7-4 and skips the soil forces the natural frequency decreases to 0.336 Hz. However if the equivalent fix point was –16m, which corresponds to the vertical tangent the tower frequency decreases to 0.323Hz. A rule of thumb could be that the equivalent fix point for a monopile is between the static zero cross point and the vertical tangent. For this turbine the equivalent fix point seems to be in –14m. This approach also seems to give good results regarding the higher order tower vibrations for the turbine which is shown in Figure 7-6 when the turbine operates at 8m/s.

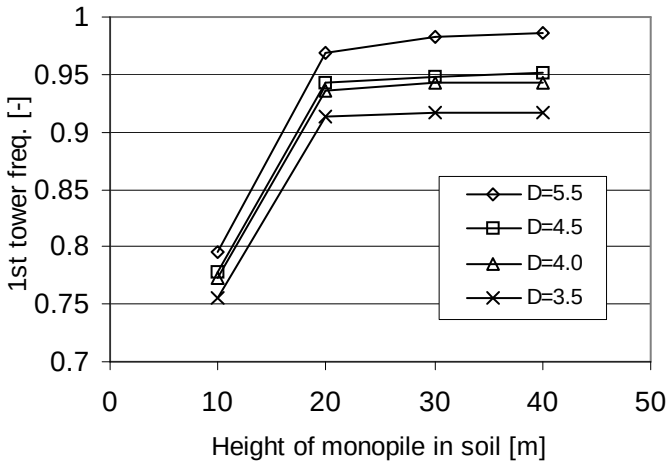

Figure 7-3: Influence on first tower frequency by changes in monopile lenght and diameter. The frequency is normalized with the tower frequency for a tower fixed at the mudlevel.

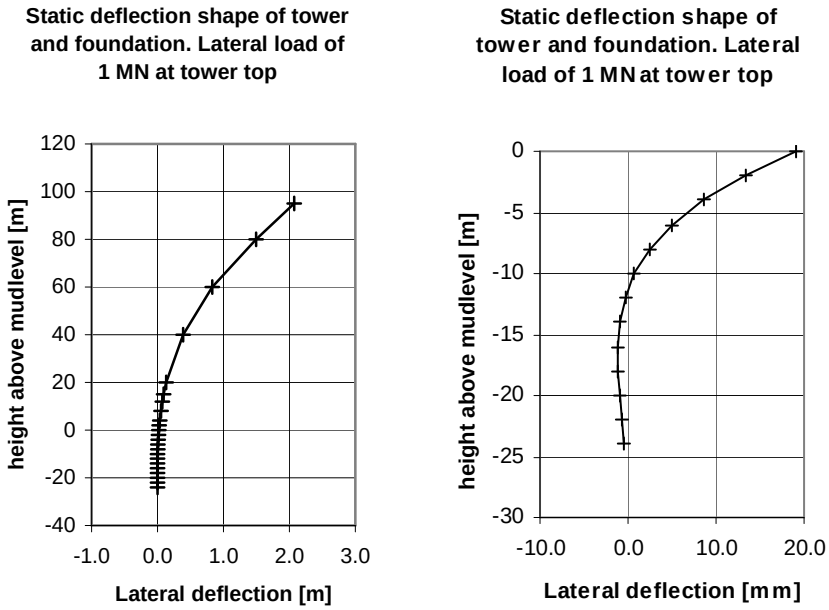

Figure 7-4: Static deflection of tower and monopile when applying a single static lateral force on the tower top.

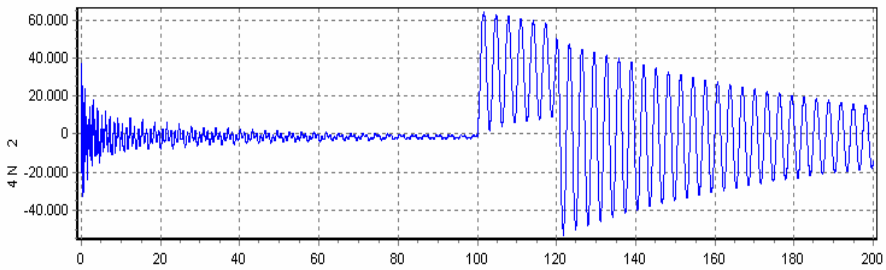

Figure 7-5: Tower activated by a constant force in axial direction in the period from 100 – 120 sec.

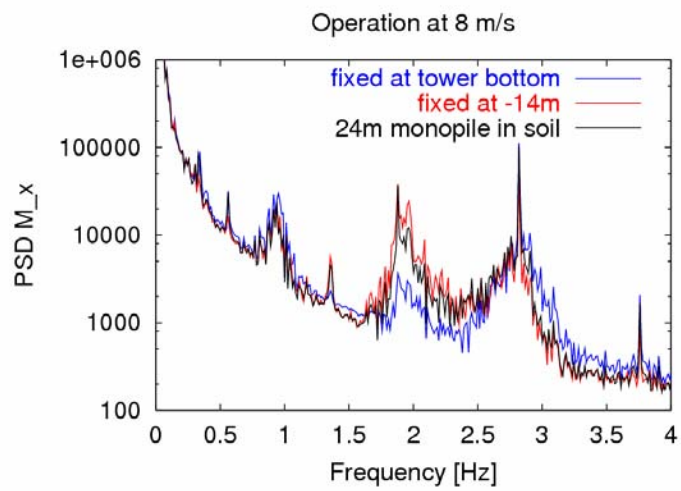

Figure 7-6: PSD of tower moment at midlevel of tower for three configurations of tower suspension. The monopile in soil and the tower fixed at an equivalent depth of 14 m are almost identical, where the configuration with the tower fixed at mudlevel has less energy at 2 Hz.

7.5 Investigation of influence of water level on tower frequency and damping at standstill

The influence of the water level on the tower frequency showed a slight decrease in eigenfre-quency with increasing water level

The influence of water level on tower frequency and damping was tested during standstill conditions with no aerodynamic forces. A constant force activated the tower motion over a short period from 100 to 120 sec., Figure 7-5. On basis of the tower response after time 120 sec. the first tower eigenfrequency and damping was derived for four water depth; 0m, 10m, 20 m and 30 m. The result is summarized in Table 1 and it is seen that the eigenfrequency is slightly decreased with increasing water level and the damping is almost unchanged. To see the influence of changes in damping due to external water velocity (current) a parameter variation has been carried out at 30m water depth. The increase in damping as a result of increasing water velocity is shown in Table 2.

Table 5: Influence of tower depth on 1st tower frequency and damping during standstill.

Water depth	*1st tower eigenfrequncy [Hz]*	*Damping Logarithmic decrement*
0	0.3207	0.0454
10	0.3205	0.0454
20	0.3199	0.0455
30	0.3177	0.0463

Table 6: Influence of current on 1st tower frequency at 30m water depth.

Current [m/s]	*Damping log. Decr.*
0	0.0463
0.5	0.0496
1.0	0.0541
1.5	0.0587
2.0	0.0632
5.0	0.0909

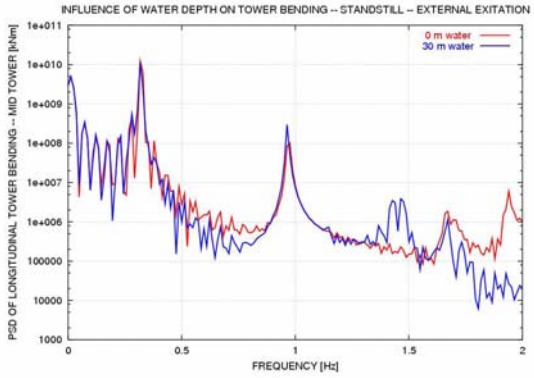

Figure 7-7: Spectrum of tower bending moment on the mid part of the part at standstill without aerodynamic forces. Tower activated as above with a constant force over a short period.

The investigation of influence of water depth on tower frequency is further illustrated by the power spectrum of the tower bending moment on the mid part of the tower, Figure 7. The second tower bending frequency is just below 1 Hz and it is seen that this frequency decreases slightly, Figure 7. On the other hand there are two other frequencies in the range from 1.5 to 2.0 Hz, which are changed down to about 1.4 and 1.7 Hz, respectively. In these vibrations the 2nd tower bending mode is dominant in combination with edgewise blade bending.

7.6 Influence of water level of dynamic tower response during operation

Next the influence of water depth on tower dynamics during operation was investigated.

A simulation at turbulent wind at 8 m/s has been run,

Figure 7-8. A considerable less high frequent energy in the PSD spectrum is seen above 1.7 Hz for the 30 m water depth, however with a slight increase at 1.5 Hz. This is due to the change in frequencies as discussed above on basis of Figure 7, and a minor, but still present, damping effect from the water.

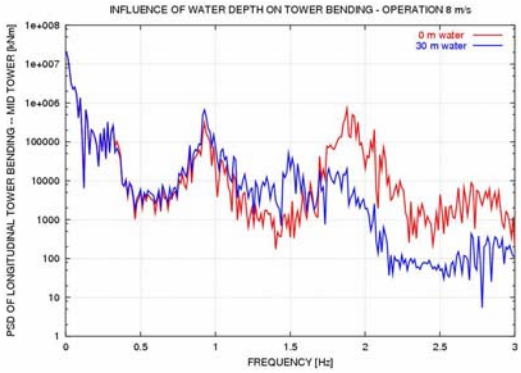

Figure 7-8: PSD of tower bending moment on the mid part of the tower during operation at 8 m/s.

7.7 Results and discussion

In this chapter the newly developed code HAWC2 was used to investigate some stability effects regarding the boundary conditions of a monopile foundation that is lacking in other codes. Nonlinear soil spring forces were applied as well as hydrodynamic forces based on Morison's equation. The problems that arose with the numerical solver due to the explicit formulation of soil and hydrodynamic forces were solved by adding equivalent mass and stiffness to the predictor part of the solver.

The boundary conditions of the soil and the flexibility of the pile mainly reduce the first tower frequency with app. 5%. A parameter variation showed that when the pile length exceeds a certain minimum length any further elongation does not contribute to increased stiffness. It is verified that even though the soil support has a very nonlinear characteristic it is fully justifiable to simplify the model by modeling the monopile down to an equivalent depth where it is fully fixed. The equivalent fix point for aero elastic codes that does not include soil springs was right between the static zero crossing depth and the vertical deflection tangent of the static deflection shape of the pile submitted to a lateral load in the tower top.

The influence of the hydrodynamics showed only minor influence on the tower frequency and damping

The influence of hydrodynamics showed only minor influence on the tower frequency and damping. The tendency was however that the 1st tower frequencies decreased slightly for increasing water depth. The influence of the water mainly appeared in a frequency change of some high order frequencies where the 2nd tower bending mode dominates, which was reduced from 1.7 and 2.0 Hz to 1.4 and 1.7 Hz, respectively.

The results of the investigations are that the hydrodynamics only affects the mode shapes where the 2nd tower bending mode is present by decreasing the natural frequency. The effective damping on the 1st tower vibration is not affected by the hydrodynamics, but slightly on the higher frequencies. An increase in external water velocity, which occurs due to current or waves, leads to a noticeable increase in damping.

The calculation time for a 600s time simulation with 38 nodes on the tower, 4 nodes on the shaft and 12 nodes on each blade is app. 1000s, which corresponds to a time ratio of 1.7 more than real time. The processor used is a 2.8GHz Pentium 4.

7.8 References

[1] Petersen, J.T. Kinematically Nonlinear Finite Element Model of a Horizontal Axis Wind Turbine. Part 1: Mathematical Model and Results. PhD thesis, Risø National Laboratory, 1990

[2] Petersen, J.T. The Aeroelastic code HAWC – Model and Comparisons. In 28th IEA Experts Meeting: 'State of the art of aeroelastic codes'. DTU, Lyngby, 1996

[3] Larsen, T.J., Madsen, H.A., Hansen, A.M., Thomsen, K. Investigation of stability effects of an offshore wind turbine using the new aeroelastic code HAWC2. In proceedings of Copenhagen Offshore Wind 2005.

[4] Shabana, A. A., Dynamics of multibody systems. Cambridge University Press, University of Illinois at Chicago, 2nd edition, 1998

[5] Larsen, T.J., Hansen, A., Buhl, T. Aeroelastic effects of large blade deflections for wind turbines. Proceedings of the special topic conference "The Science of making Torque from Wind". Delft university of technology. The Netherlands 2004.

[6] Madsen, H.A. Aerodynamic modeling in the aeroelastic codes HAWC and HAWC2. Presented at the IEA Annex XI and Annex XIX meeting held in Pamplona, Spain on May 25-26, 2005

[7] Hansen, M.H., Gaunaa, M., Madsen, H.A. A Beddoes-Leishman type dynamic stall model in state-space and indicial formulations. Risø-R-1354(EN), Risoe National Laboratory June 2004.

[8] Øye, S. Dynamic stall simulated as time lag of separation. In proceedings of 4th IEA Symposium on the Aerodynamics of Wind Turbines. Jan 1991, Rome, Italy.

[9] Offshore standard DNV-OS-J101 Design of offshore wind turbine structures. June 2004.

[10] Guidelines for Design of Wind Turbines 2nd edition. Det Norske Veritas and Risø National Laboratory. 2002. ISBN 87-550-2870-5

8 Torsional properties of large wind turbine blades

Anders M. Hansen, Kim Branner, Peter Berring, Henrik W. Knudsen, Mark Capellaro

The motivation for initiating this work is the concern that flutter instabilities may occur as the wind turbine blades become larger. Due to the increased size of the blades, the torsional eigenfrequency becomes lower and the torsional mode may couple with some of the lower bending modes. Also, it is expected that in case of flutter instability, the amplitude of the flutter vibration will increase rapidly and may result in ultimate failure of the wind turbine.

Previous work has shown limited correlation between the torsional response obtained by numerical structural models and measurements, cf. [1], [2]. In [1] the response of two numerical models was compared, one obtained by a FEM model using shell elements, and another obtained by a FEM model using beam elements. In general, the comparison of the torsional response between the two models showed poor correlation, both regarding the torsional eigenfrequency and eigenmode, and regarding the torsional contents of flapwise and edgewise modes. The latter is significant for the aerodynamic damping properties of wind turbine modes and thus for the calculation of fatigue loads. In [2] the response of the numerical model from [1] was compared with measured modal response and also here the correlation related to torsional response was limited, especially for the higher modes, including the 1st torsional mode.

Torsion is believed to be important, but the tools for analyzing it are unreliable.

In summary, the torsional properties of blades are believed to be important and at the same time the methods to calculate the response are unreliable. This calls for further attention on this subject.

The aim of the work initiated in the present milestone is to implement and verify numerical models with special attention to torsional behavior. The two numerical models that are dealt with are a detailed FEM model based on shell elements, and a FEM model based on an anisotropic beam element which includes the structural couplings introduced in the blade sections when layers of composite materials are used for the structural design. The beam element model is intended to be implemented into the aeroelastic code HAWC2.

Validation of the numerical models is done by comparison of the response with static and dynamic experiments performed on a part of a full-scale blade provided by Vestas Wind Systems A/S. This work is done by master students from DTU as part of their master theses. However, since the finalization dates of the master projects are due later than the finalization date of the present project, what is reported herein is merely a status of the milestone more than a report of finalized work.

8.1 Description of Master Projects

During this project, two master projects were initiated and one of these was preceded by a pre-project. Both projects are expected to end in August 2006 and are done by students from DTU with Assistant Professor Christian Berggren as supervisor. In the following sub-sections the contents of the projects are outlined.

Torsional Performance of Large Wind Turbine Blades. Pre-project and Master Project by Peter Berring and Henrik W. Knudsen

The primary aim is to investigate methods, both experimental and numerical, to calculate stiffness properties including the bend-twist coupling. Furthermore, the aim is to design and build a test rig for doing such experiments on a particular blade part. Finally, the project aims to study how well finite element models predict the torsional behavior of a blade.

The contents of the project is outlined below:

- Make a detailed FE-model (shell elements) of the blade section.
- Design and building of a test rig for experimental investigations.
- Numerical determination of the stiffness matrix for blade sections, which can be used as input to the HAWC2 code. This is done by analyzing static load cases.
- Numerical analysis of the blade section's dynamic properties (modal analysis) including torsion mode shapes and their couplings to bending.
- Experimental determination of the bending stiffness parameter, the torsional stiffness parameter and the bend-twist coupling parameter.
- Comparison of experimental and numerical results.
- Suggest guidelines for reliable determination of torsion stiffness and bend-twist couplings using FEM.

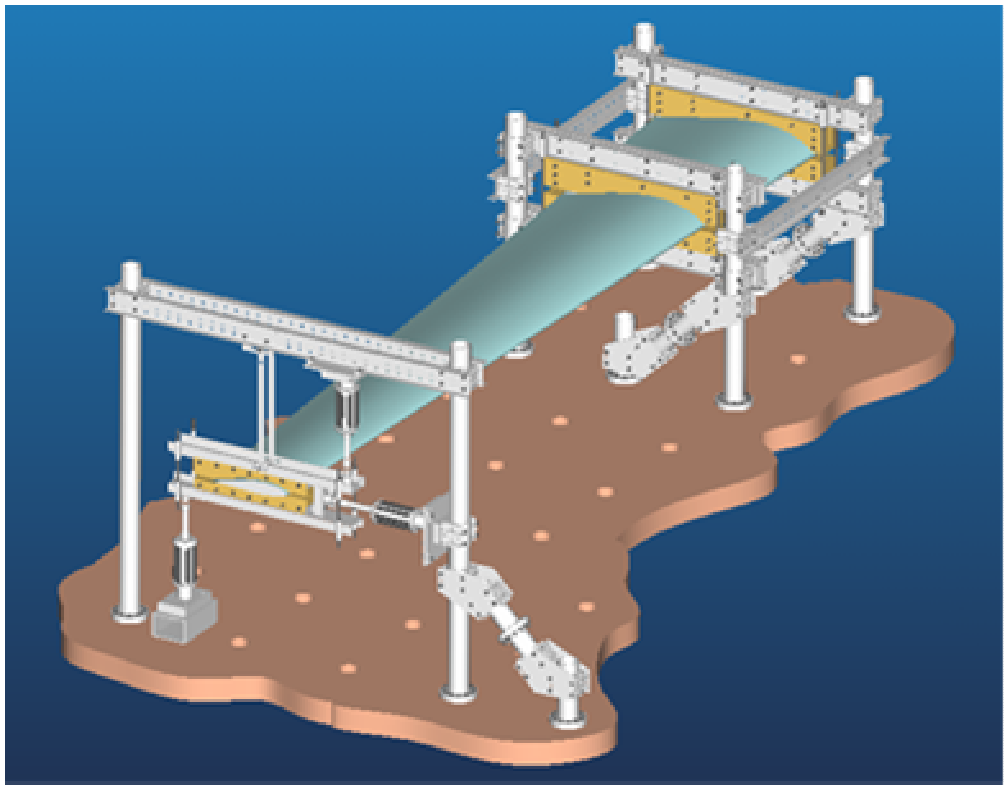

Figure 8-1: Drawing of the test rig designed during the pre-project.

Figure 8-2: Blade positioned in test rig ready for dynamic testing.

The status of the project (June 2006) is that the pre-project is finalized which resulted in the test rig design shown in Figure 8-1. The as-built test rig is shown in Figure 8-2. Further, the first series of tests have been performed with success and the results are presently being analyzed. All of the intended sub-tasks in the list above are expected to be covered within the project period. Conclusions are not available yet, but will be reported later.

Application of Bend-Twist Couplings in Design of Large Wind Turbine Blades. Master project by Mark Capellaro

The primary aim is to investigate to what extent the bend-twist coupling can be used to reduce loads on wind turbine blades. The aim is also to investigate the limits of realistic bend-twist couplings achievable in current design practice.

The contents of this master project is outlined below:

- Development of FEM model of a blade with designed bend-twist coupling.
- Numerical analysis of the blade section's dynamic properties (modal analysis) including torsion mode shapes and their couplings to bending.
- Full-scale blade testing in existing test rig, with special emphasis on vibration measurements (modal analysis).
- Validation of FEM model against full-scale experimental testing.
- Development of a beam model for a simplified code that will allow bend-twist couplings to be simulated.
- Estimation of possible load reduction and validation of beam model against FEM results for an optimized adaptive blade taking advantage of bend-twist couplings.

The status of the project (June 2006) is that the experimental modal analysis has been performed. All of the intended sub-tasks in the list above are expected to be covered within the project period, and conclusions will be reported later.

8.2 Application of an anisotropic beam model

This section gives a description of an anisotropic beam element intended to be implemented into HAWC2. It differs significantly from the beam element presently implemented, and a description of the difference is given below. Further, 2 examples of the use of the new element is given.

Description of the new element

The beam element presently used in the aeroelastic code HAWC2 is a prismatic Timoshenko element for which the properties of the element is defined through the following constitutive relations

The old constitutive matrix...

$$\begin{Bmatrix} F_x \\ F_y \\ F_z \\ M_x \\ M_y \\ M_z \end{Bmatrix} = \begin{bmatrix} EA & 0 & 0 & 0 & 0 & 0 \\ 0 & k_yGA & 0 & 0 & 0 & 0 \\ 0 & 0 & k_zGA & 0 & 0 & 0 \\ 0 & 0 & 0 & GI_x & 0 & 0 \\ 0 & 0 & 0 & 0 & EI_z & 0 \\ 0 & 0 & 0 & 0 & 0 & EI_y \end{bmatrix} \begin{Bmatrix} \gamma_x \\ \gamma_y \\ \gamma_z \\ \kappa_x \\ \kappa_y \\ \kappa_z \end{Bmatrix}$$

The diagonal matrix above is the constitutive matrix for the beam section which gives the relation between sectional forces and moments, and the corresponding beam strains. The diagonal terms that enter this particular constitutive matrix are the axial stiffness, EA, the shear stiffnesses, k_yGA and k_zGA, the torsional stiffness, GI_x, and the bending stiffnesses, EI_z and EI_y. Actually, in the derivation of the stiffness and mass matrix, corrections are made in order to account for the location of the shear center which indirectly results in addition of a few off-diagonal terms in the constitutive matrix, however, still leaving the most of the off-diagonal terms zero.

In order to describe the sectional properties in a more general way a fully populated constitutive matrix is introduced, like the following:

...and the new.

$$\begin{Bmatrix} F_x \\ F_y \\ F_z \\ M_x \\ M_y \\ M_z \end{Bmatrix} = \begin{bmatrix} S_{11} & S_{12} & S_{13} & S_{14} & S_{15} & S_{16} \\ S_{12} & S_{22} & S_{23} & S_{24} & S_{25} & S_{26} \\ S_{13} & S_{23} & S_{33} & S_{34} & S_{35} & S_{36} \\ S_{14} & S_{24} & S_{34} & S_{44} & S_{45} & S_{46} \\ S_{15} & S_{25} & S_{35} & S_{45} & S_{55} & S_{56} \\ S_{16} & S_{26} & S_{36} & S_{46} & S_{56} & S_{66} \end{bmatrix} \begin{Bmatrix} \gamma_x \\ \gamma_y \\ \gamma_z \\ \kappa_x \\ \kappa_y \\ \kappa_z \end{Bmatrix}$$

The constitutive matrix depends on the material lay-up and the geometry of the blade section, and the question is how to obtain it for selected beam sections of the blade. For the present analysis it was chosen to use the Variational Asymptotic Beam Section analysis software, VABS, which is available for research purposes, cf. [3].

VABS provides the new constitutive matrix

The solution to a general 3D elastic problem can be obtained by minimizing the sum of internal and external elastic energy with respect to the state variables describing the deformation of the structure. In short, VABS separates the state variables along the beam axis from the state variables in the sectional plane and performs the energy minimization with respect to the sectional state variables. This is in essence the collapse of a 3D elastic problem into a 1D problem. The state variables in the sectional plane describe the deflection of the section points, both in-plane and out-of-plane. Together with the 1D solution the strains can be obtained in all points of the beam section, and thus the stresses in the section can be obtained as a post-processing capability.

Besides the constitutive matrix, VABS also provides the sectional mass properties, and from these two matrices the derivation of the stiffness and mass matrices can be made. The derivation and validation of the implementation of the stiffness and mass matrices are given in [4].

Example: Effect of boundary conditions in the experiment

This example was made to investigate the importance of the boundary conditions in the dynamic experiments described in Section 8.1. The blade which is analyzed is approximately 8 meters long and it is supported at two locations along the blade, one support at the root and one support approximately 2 meters from the root. Three different sets of boundary conditions were applied at the two supports. These were defined as:

1. "fix": All 6 DOFs fixed (3 displacements and 3 rotations) at the outermost support
2. "ss1": Fixed in displacement and in rotation around the beam axis at both supports, and fixed rotations around the bending axes at the innermost support
3. "ss2": Similar to "ss1" except that the rotations around the bending axes are free at the innermost support

The three plots in Figure 8-3 show the flap, edge, and torsional displacement for the 1st flapwise modal shape for all three boundary condition sets. Table 7 shows the normalized eigenfrequencies of the first four eigenmodes for the different boundary condition sets. The frequencies are normalized by the frequencies of the fixed set of boundary conditions (set 1). Clearly, the "ss1" and "ss2" sets of boundary conditions are significantly lower than for the "fix" set, except for the 1st torsional mode. Also, it is clear from the plots in Figure 8-3 that the effect of the boundary conditions is significant. The boundary conditions that are the most realistic are the "ss2" set and this example shows that the blade cannot be considered clamped at the outermost support.

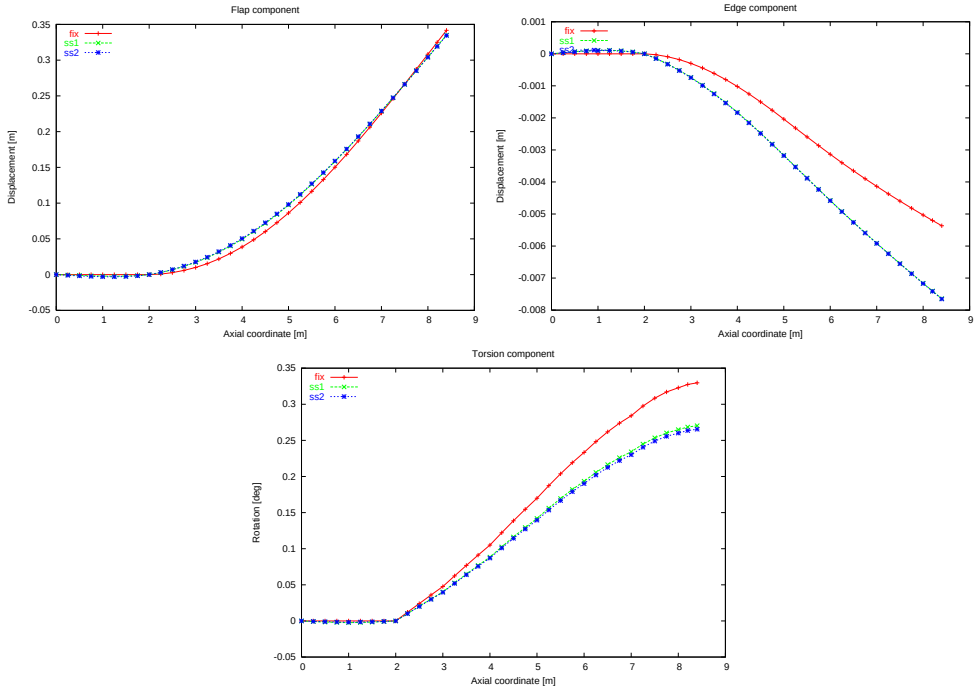

Figure 8-3: Flap, edge, and torsional deflection for the 1st flapwise bending mode for three different boundary conditions.

Table 7: Ratio between eigenfrequencies for the three boundary condition sets for the first four eigenmodes.

	1st Flap	1st Edge	2nd Flap	1st Torsion
Ss1/fix	0.897	0.840	0.910	0.999
Ss2/fix	0.888	0.837	0.903	0.999

Example: Effect of fibre orientation

This example demonstrates the effect of fibre orientation on the mode shapes of a blade. In Figure 8-4, the flap, edge, and torsional contents of the 1st flapwise mode shape is shown for 3 different lay-ups. The lay-ups differ in orientation of the outermost UD-layer of the sample blade, both on the suction side and the pressure side. The orientation of the layers are 0/0, +15/-15, and -15/+15 degrees, respectively, i.e. the top and bottom layers are rotated in opposite directions.

For the flapwise and the edgewise contents of the mode shape the effect is almost invisible, but for the torsional contents the effect is indeed visible. In the present example the eigenfrequencies for the 3 lay-ups were almost identical. Further, the effect on the higher modes was almost invisible.

The example implies that it might be reasonable to include these material effects in aeroelastic calculations to investigate which load reducing (or increasing) effects can be achieved by aeroelastic tailoring.

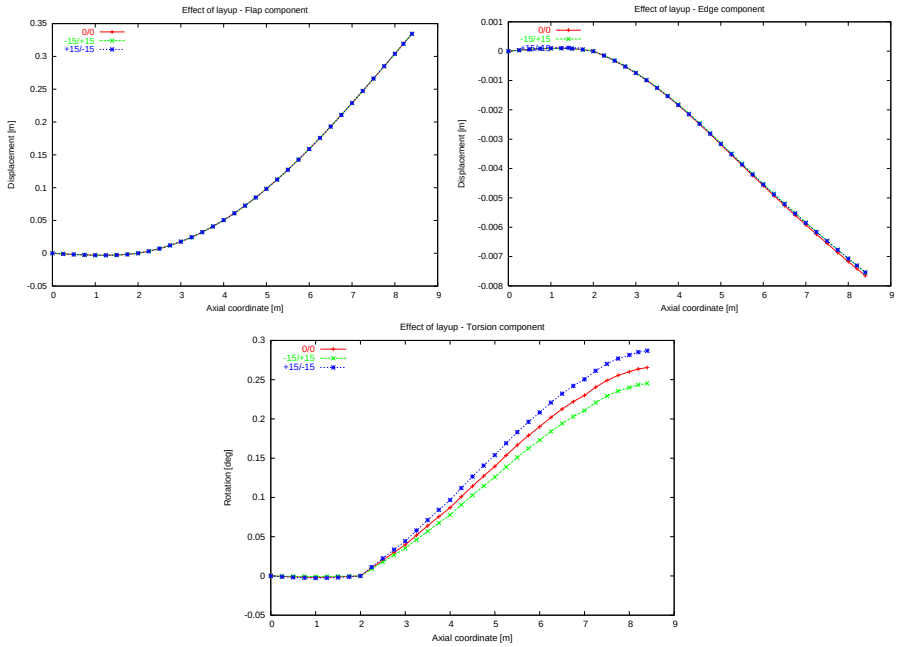

Figure 8-4: Effect of material lay-up.

8.3 Conclusion

The present section has presented the status of the work performed under the milestone related to torsional properties for large wind turbine blades. The work is on-going and the main results will be presented in the continuation of this EFP-project.

During the project a new anisotropic beam element based on the program VABS has been implemented. The validation of the element formulation awaits the finalization of the 2 master projects which were initiated under this milestone. When these master

projects are finalized it is expected that the present work provides an improved model for doing blade response analysis, which has been validated by comparison between experiments (static and dynamic) and a FEM shell model. This provides the basis for giving more confidence in flutter estimation – and aeroelastic stability analyses in general - and the ability to analyze the reduction of fatigue loads by aeroelastic tailoring of future blades. Further, it is expected that guidelines for the use of shell finite elements with special attention to torsional behavior of blades will be addressed.

8.4 References

[1] Helge Aagaard Madsen: ' Forskning i Aeroelasticitet - EFP-98', Risø-R-1129(DA), Risø National Laboratory, August 1999

[2] Gunner C. Larsen et al: ' Modal Analysis of Wind Turbine Blades', Risø-R-1181(EN), Risø National Laboratory, February 2002

[3] Cesnik, C. E. S. and Hodges, D. H.: 'VABS: A New Concept for Composite Rotor Blade Cross-Sectional Modeling', Journal of the American Helicopter Society, vol. 42, no. 1, Jan. 1997, pp. 27 - 38

[4] A.M.Hansen: 'Implementation of anisotropic beam finite element model based on VABS', Risø-R-1558(EN), Risø National Laboratory, to appear

9 Conclusion

In the Energy Research Project ”Program for Research in Applied Aeroelasticity” (EFP2005), Risø National Laboratory (Risø) and the Technical University of Denmark (DTU) have applied and further developed the tools in “the aeroelastic design complex”, which consists of:

- 3D Computational Fluid Dynamics , *EllipSys*, and actuator disc/line models,
- Noise calculations in terms of both empirical models and Computational Aero Acoustics (CAA),
- Airfoil and blade design (HAWTOpt and AIRFOILOpt) with corresponding tests of new airfoil designs in wind tunnel,
- Aeroelastic codes in terms of structural models including wind modelling and aerodynamic models (HAWC og FLEX),
- Aeroelastic stability and control, where linear stability analysis is carried out for the whole wind turbine (HAWCStab).

The main results from the project are:

- Adding a winglet to a wind turbine blade for minimizing the induced drag of the blade, where different winglet configurations were analysed and for a winglet pointed toward the wind, the biggest increase in power was 1.4% with a corresponding increase in thrust of 1.6%. Effects of sweep and cant angles were not accounted for in this analysis.
- Transient wind loads during pitch motion, where the time constants varying along the blade span are determined using the EllipSys3D Navier-Stokes solver and an actuator disc method. Transients in the computations are compared to the NREL/NASA Ames test and reasonably good agreement is seen.
- A general method was developed for the determination of 3D angle of attack for rotating blades from either measurements or numerical computations using CFD.
- A model of the far wake behind wind turbines was developed and forms the basis of a supplementary work on stability of the tip vortices in the far wake behind a wind turbine.
- The investigation of an aerodynamically more efficient blade root region showed that the power efficiency, CP, can locally be increased significantly beyond the Betz limit, but that the global CP for the rotor cannot exceed the Betz limit. Furthermore, a simple correction of the Glauert BEM model to account for the effect from the pressure term from wake rotation has been developed and tested. Finally, when including tip losses and the minimum blade drag coefficient, a maximum rotor CP in the range of 0.51-0.52 was obtained, which is in good agreement with 3D CFD computations that showed a CP around 0.51.
- A new airfoil family with relative thicknesses from t/c=15% to 30% was designed. To design the airfoil family, a 3D design tool was developed to take 3D effects into account such as airfoil compatibility and blade stiffness. Compared to the Risø-B1 family, the aerodynamic characteristics are improved because the characteristics with forced transition at the leading edge are similar, but with free transition the lift-

drag ratio was increased significantly for lift values between 1.0 and 1.6. Comparing the structural characteristics with the Risø-B1 family the new airfoil family is around 5% more stiff around the chord line corresponding to the flap direction for a wind turbine blade and the compatibility between the airfoils improved further.

- Four different airfoils were analyzed to reveal the differences between 2D and 3D Computational Fluid Dynamics. Several mechanisms explaining the discrepancies between the different numerical simulations, and some of the experimental results, have been identified. However, these conclusions cannot in general be applied to all types of airfoils. The two major conclusions of this work are the dependency of computational results to transition modelling, and the ability of 3D DES calculations to realistically simulate the turbulent wake of an airfoil in stall.

- The capability of a versatile theory for simulation of Gaussian turbulence driven gust events was demonstrated by emulating a violent shear gust event from a complex site in Spain. The generated stochastic gust event has been demonstrated to exhibit the requested characteristics imposed by defining a number of constraints in the turbulence simulation. Furthermore, as a follow up on the need for rational statistical models of gust amplitudes, an asymptotic model for the PDF of the largest excursion from the mean level, during an arbitrary recurrence period, has been derived for a stochastic wind speed process driven by atmospheric turbulence. The model requires only a few, easily accessible, input parameters, and it accounts for variation of the magnitude of large excursions with height above terrain. It has been calibrated against a huge number of full-scale wind speed time series measurements for application in three of the most common terrain categories.

- An offshore monopile foundation was investigated using HAWC2. The boundary conditions of the soil and the flexibility of the pile mainly reduce the first tower frequency with app. 5%. A parameter variation showed that when the pile length exceeds a certain minimum length any further elongation does not contribute to increased stiffness. It is verified that even though the soil support has a very nonlinear characteristic, it is fully justifiable to simplify the model by modelling the monopile down to an equivalent depth where it is fully fixed. The influence of hydrodynamics showed only minor influence on the tower frequency and damping. The hydrodynamics only affect the mode shapes where the 2^{nd} tower bending mode is present by decreasing the natural frequency. The effective damping on the 1^{st} tower vibration is not affected by the hydrodynamics, but slightly on the higher frequencies. An increase in external water velocity, which occurs due to current or waves, leads to a noticeable increase in damping.

- A new anisotropic beam element based on the program VABS, which is a program for providing sectional-properties of arbitrary blade sections from geometry and material properties, has been implemented. This provides the basis for giving more confidence in flutter estimation and also the ability to analyze the reduction of fatigue loads by aeroelastic tailoring of future blades.

Furthermore, there has been activity within the development of the aeroelastic design complex in both the short and the long term. Also, investigations not defined by the milestones have been carried out such as, e.g. transient loads during pitch motion, determination of angle of attack for rotating blades and modelling of the far wake behind a wind turbine have been investigated. The list of publications, Chapter 10, shows extensive activity within communication with 6 journal papers, 13 conference papers, 2

reports and 2 lectures. Also, it should be noted that the research environment of the aeroelastic research program is an ideal frame for education. At the moment 4 Ph.D and 4 Master students are affiliated to Risø and 4 Ph.D. and 7 Master students to the DTU. Furthermore, researchers from both Risø and the DTU teach at the Wind Energy Master education and the Danish Academy in Wind Energy (DAWE). Finally, both Risø and the DTU have contributed with a number of basic and specialist courses for wind turbine industry engineers at the Research and Competence Centre for the wind energy sector (HIBAT Wind).

10 Complete list of publications from the project

10.1 Journal papers

Bertagnolio, F., Sørensen, N.N., and Rasmussen, F., "New Insight Into the Flow Around a Wind Turbine Airfoil Section", Journal of Solar Energy Engineering (Transaction of the ASME), Vol.127, pp.214-222, 2005.

G.C. Larsen and K.S. Hansen (To appear). The statistical distribution of turbulence driven wind speed velocity extremes – Cartwright/Longuet-Higgins revised.

Larsen, T.J.; Aagaard Madsen, H.; Thomsen, K., Investigation of stability effects of an offshore wind turbine. The new aeroelastic code HAWC2. Windtech Int. (2006) 2 , 33-35

Larsen, T.J.; Aagaard Madsen, H.; Thomsen, K., Active load reduction using individual pitch, based on local blade flow measurements. Wind Energy (2005) 8 , 67-80

W.Z. Shen, R. Mikkelsen and J. N. Sørensen, "Tip loss correction for Actuator / Navier-Stokes computations". Journal of Solar Energy Engineering, vol. 127, No. 2, pp. 209-213, (2005).

W. Z. Shen, R. Mikkelsen, J. N. Sørensen and C. Bak, "Tip loss corrections for wind turbine computations". Wind Energy, vol. 8, pp. 457-475, (2005).

10.2 Conference papers

Bak, C.; Gaunaa, M.; Antoniou, I., Performance of the Risø-B1 airfoil family for wind turbines (poster). In: [Program and abstracts]. EUROMECH colloquium 464b: Wind energy. International colloquium on fluid mechanics and mechanics of wind energy conversion, Oldenburg (DE), 4-7 Oct 2005. (ForWind, Oldenburg, 2005) p. 76

Bak, C.; Johansen, J.; Andersen, P.B., Three-dimensional corrections of airfoil characteristics based on pressure distributions (paper and poster). In: Proceedings (online). 2006 European Wind Energy Conference and Exhibition, Athens (GR), 27 Feb - 2 Mar 2006. (European Wind Energy Association, Brussels, 2006) 10 p.

J. Johansen, H.Aa Madsen, N.N. Sørensen, and C. Bak “Numerical Investigation of a Wind Turbine Rotor with an aerodynamically redesigned hub-region”, EWEC-2006, Athens, 27. feb. -2. March, 2006.

J. Johansen and N.N. Sørensen, “Aerodynamic investigation of Winglets on Wind Turbine Blades using CFD”, IEA Annex II/XX Joint meeting, Kiel, Germany, 25-26. April, 2006.

Larsen, G.C.; Hansen, K.S. (2005). The statistical distribution of turbulence driven velocity extremes in the atmospheric boundary layer - Cartwright/Longuet-Higgins revised. In: [Program and abstracts]. EUROMECH colloquium 464b: Wind energy. International colloquium on fluid mechanics and mechanics of wind energy conversion, Oldenburg (DE), 4-7 Oct., p. 28.

Larsen, T.J.; Madsen, H.Aa.; Hansen, A.M.; Thomsen, K., Investigation of stability effects of an offshore wind turbine using the new aeroelastic code HAWC2. In: Proceedings (CD-ROM). Copenhagen offshore wind conference 2005, Copenhagen (DK), 25-28 Sep 2005. (Copenhagen Offshore Wind, Copenhagen, 2005) 6 p.

Larsen, T.J.; Hansen, A.M., Influence of blade pitch loads by large blade deflections and pitch actuator dynamics using the new aeroelastic code HAWC2 (poster). In: Proceedings (online). 2006 European Wind Energy Conference and Exhibition, Athens (GR), 27 Feb - 2 Mar 2006. (European Wind Energy Association, Brussels, 2006) 5 p.

Madsen, H.Aa., Aerodynamic modelling in the aeroelastic codes HAWC and HAWC2. IEA Joint Action Committee on aerodynamics, Annex XI and 20. Aero experts meeting, Pamplona (ES), 25-26 May 2005. Unpublished.

Madsen, H.Aa.; Johansen, J.; Bak, C.; Sørensen, N.N., An investigation of inboard rotor/blade aerodynamics and its influence on blade design. Sandia blade workshop, Alberquerque (US), 18-19 Apr 2006. Unpublished.

Mann, J.; Larsen, G.C.; Larsen, T.J. (2006). Towards more realistic extreme load predictions. In: Proceedings (online). 2006 European Wind Energy Conference and Exhibition, Athens (GR), 27 Feb - 2 Mar 2006. (European Wind Energy Association, Brussels, 2006) 8 p.

Mikkelsen R. and Øye S. Towards the Optimal Loaded Actuator Disc. IEA Symp. on the 'Aerodynamics of wind turbines', Kiel, Germany, 2006, to appear.

Sørensen, N.N.; Madsen, H.Aa., Modelling of transient wind turbine loads during pitch motion (paper and poster). In: Proceedings (online). 2006 European Wind Energy Conference and Exhibition, Athens (GR), 27 Feb - 2 Mar 2006. (European Wind Energy Association, Brussels, 2006) 10 p.

Sørensen, N.N., Rotor computations using a 'Steady State' moving mesh. IEA Joint Action Committee on aerodynamics, Annex XI and 20. Aero experts meeting, Pamplona (ES), 25-26 May 2005. Unpublished.

10.3 Reports

Bertagnolio, F., Sørensen, N.N., and Johansen, J., "Profile Catalogue for Airfoil Sections Based on 3D Computations", Technical Report, Risø National Laboratory, Roskilde, Denmark (to be published).

J. Johansen and N.N. Sørensen "Aerodynamic investigation of Winglets on Wind Turbine Blades using CFD" Risø-R-1543(EN), Risø National Laboratory, Roskilde, February 2006.

10.4 Lectures

Rasmussen, F., Aeroelasticitet. Vinddag 2005, Dansk Forskningskonsortium for Vindenergi, Risø (DK), 23 Aug 2005. Unpublished.

Sørensen, N.N., CFD activities at Risø Wind Energy Department. Marine - CFD workshop, Trondheim (NO), 16 Jun 2005. Unpublished.

Risø's research is aimed at solving concrete problems in the society.

Research targets are set through continuous dialogue with business, the political system and researchers.

The effects of our research are sustainable energy supply and new technology for the health sector.